



DYNAMIC LOADING OF ANATOMICALLY SHAPED MENISCAL CONSTRUCTS GENERATED VIA MRI AND **micro-CT IMAGING**

by Jeffrey Johnathan Ballyns

This thesis/dissertation document has been electronically approved by the following individuals:

Bonassar, Lawrence (Chairperson)

Van Der Meulen, Marjolein C.H. (Minor Member)

Nixon, Alan J (Minor Member)

DYNAMIC LOADING OF ANATOMICALLY SHAPED
MENISCAL CONSTRUCTS GENERATED VIA MRI AND μ CT IMAGING

A Dissertation

Presented to the Faculty of the Graduate School

of Cornell University

In Partial Fulfillment of the Requirements for the Degree of

Doctor of Philosophy

by

Jeffrey Jonathan Ballyns

August 2010

© 2010 Jeffrey Jonathan Ballyns

DYNAMIC LOADING OF ANATOMICALLY SHAPED MENISCAL CONSTRUCTS GENERATED VIA MRI AND μ CT IMAGING

Jeffrey Jonathan Ballyns, Ph. D.

Cornell University 2010

Several studies have established that dynamic stimulation by mixing media and dynamic compression enhances the production of extracellular matrix (ECM) and mechanical properties of tissue-engineered (TE) constructs seeded with articular chondrocytes. Very few studies have attempted to engineer a whole meniscus and none have attempted to dynamically stimulate this tissue *in vitro*.

The overall objective of this dissertation was to investigate the effect of dynamic stimulation on the biochemical and mechanical properties of image-guided tissue engineered menisci. The central hypothesis of this dissertation is that mechanical stimulation will alter the ECM assembly and mechanical behavior of anatomically shaped constructs. The first specific aim developed a method of generating patient specific anatomically shaped menisci using an image guided approach and tested the feasibility of culturing these engineered constructs using bovine meniscal fibrochondrocytes. The second specific aim developed a method of quantitatively comparing the shape fidelity of anatomically shaped tissue engineered menisci using various imaging and fabrication techniques. The third specific aim tested the hypothesis that controlled media mixing will enhance tissue formation and mechanical properties of anatomically shaped constructs compared to static controls. The fourth specific aim tested the hypothesis that dynamic compressive loading would improve biochemical and mechanical properties of image-guided tissue engineered

menisci. This work represents the first study to dynamically load an anatomically shaped engineered meniscus *in vitro*.

The studies presented in this dissertation are the first attempts to examine the effects of mechanical stimulation on large volume anatomically shaped TE menisci. The findings presented highlight 1) the effectiveness of image-guided fabrication techniques in generating patient specific TE implants and 2) the potential mechanical stimulation has to enhance tissue growth in engineered constructs.

BIOGRAPHICAL SKETCH

Jeffrey J Ballyns was born in Kingston, Ontario, Canada and raised in Oswego, New York. He is the eldest of three sons. Jeff received his B.S. at Cornell University, from the Sibley School of Mechanical and Aerospace Engineering. He majored in biomechanics as an undergraduate, where he was convinced to stay at Cornell to pursue a Ph.D. in biomedical engineering.

Working under the advisement of Larry Bonassar, Jeff has had the opportunity to participate in a number of community outreach events and present at conferences. His research has placed 1st and 3rd at Cornell research competitions and has also been rewarded by the Alfred P. Sloan Foundation Fellowship and a National Science Foundation GK-12 Fellowship. He has also authored a number of articles, 3 have been published and 3 more have been submitted for publication. Jeff would like to pursue further research in orthopaedic tissue engineering or a related field, where his main passions lie in product development of medical devices.

To my family and the Toasties

ACKNOWLEDGMENTS

Though only my name appears on the cover of this dissertation, many people have contributed to this work. I would like to extend my sincerest gratitude to my mentor and advisor, Lawrence Bonassar, Ph.D., for believing in me and constantly encouraging and exciting my passion for research. Working with Larry has been an honor and pleasure that I will not soon forget.

I would also like to thank the many people that I have had a pleasure to work with, namely Hollis Potter, M.D., Timothy Wright, Ph.D., and Suzanne Maher, Ph.D. from the Hospital for Special Surgery. The work we did served as the back bone for this dissertation. I would also like to thank Dan Cohen, Ph.D., Evan Malone, Ph.D., Jeffrey Lipton, and Hod Lipson, Ph.D. for opening their doors to me and allowing us to do some innovative work with 3D printing. I would also like to thank my fellow lab mates Robby Bowles, Omatunde Babalola, Ph.D., Satish Degala, Ph.D., Natalie Galley, Jenny Puetzer, Parksun Joo, Elysia Sheu, and John Nguyen for aiding me with my work and providing constant feedback.

I also want to thank the additional members of my advisory committee Alan Nixon, Ph.D. and Marjolein van der Meulen, Ph.D. whose input and guidance have been invaluable. Special thanks to Shivaun Archer, Ph.D. and Robert Doran for your contributions to the lesson plan developed for children at Newfield Middle School. Thank you Judy Thoroughman and Belinda Floyd for making sure my forms were always turned in and ensuring things ran smoothly.

I would also like to give special thanks to Heather Allen for your endless support and council. Without your help none of my work would have been completed on time.

Lastly I want to thank my funding sources the Alfred P. Sloan Foundation, Clark & Kirby Foundations, Soft Tissue & Sports Medicine Funds, MRRCC Core Center grant: NIH AR046121, the AO/ASOF Foundation: F-08-10B, the Cornell BME NSF GK-12 program: DGE 0841291, and Cornell University.

TABLE OF CONTENTS

BIOGRAPHICAL SKETCH.....	iii
DEDICATION	iv
ACKNOWLEDGMENTS.....	v
TABLE OF CONTENTS	vii
LIST OF FIGURES.....	x
LIST OF ABBREVIATIONS	xvii
LIST OF SYMBOL.....	xviii
CHAPTER 1.....	1
1.1 Meniscus of the Knee: Structure, Function, and Pathology.....	1
1.2 Biochemical and Mechanical Properties	2
1.3 Current Methods of Treatment and Tissue Engineering Efforts	6
1.4 Use of Dynamic Stimulation In Vitro	9
1.5 Research Objectives	11
<i>Specific Aims</i>	13
CHAPTER 2.....	16
2.1 Abstract.....	16
2.2 Introduction	16
2.3 Imaging Techniques	19
2.4 Fabrication Techniques	22
Injection Molding.....	23
Rapid Prototyping.....	26
Lithography	29
Sintering	30
2.5 Conclusions	31
CHAPTER 3.....	34
3.1 Abstract.....	34
3.2 Introduction	34
3.3 Materials and Methods	37
Imaging.....	37
Mold Design.....	39
Injection Molding.....	39
Biochemistry.....	40
Histology	41
Mechanical Testing	41
Statistical Analysis	42
3.4 Results	42
3.5 Discussion.....	46
CHAPTER 4.....	50
4.1 Abstract.....	50
4.2 Introduction	51
4.3 Materials and Methods	53
Imaging.....	53

Mold Design	54
Injection Molding	54
3D Printing	54
Geometric Analysis	56
Statistics.....	57
4.4 Results	58
Quantification of Gross Anatomy	58
Pooled Measurements.....	59
Individual Sample Analysis.....	61
Success Criteria	66
4.5 Discussion.....	68
CHAPTER 5	74
5.1 Abstract.....	74
5.2 Introduction	74
5.3 Materials and Methods	76
Molded Constructs.....	76
Culture Environment	77
Sample Preparation.....	79
Mechanical Analysis	79
Biochemistry.....	80
Histology	80
Statistics.....	80
5.4 Results	81
Construct Appearance and Composition	81
Comparison between Large Volume and Small Volume Constructs	81
Effect of Mixing Intensity	83
Mechanical Analysis	86
Spatial Comparison between Mixing Intensities	88
5.5 Discussion.....	90
5.5 Conclusion.....	95
5.6 Supplementary Data	95
CHAPTER 6	96
6.1 Abstract.....	96
6.2 Introduction	97
6.3 Methods	98
Mold and Loading Platen Design and Fabrication	98
Dynamic Loading Conditions.....	99
Post Culture Sample Analysis	102
Statistics.....	104
6.4 Results	104
FE Model	104
Construct Shape Fidelity and Composition	104
The Effect of Dynamic Compression	105
6.5 Discussion.....	110

CHAPTER 7	113
7.1 Future Directions	121
Introduction of growth factors	122
Altering biomaterial properties	122
Optimizing mechanical stimulation protocol	124
CHAPTER 8	126
8.1 Abstract	126
8.2 Introduction	126
8.3 Article Background	130
What is Tissue Engineering?	131
Materials used in Tissue Engineering	132
Characterizing the strength of engineered tissue	133
8.4 Tissue Engineering Activity	133
8.5 Alginate Activity #1	136
<i>Materials and Teacher Preparation</i>	136
<i>Performing the Activity</i>	136
8.6 Alginate Activity #2	138
<i>Materials and Teacher Preparation</i>	138
<i>Performing the Activity</i>	138
8.7 Results	139
<i>Class Performance</i>	139
8.8 Concluding Remarks	142
APPENDIX A	143
APPENDIX B	150
APPENDIX C	152
APPENDIX D	155
APPENDIX E	166
APPENDIX F	171
REFERENCES	174

LIST OF FIGURES

CHAPTER 1

Figure 1.1: Regional tensile properties (MPa) for human medial and lateral menisci...3

CHAPTER 2

Figure 2.1: Image guided tissue engineering process tree.....17

Figure 2.2: Examples of image guided tissue engineering techniques.....26

CHAPTER 3

Figure 3.1: Image processing steps for CT and MRI scans to design injection molds.....38

Figure 3.2: Photographs of intact implants, cross-sectional views, tissue sections stained with Safranin-O, and tissue sections stained with picosirius red.....43

Figure 3.3: Temporal changes in DNA content and hydroxyproline content in tissue-engineered menisci and native meniscus.....44

Figure 3.4: Temporal changes in GAG content and compressive equilibrium modulus in tissue-engineered menisci and native meniscus.....45

CHAPTER 4

Figure 4.1: Custom gantry robot with laser triangulation distance sensor capturing surface of native and engineered sample.....55

Figure 4.2: Key dimensions that were measured physically and computationally.....57

Figure 4.3: Photographs of engineered menisci and respective deviation color heat maps.....58

Figure 4.4: Average % error across key dimensions as a function of fabrication method.....60

Figure 4.5: Scatter plot of height errors.....62

Figure 4.6: Scatter plot of width errors.....63

Figure 4.7: Scatter plot of depth, span, volume, and posterior and anterior width errors.....	64
Figure 4.8: Average % error for height width and volume across different sheep and fabrication methods.....	65
Figure 4.9: Average % error across different sheep and fabrication methods for depth, span, and posterior and anterior widths.....	67
CHAPTER 5	
Figure 5.1: Media mixing bioreactor schematic and photographs.....	77
Figure 5.2: Spatial locations of biopsy plugs taken for confined compression and biochemical analysis.....	79
Figure 5.3: Photographs of intact implants, cross-sectional views, tissue sections stained with Safranin-O and with picrosirius red.....	82
Figure 5.4: Plots of DNA content, collagen content, GAG content, and compressive modulus comparing large and small volume constructs.....	84
Figure 5.5: DNA content, GAG content, and collagen content found in engineered constructs and cumulative release to the culture medium for different mixing intensities.....	85
Figure 5.6: Compressive equilibrium modulus and tensile modulus for different mixing intensities across culture time.....	87
Figure 5.7: Spatial properties for DNA content, collagen content, GAG content and compressive modulus for Re 0.5, Re 2.9, and Re 21.8.....	89
Figure 5.8: Photographs of a cellular alginate gels after 3 weeks of culture in static, Re 5.8 and Re 21.8 mixing intensities.....	94
Figure 5.9: Plot of wet weight mass for acellular alginate hydrogels over 21 days of culture.....	94

CHAPTER 6

Figure 6.1: 3D printed ABS plastic parts generated via μ CT data used for injection molding and dynamic compression in custom bioreactor.....	99
Figure 6.2: Boundary conditions for linear poroelastic FE model.....	100
Figure 6.3: Predicted compressive strains, stresses, and Von Mises Stresses for high (352 μ m) and low (171 μ m) imposed displacement groups.....	102
Figure 6.4: Photographs, deviations heat maps, and histology of static, 171 μ m, and 352 μ m groups across 6 weeks of culture.....	107
Figure 6.5: Compressive equilibrium modulus, GAG content, collagen content, and DNA content found in engineered constructs and cumulative release to the culture medium for different culture conditions.....	108

CHAPTER 7

Figure 7.1: GAG content, collagen content, compressive equilibrium modulus and tensile modulus for engineered tissues exposed to varying culture conditions.....	117
Figure 7.2: E(t) model using rule of mixtures for static, Re 2.9, Re 21.8, and 352 microns along side measured compressive modulus values.....	118

CHAPTER 8

Figure 8.1: Point cloud images used to design a knee meniscus or human ear for tissue engineering.....	131
Figure 8.2: Quiz given to student before and after 3 day lesson.....	134
Figure 8.3: Hand out for students with a list of materials and instruction for the first alginate activity.....	135
Figure 8.4: Layout of materials used for alginate activities.....	137
Figure 8.5 Hand out for students with a list of materials and instruction for the second alginate activity.....	140

Figure 8.6: Student Pre- and Post-Quiz performance.....	141
Figure 8.7: Student praise for alginate activities.....	142
APPENDIX A	
Figure A.1: Comparative MRI, μ CT, and laser scan of the same ovine meniscus....	143
APPENDIX B	
Figure B.1: Plots of DNA content, collagen content, and GAG content, looking at the individual spatial properties for Re 5.8 and Re 10.2.....	150
APPENDIX C	
Figure C.1: Original bioreactor design with an ice pack and retrofitted bioreactor with heat sinks, cooling fans, and load cell.....	152
Figure C.2: Labview diagram for the bioreactor.....	153
Figure C.3: Graphic user interface of Labview bioreactor program.....	154
APPENDIX D	
Figure D.1: Predicted FE model fluid velocity directions and pressure gradients for 171 μ m and 352 μ m loaded menisci.....	156
Figure D.2: Deviation histograms of static and dynamically loaded constructs and 0.29, 2 and 6 weeks.....	157
Figure D.3: Tensile modulus for static and 352 μ m dynamically loaded samples.....	158
Figure D.4: DNA content and ECM accumulation at different locations throughout dynamically loaded TE menisci.....	159
APPENDIX E	
Figure E.1: Model fits for alginate scaffold mass degradation, GAG accumulation, collagen accumulation, and equilibrium compressive modulus for different culture conditions.....	168

APPENDIX F

Figure F.1: DNA and GAG content for the first and second pilot studies.....172

Figure F.2: DNA, GAG, and collagen content for the third pilot study.....173

LIST OF TABLES

CHAPTER 1

Table 1.1: The range of compressive and tensile properties for human, bovine, canine, lapine, and ovine menisc.....4

Table 1.2: Meniscal tissue engineering efforts done with alginate, PCL, PGA, agarose compared to native meniscus.....8

CHAPTER 2

Table 2.1: Image modality characteristics.....20

Table 2.2: Fabrication techniques and the various biomaterials used for cell seeded scaffolds and acellular scaffolds as well as multi-cell/material capability and current resolution capabilities.....28

CHAPTER 4

Table 4.1: Average volumetric error, percentage of points from deviation heat maps that fell within $\pm 10\%$ of the native tissue, and repeatability error of fabrication methods.....60

Table 4.2: Percentage of points that fell within $\pm 10\%$ deviation from native tissue...67

Table 4.3: Repeatability error for each sheep meniscus and fabrication method.....68

CHAPTER 5

Table 5.1: Listed Reynolds numbers, respective magnetic stir bar length, the number of rotations per minute, and the resulting type of flow in the mixing media bioreactor.....78

CHAPTER 6

Table 6.1: Shape fidelity data for cultured samples represented by the number of points from deviation heat maps that fell within $\pm 10\%$, construct volume, and construct mass.....106

APPENDIX E

Table E.1: Constants for initial alginate mass, time constants and steady state GAG and collagen concentrations for different culturing conditions based on model fits to measured biochemical data.....168

LIST OF ABBREVIATIONS

3-D	three-dimensional
ANOVA	analysis of variance
Ca ²⁺	calcium
CaCl ₂	calcium chloride
CaSO ₄	calcium sulfate
DMAB	dimethylaminoborane
DMEM	Dulbecco's Modified Eagle Medium
DMMB	1, 9 Diethylmethylene blue
DNA	deoxyribonucleic acid
DW	dry weight
ECM	extracellular matrix
EDTA	ethylenediaminetetraacetic acid
FBS	fetal bovine serum
FE	finite element
g	gram
GAG	glycosaminoglycans
Hz	hertz
IGF	insulin-like growth factor
Kg	kilogram
kPa	kilopascal
µm	micrometer
µg/ml	micrograms per milliliter
mm	millimeter
M	molar
mM	millimolar
MPa	megapascal
MSC	mesenchymal stem cell
MRI	magnetic resonance imaging
nm	nanometer
OA	osteoarthritis
Pa	pascal
PBS	phosphate buffered saline
PEG	poly(ethylene glycol)
% W/V	percent weight per volume
PLA	polylactic acid
PLGA	poly(lactic-co-glycolic acid)
PLLA	poly-L-lactic acid
RGD	Arginine-Glycine-Aspartate
SD	standard deviation
SEM	standard error mean
TE	tissue engineering or engineered
TGF-β	transforming growth factor beta
U/ml	units per milliliter
WW	wet weight

LIST OF SYMBOL

Symbol	Variable or parameter	Dimensions
HA	aggregate modulus	N/m^2
ω	angular velocity	rad/s
$^{\circ}\text{C}$	degrees Celsius	---
ρ	fluid density	g/mL
μ	fluid viscosity	Pa·s
Q	flow rate	mL/s
L	length	m
ℓ	mesh pore size	μm
K	permeability	m^4/Ns
p	pressure	N/m^2
Re	Reynolds number	---
τ	shear stress	N/m^2
σ	stress	N/m^2
v	velocity	m/s
E	Young's modulus	N/m^2

CHAPTER 1

INTRODUCTION

1.1 Meniscus of the Knee: Structure, Function, and Pathology

Interest in the meniscus of the knee has been increasing rapidly in recent years as its importance in the joint becomes more apparent. When I began my research five years ago, few people could have identified what a meniscus was, unless they or an immediate family member had a torn meniscus. However in 2010, many people are aware of the meniscus of the knee, in part because a meniscal tear is one of the most common results of traumatic injuries in the knee, second only to osteoarthritis (OA) [1]. Typically, symptoms of a torn meniscus include pain, swelling, catching, locking, and episodes of giving way [2]. There are over a million meniscal operations done annually in the United States [3] and the most common form of treatment is a total or partial meniscectomy. However, removing part or the entire meniscus is known to greatly accelerate the onset of OA on the surrounding articular cartilage. The meniscus is a fairly avascular tissue and as a result, has a notoriously slow healing ability. Common modes of failure include vertical tears, flap tears, horizontal tears and the most extreme bucket handle tears [4].

There are two menisci in each knee, a medial and lateral, each having a semi-lunar shape located between the femoral condyles and tibial plateau in the knee. The key functions of the meniscus are to aid in joint load distribution, serve as a shock absorber, and act as a secondary joint stabilizer [5]. The meniscus also aids in joint lubrication. Upon the removal of the meniscus, the coefficient of friction in the knee can increase by 20% [6].

A skeletally mature meniscus is a fibrocartilagenous tissue with anisotropic properties that vary by location. These complex mechanical properties are due to the extracellular matrix (ECM) that is primarily composed of type I and II collagen,

glycosaminoglycans (GAG), and water [6]. GAG provides the equilibrium compressive modulus and the collagen provides the tensile strength. The meniscus has a complex geometry, which plays a critical role in joint load distribution. Small changes in the radius of curvature in the femur can greatly change stress distributions in a cross section of the meniscus, highlighting the importance of shape congruity between the articulating surfaces [5]. Not only is meniscal shape critical for proper joint mechanics, but if damaged could greatly increase the probability of osteoarthritis (OA).

1.2 Biochemical and Mechanical Properties

The composition of the ECM of the meniscus is represented by type I collagen (65% dry weight), type II collagen (5% dry weight), GAG (2% of dry weight), and water (74% by wet weight)[6]. The equilibrium compressive modulus for a human meniscus can range from 0.150 – 0.220 MPa [7] while the tensile strength along the fiber direction can be as high as 300 MPa, but drops to 10% of this value (30 MPa) when perpendicular to the fiber direction [8]. The wide range in tensile properties can largely be explained by the orientation of collagen fibers, which varies with location along the meniscus and also spatially (Fig. 1.1).

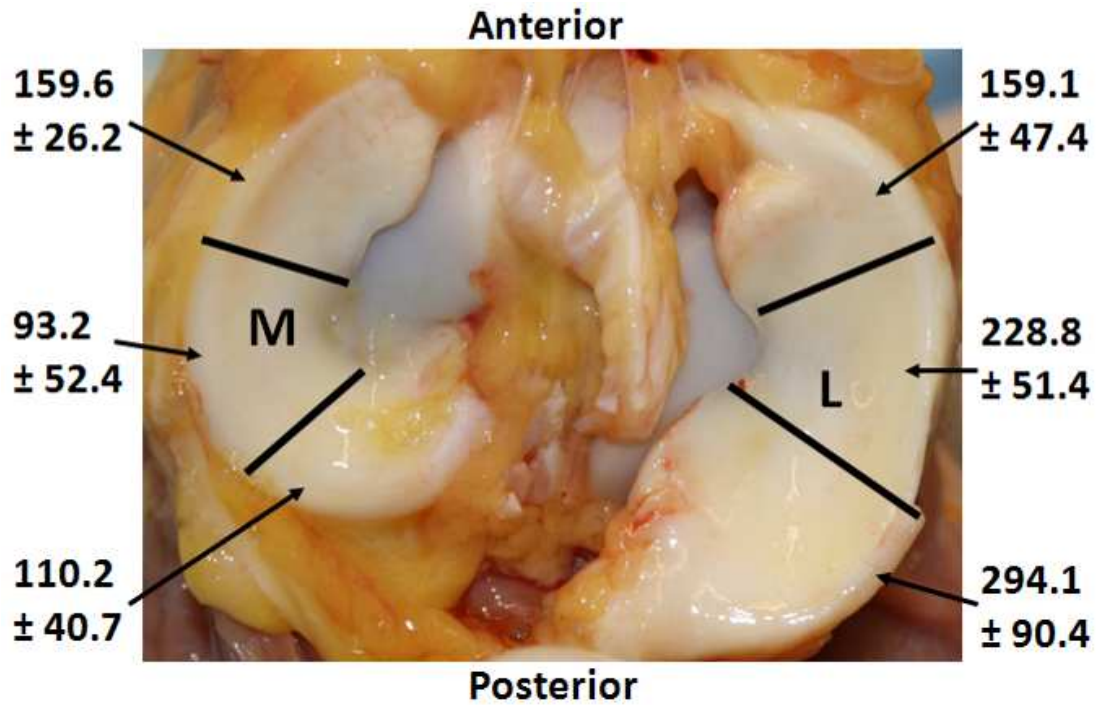


Figure 1.1: Regional tensile properties (MPa) for human medial and lateral menisci [8].

The large variation in tensile properties between different regions of the meniscus is not unique to human. In fact, similar trends in region and depth dependent properties are found in the menisci of multiple species (Table 1.1). Interestingly, there is a large amount of overlap in the range of meniscal tensile and compressive properties across these various species despite the differences in loading conditions as a result of weight, gait cycle, and whether the animal is a biped or quadruped (Table 1.1).

Table 1.1: The range of compressive and tensile properties for human [8, 9], bovine [9, 10], canine [9, 11], lapine [7, 9], and ovine menisci [12, 13].

Species	Compressive Equilibrium Modulus (kPa)	Tensile Modulus (MPa)
Human	150 - 220	30 - 300
Bovine	110 - 490	48 - 260
Canine	190 - 434	65 - 136
Lapine	120 - 500	108 - 206
Ovine	160 - 260	190 - 260

The geometry and highly organized fibers of the meniscus are believed to be a result of the physical environment that cells experience *in utero*. However little is known about how this fibrocartilagenous tissue matures embryologically. Research suggests an approximate time table of when the medial and lateral menisci begin to form in the knee: the meniscus begins as a single layer of mesenchymal cells that grow into a bundle at week 9 of gestation [14]. At weeks 10 and 11 of development cavitation occurs. This cavitation allows the formation of articular surfaces and a cavity between the bottom of the femur and top of the tibia and fibula. This cavity allows for mesenchymal cells to separate and form a visible meniscus.

Exactly when the horns of the menisci become attached is unclear, though it has been claimed that the horns attach as early as 10 weeks of development [14] and as late as 16 weeks for both lateral and medial meniscal attachment to the tibia and fibula [15]. At week 14, cells appear spindle shaped and parallel to the direction of the lateral meniscus, but are randomly oriented in the medial meniscus. Collagen bundles do not appear until week 17, but become thickly oriented fibers by week 25 [16].

A meniscus that is skeletally mature has a very distinct collagen fiber orientation/infrastructure. This collagen fiber architecture varies with location (anteriorly to posteriorly), and also varies throughout the depth of the tissue [17]. Estimates suggest there are 5 distinct zones of collagen fiber orientation throughout the depth of the meniscus [17]. While the complex collagen network is thought to be anisotropic, there is no consensus on an appropriate constitutive model. Currently, an orthotropic model would be the best estimation of mechanical behavior, since properties have been reported for compression, tension in the fiber direction (FD), tension perpendicular to the fiber direction (PFD), and the respective shear moduli and Poisson ratios [5, 7, 8, 18, 19].

Prior work has modeled the meniscus using simple geometries and linear elastic isotropic properties [5, 18, 19]. By using simple geometries and a transversely orthotropic model it was shown that altering the radius of curvature of the femur can greatly change the stress distributions in a cross section of the meniscus [5]. Pena and coworkers applied MRI imaging data with a spatial resolution of 1.5mm between image slices to give rough anatomical geometries of the femur, tibial, meniscus, and key ligaments in the knee. The MRI model applied linear elastic isotropic properties for the meniscus, demonstrating that an intact lateral meniscus under static load resulted in a peak stress of 1.45 MPa and 3.02 MPa for a torn meniscus [18]. The peak stress calculated by Pena et al. for an intact meniscus was an estimated compressive strain of 6.6 – 9.7%.

Vadher and coworkers also used a simple cross sectional geometry to model the effects of increasing the percentage of meniscal tissue that is removed during a partial menisectomy. They reviewed how this removal changed contact pressures on the surrounding articular cartilage, finding—similarly to Pena et al.—that there was a

positive correlation between contact pressures on cartilage surfaces and the percentage of meniscal tissue removed.

As of Spring 2010, there have been no attempts to model the meniscus as a region specific, orthotropic tissue. Furthermore, there are very few studies that observed *in vivo* deformations of the meniscus. The few *in vivo* studies that have measured meniscal displacements have found that the meniscal volume after running 5 km, 10 km and 20 km resulted in a 5.2%, 7.5%, and 10.1% decreases respectively [20]. Mastrokalos et al. assessed the mean height of the posterior horns of the lateral and medial meniscus under no load and load, equal to 100% body weight. Full body weight resulted in a decrease of posterior horn height by 0.8 mm for the medial meniscus and 0.7 mm for the lateral meniscus [21] which is estimated to be 11.8% and 10.1% compressive strain, respectively. Measured *in vivo* meniscus displacements can prove to be useful to validate current FE models or in designing a loading protocol for tissue engineering purposes as will be seen later in this dissertation (Chapter 6).

1.3 Current Methods of Treatment and Tissue Engineering Efforts

Suture techniques and newly developed repair devices for focal defects have recently garnered much attention. Evaluations have been conducted to assess how these devices and techniques perform in repairing torn menisci. Though repair devices simplify surgical techniques and decrease the risks associated with surgery, they perform poorly on initial fixation strength when compared to vertical sutures [22]. The future success of developing repair devices depends on improving initial fixation strength, increasing their ability to withstand clinical stresses, and optimizing the device hydrolysis (i.e. degradation rate as tissue regenerates).

There have been great advances to repair meniscal tears, but in some cases, the entire meniscus still needs to be replaced. Ideally, the recipient could receive a

cadaveric transplant. But the possibility and utility of receiving a meniscal transplant is mitigated due to the scarcity of donor tissue, risk of disease, and lack of a standardized method of fixation [23]. Further complicating cadaveric meniscal transplantation, size matching is necessary to restore proper joint mechanics. If the replacement tissue deviates by more than $\pm 10\%$ for some key dimensions, increased normal stresses result on the tibial plateau that will subsequently damage the surrounding articular cartilage (for oversized tissue) or cause higher meniscal hoop stresses (for undersized tissue) [24]. These higher hoop stresses increase the chance of a tear in the newly transplanted meniscus [24]. As a result of these challenges, other solutions for meniscal replacement are being actively explored in the field of tissue engineering.

To generate functional artificial living tissues to replace damaged tissues, specifically the meniscus, three major concerns need to be addressed. First, the engineered construct must be anatomically accurate to provide proper mechanical function [5]. Second, engineered menisci must be able to withstand anatomical compressive and tensile loading prior to implantation. Third, tissue engineered structures need to achieve the region specific mechanical and biochemical properties found in the native meniscus.

Of the over 40 studies that have focused on meniscal tissue engineering, only 11 have attempted to generate anatomically shaped constructs. These anatomically shaped tissue engineered (TE) studies have used a variety of culturing environments and scaffolding materials, including: polyurethane with poly(ϵ – caprolactone) (PCL) cultured in a dog model [25], polyvinyl alcohol-hydrogel (PVA-H) cultured in a rabbit model [26], polyglycolic acid (PGA) mixed with poly-(lactic-co-glycolic acid) (PLGA) cultured in a rabbit model [27], a scaffoldless meniscus cultured *in vitro* [28], and an alginate scaffold cultured *in vitro* [29]. None of the studies which generated

anatomically shaped constructs attempted to quantify the shape fidelity of their constructs. Furthermore, a comparison of *in vitro* cultures which analyzes mechanical properties and matrix production is difficult since very few studies evaluate proteins produced by cells and instead study gene expression. All of the studies that have seeded cells on or into scaffolds and used *in vitro* culturing conditions have resulted in menisci (or whatever it is) with areas of strength and weakness. However, these studies have yet to replicate native tissue properties in experimental conditions (Table 1.2). While the work done with these different scaffolding materials is promising, most has been with simple geometry constructs in static free swell culture. Very little research has been conducted on the effect mechanical stimulation might have on meniscal fibrochondrocytes. Moreover, virtually no studies have attempted to apply a dynamic loading regime on an anatomically-shaped tissue engineered meniscus.

Table 1.2: Meniscal tissue engineering efforts done with alginate [29], PCL [30], PGA [28], and agarose [31] compared to native meniscus [7, 8, 28, 32] with total volume, GAG normalized to dry weight (DW), collagen normalized to DW, compressive equilibrium modulus, and tensile modulus.

Scaffold	Volume (mL)	GAG ($\mu\text{g}/\text{mg DW}$)	Collagen ($\mu\text{g}/\text{mg DW}$)	Compressive Equilibrium Modulus (kPa)	Tensile Modulus (Mpa)
Alginate	1.75 – 5.0	5.8 – 9.6	7.5 – 89.3	12.7 – 18.1	12.7×10^{-3} – 18.1×10^{-3}
PCL	0.11 – 0.16	31.5 – 39.8	22.1 – 61.8	NA	1.0 – 7.6
PGA	0.16	28.8 – 166.2	73.9 – 95.4	5.8 – 10.0	11.0×10^{-3} – 21.0×10^{-3}
Agarose	0.16	3.0 – 14.0	0.0 – 4.0	10.0	NA
Native Meniscus	1.75 – 5.0	20.0 – 30.0	600 – 700	150 – 220	93.2

1.4 Use of Dynamic Stimulation In Vitro

In an effort to increase ECM synthesis by cells in tissue engineered constructs, many researchers have turned to dynamic stimulation. Because dynamic loads such as compression, shear, and hydrostatic forces are all present in the native loading environment of the knee, a variety of dynamic stimulatory devices have been designed to institute these forces individually or in combination on cell seeded scaffolds. Although bioreactors applying *in vivo* mechanical forces are being studied, most of the tissue engineering research has been with simple geometry scaffolds using articular chondrocytes. Though a few studies examining the effects of dynamic stimulation on meniscal fibrochondrocytes do exist, they have focused on simple geometry plugs or small tissue explants.

Controlled media mixing has been widely used to stimulate TE constructs seeded with articular chondrocytes (AC) [33-36] and has been used with meniscal fibrochondrocytes [37, 38]. Media mixing stimulation is relatively simple to implement when compared to direct compressive or tensile stimulation, and is easily controlled by altering the rotation speeds of the stir bar mixing the media. As such, several studies have demonstrated over a wide range of mixing intensities that mixing bioreactors increases the amount of extracellular matrix (ECM) 3 to 9 fold and the mechanical properties 3 to 4 fold for TE cartilage [31, 34-37]. It has also been found that high turbulent mixing intensities can greatly increase ECM production in tissue engineered constructs containing articular chondrocytes [34] or meniscal fibrochondrocytes [37]. High turbulent mixing greatly increases collagen fibril formation in small engineered plugs, which forms a fibrous capsule around the outer surface of the engineered tissue [34].

Another widely researched form of stimulation is dynamic compression. Similarly to controlled media mixing, the majority of the research which reviews the effects of

dynamic compression on tissue engineered constructs has employed articular chondrocytes. Dynamic compression studies have typically measured gene expression for GAG and collagen type II of articular chondrocytes [39-41]. Most compression studies are short term cultures, of less than 2 weeks, where simple geometric constructs are exposed to compressive strains ranging from 3 – 20% at frequencies of 0.33 – 3 Hz [39-45]. The duty cycles typically 30 – 120 minutes with 1 – 6 hours of rest done daily.

Tissue engineering dynamic compression studies with articular chondrocytes present evidence that compression increases gene expression for GAG and collagen type II [39, 40, 43] and also improves the compressive properties which correlate with increased GAG accumulation in cultured constructs [42, 44]. Of the studies that have performed biochemical analysis on engineered samples, it has been observed that cells do produce more GAG under dynamic compression at a frequency of 1 Hz and that continuous loading increases GAG loss and DNA loss from constructs [39, 40]. However, research has found that alternate day loading can greatly improve cell retention in longer time point cultures [39].

It is clear that most of the research and literature has focused on the cellular response of tissue explants to dynamic compression. The evidence suggests that a large range of gene expression responses are initiated by this dynamic compression, particularly (or including) increased GAG, collagen type I synthesis, MMP1, MMP3, and production of other cell mediators such as nitric oxide and prostaglandin [41, 46-50]. Of the published meniscal tissue engineering studies produced by other labs, only 6 articles measure the amount of GAG and collagen that are accumulated in engineered tissue [27, 30, 51-55], and of these only 5 measure mechanical properties. Only 3 articles expose these constructs to dynamic stimuli [27, 51, 53].

Mechanical and biochemical data are rarely reported because few dynamic compression studies stimulate engineered tissues long enough to observe if an increase in GAG or collagen gene expression will translate into protein production for the respective gene. While gene expression is a good indicator of protein production potential, it does not always correlate well. In this dissertation, data is presented on the accumulation of GAG and collagen produced by meniscal fibrochondrocytes in anatomically engineered constructs. Moreover, this research measures mechanical properties to evaluate how these matrix constituents contribute to the mechanical behavior of a TE meniscus.

1.5 Research Objectives

As a science, tissue engineering attempts to generate living tissues that mimic the functions of healthy tissues in the body to replace damaged or nonfunctioning tissues/organs. To achieve this goal, the field has focused on 1) creating innovative fabrication methods to correspond with the development of novel biomaterials and 2) analyzing the cellular behavior of these biomaterials and studying how it can be altered based on the culture environment.

However, there has been little work done developing image-guided approaches to generate geometrical complex tissues such as the meniscus. Very little is known about meniscal fibrochondrocytes and how best to stimulate this cell type to produce functional engineered tissues.

The research presented in this dissertation makes significant steps towards establishing feasible methods for recreating the complex geometry of the meniscus via image-guided techniques that utilize injection molding and 3D tissue printing. Continuing research for patient specific implants will rely on image-guided tissue engineering as a foundation. The review article, which is featured in Chapter 2, offers

more information on image guided tissue engineering. The overall objective of this dissertation was to investigate the effect of mechanical stimulation on the biochemical and mechanical properties of image-guided tissue engineered menisci. The central hypothesis of this dissertation is that mechanical stimulation will alter the ECM assembly and mechanical behavior of anatomically shaped constructs compared to statically cultured controls.

Before research can be conducted on the effects of mechanical simulation on anatomically shaped TE constructs, a method for fabricating such tissues developed. Chapter 3 presents an image guided approach to generating anatomically shaped TE menisci via injection molding utilizing MRI and micro-CT (μ CT) data. Before the work presented in Chapter 3, no method existed to generate such tissues or a method to evaluate the accuracy of a TE construct to ensure the proper geometry to restore proper joint function. Chapter 4 presents a method to compare shape fidelity of engineered tissues quantitatively.

After establishing these methods of fabrication and shape fidelity verification, research on the effects of mechanical simulation on anatomically shaped TE menisci can begin. The first approach to studying the effects of mechanical simulation on anatomically shaped TE menisci was to increase the matrix production via a chemical engineering approach. This approach improved nutrient transport throughout large volume constructs through media mixing (Chapter 5). The second approach leveraged mechanical engineering to apply dynamic compression on the complex shaped engineered tissues to elicit an increase in ECM production (Chapter 6). Utilizing the fabrication and shape evaluation techniques presented in Chapters 3 and 4, over 146 TE menisci were generated, cultured, and analyzed to complete this thorough examination of two contrasting forms of mechanical stimulation.

Specific Aims

Specific Aim 1 (Chapter 3)

To develop a method of generating patient specific anatomically shaped menisci using an image-guided approach and test the feasibility of culturing these engineered constructs using bovine meniscal fibrochondrocytes.

Widely used medical imaging modalities such as computed tomography (CT) and magnetic resonance imaging (MRI) were used to obtain geometrical data of meniscal tissue. Computer-aided design (CAD) utilized geometrical data to design injection molds that were subsequently printed out of acrylonitril butadiene styrene (ABS) plastic. Anatomically shaped engineered tissues were obtained by injection molding a 2:1 ratio combination of 2% weight per volume (w/v) alginate with 2% w/v CaSO₄. Tissue engineered menisci were then cultured for 8 weeks under static free swell conditions *in vitro*. Constructs maintained shape throughout culture and also had progressive tissue formation as indicated by increases in ECM content and mechanical properties.

Specific Aim 2 (Chapter 4)

Develop a method of quantitatively comparing the shape fidelity of anatomically shaped tissue engineered menisci using various imaging and fabrication techniques.

Four ovine menisci were scanned via MRI and μ CT imaging technique. These menisci served as templates for injection mold design and 3D tissue printing. Tissue engineered menisci were produced by impression molds, ABS plastic molds or 3D tissue printing. Impression molds were fabricated using ovine menisci and a silastic rubber, while ABS plastic molds were 3D printed directly on a Stratasys FDM 3000. Printed tissues were made on a custom open-architecture solid freeform fabrication

platform. Hydrogel constructs were scanned via laser triangulation distance sensor. The point cloud images were analyzed to acquire computational measurements for key points of interest (e.g., height, width, and volume) and to examine deviation from native tissue. Both imaging modalities and fabrication techniques produced anatomically shaped constructs of high geometric fidelity. Injection molded samples were more accurate and reproducible than 3D printed samples. Constructs based on μ CT images were more accurate than MRI-based samples, likely due to the difference in image resolution. However, MRI molds did yield samples with a significant fraction of key dimensions within $\pm 10\%$ error with respect to the native tissue.

Specific Aim 3 (Chapter 5)

To test the hypothesis that controlled media mixing will enhance tissue formation and mechanical properties of anatomically shaped constructs compared to static controls.

A mixing media bioreactor was designed to ensure proper mixing of culture medium while protecting the constructs from the spinning impeller. Mixing intensity was controlled by altering impeller size and speed to produce Reynolds numbers (Re) of 0.5, 2.9, 5.8, 10.2, and 21.8. Engineered menisci were cultured for up to 6 weeks. Matrix accumulation in engineered tissues and ECM loss to the media was compared and analyzed across varied mixing intensities and culture time. Plugs taken from various locations of engineered constructs were tested under confined compression and tension to determine the equilibrium and tensile modulus, respectively. Constructs maintained their overall shape fidelity throughout culture for all mixing intensities. Media stimulation resulted in increased mechanical properties and ECM accumulation in constructs over 6 weeks of culture. However media mixing was not beneficial for

all mixing intensities. The benefits of improved matrix accumulation and mechanical properties peaked near Re 2.9, and then decreased with increased mixing intensity.

Specific Aim 4 (Chapter 6)

To test the hypothesis that dynamic compressive loading would improve biochemical and mechanical properties of image-guided tissue engineered menisci. This work represents the first study to dynamically load an anatomically shaped engineered meniscus *in vitro*.

Tissue engineered menisci were loaded via a custom bioreactor with loading platens specifically designed to load these complex shaped tissues in unconfined compression. Loading platens and a loading tray, used to restrict tissue movement under mechanical loading, were designed using μ CT imaging data. The design process for the loading platen and loading tray was similar to that of the injection molds, all of which were 3D printed out ABS plastic. Finite element simulations were generated to guide the loading of engineered tissues and yield physiological strain levels under the imposed sinusoidal displacements. Constructs were loaded 3 times a week for 2 hours with 1 hour of intervening rest for up to 6 weeks of culture. There was a high loading condition with maximum compressive displacement of 704 μ m and a low loading condition with maximum displacement of 342 μ m. After 2 weeks of culture, both loading groups experienced increases in ECM accumulation and mechanical properties. Improved tissue growth was not maintained with prolonged loading as indicated by decreased matrix and mechanical properties from week 2 to week 6, which could be indicative of an altered rate of alginate scaffold degradation or an initiated catabolic cellular response.

CHAPTER 2

IMAGE-GUIDED TISSUE ENGINEERING: A REVIEW

Published in the *Journal of Cellular and Molecular Medicine*¹ [32]

2.1 Abstract

Replication of anatomic shape is a significant challenge in developing implants for regenerative medicine. This has led to significant interest in using medical imaging techniques such as magnetic resonance imaging (MRI) and computed tomography (CT) to design tissue engineered (TE) constructs. Implementation of medical imaging and computer aided design (CAD) in combination with technologies for rapid prototyping of living implants enables the generation of highly reproducible constructs with spatial resolution up to 25 μ m. In this paper, we review the medical imaging modalities available and a paradigm for choosing a particular imaging technique. We also present fabrication techniques and methodologies for producing cellular engineered constructs. Finally, we comment on future challenges involved with image guided tissue engineering and efforts to generate engineered constructs ready for implantation.

2.2 Introduction

Tissue engineering attempts to generate new living tissues through the use of engineering principles and biological sciences [56]. There are many different techniques and methodologies used to generate these new tissues (Fig. 2.1), which have progressed beyond contemporary structural design. Traditionally, when constructing a building, the process begins with the designer using a protractor, straight edge, and compass to produce a sketch that will be translated to CAD software

¹ Ballyns JJ, Bonassar LJ. Image-Guided Tissue Engineering. *Journal of cellular and molecular medicine* 2009;13:1428-1436.

for blueprint production. However, in nature, one rarely sees right angles and straight edges. In the human body the curved surfaces on the exterior of the body result in one's identity (e.g. facial mapping and finger prints). Internally, geometric features result in proper joint load distributions in the hip, knee, and ankle. Blood flow in a beating heart is properly restricted by the size and behavior of leaflet valves. Larger organs, such as the liver, have highly organized circulating systems necessary to deliver oxygenated blood through the larger structure. Replicating the complex geometries in naturally occurring structures in the body will require more than protractor and compass. To this end, the development of high resolution imaging techniques combined with biomaterials processing technology has given rise to the field of image-guided tissue engineering.

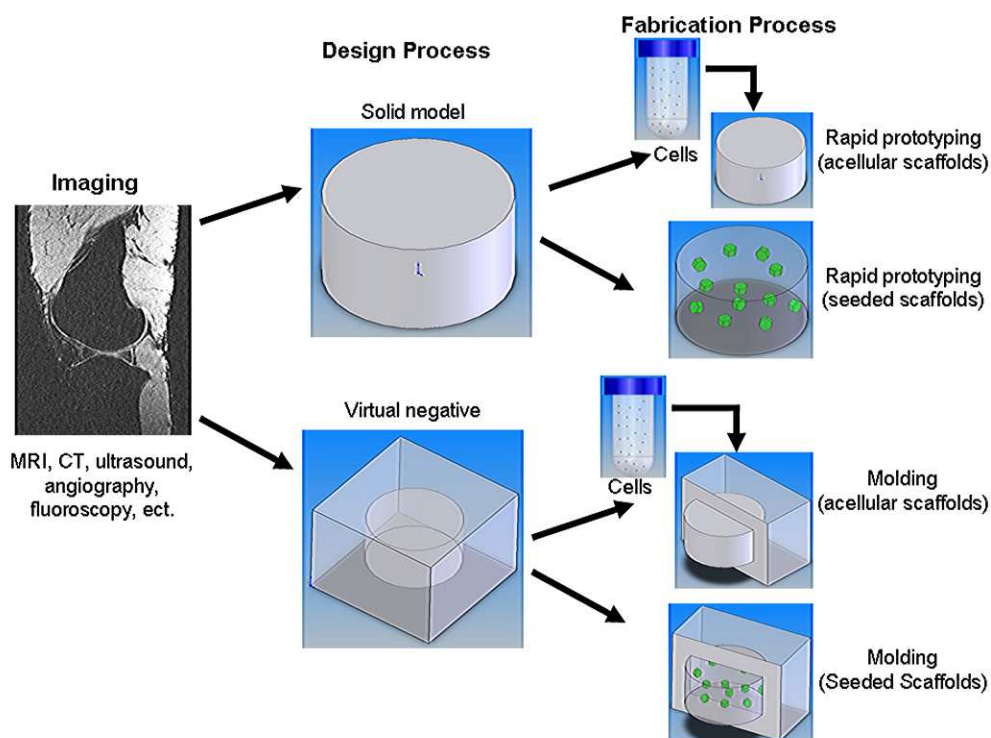


Figure 2.1: Image guided tissue engineering process tree.

Typically, imaging modalities such as magnetic resonance imaging (MRI) and computed tomography (CT) have been used as diagnostic tools to visualize the body and develop treatment strategies. Treatment strategies include choosing the type of implant, designing a patient specific implant/prosthetic, or perhaps using medical imaging data to guide implantation of a device. Medical imaging can be used not only for prosthetic designs, but can serve as templates for organ scaffold construction. Medically, there exists a large need to provide alternatives for cadaveric allografts, autografts, and prosthetic implantations. For example in orthopaedic surgery, the number of patients receiving total hip and knee replacements in 1995 totaled 457,000 in the US alone and is expected to double by the year 2025 [57]. Although the number of patients affected is smaller, those awaiting liver transplant had a death rate of 8.3% in 1999 [58]. Similarly, patients awaiting a heart transplant have a 6 month mortality rate of 24 – 70% [59]. Facial reconstruction, though less life threatening, represents a cornerstone that interfaces cosmetic and reconstructive surgery to restore both functionality and aesthetic properties important to one's quality of life [60].

Regardless of applications, control of the geometry of transplanted tissue is important. Internally transplanted tissues need to fit into the desired space and conform to the surrounding tissues. As a result, surgeons are often required to manually alter the organs/tissues to “fit” the recipient whether it is a liver, heart, meniscus, or flap of skin. In addition to function, external tissue transplants require appearance to be taken into consideration as well. However, aesthetic appearance becomes a secondary objective to functionality and restoration of health, because no established treatment exists that meets all other primary criteria to prevent rejection, chronic pain and decrease mortality. Indeed some of the most exciting applications of TE technology have involved replication of anatomic geometry.

Some early examples in the field of tissue engineering have been successful in forming cartilage in the shape of a human ear [61], producing a bone-cartilage composite shaped as a mandibular joint [62], generation of a distal phalanx for thumb reconstruction [63], and anatomically shaped menisci for the knee [29]. In these cases, geometry was generated from molds taken from the intended tissue. These initial studies, while very important, are unlikely to be implemented on a wide scale for generating patient specific geometry on a case by case basis. An obvious solution would be using medical imaging to obtain the necessary information on the patient's specific anatomical needs. This article will present a brief review of the current methods used to replicate the complex tissues in the body.

2.3 Imaging Techniques

Anatomical geometries can be extracted from any medical imaging modality capable of rendering a 3D image, such as angiography, fluoroscopy, mammography, MRI, CT, μ CT, stereophotogrammetry (3D photogrammy), and ultrasound. While there exists a large selection of imaging modalities from which to choose, MRI and CT are the most widely used to visualize cardiovascular, musculoskeletal, neural, and dental tissues. However, each imaging technique may present distinct advantages for a specific application of tissue replacement.

MRI can readily register bone and soft tissues and has scan volumes that can range from as large as the human body to small precision scans that image the wrist and knee (Table 2.1). Scan times for an MRI range from 5 to 40 minutes with resolutions that increase with both scan time and magnetic coil strength. Resolutions for a 3T MRI have been reported as high as $250\mu\text{m} \times 250\mu\text{m} \times 0.5\text{mm}$. Scan time can be reduced with the use of higher powered magnetic fields, but human subjects are rarely exposed to fields greater than 3 Tesla (T). Exposure to a 7T MR coil can cause

higher incidence of discomfort and sensations of vertigo than lower strength MR coils [64]. While MRI scans are preferred over CT because there is no radiation exposure, it is important to note that there is a sizable percentage of the population that experiences uncomfortable anxiety and claustrophobia when having a full body MRI (Table 1).

Table 2.1: Image modality characteristics. * = other tissues can be imaged with the aid of contrast agents. Specifications for MRI, CT, and μ CT provided by Siemens Medical Solutions USA, Inc. Malvern, PA and GE Healthcare, formerly EVS Corporation, Ontario, Canada. 3D digital photogrammy specifications provided by 3dMD, Atlanta, GA and ultrasound specifications provided by Elliott and Thrush [65].

Imaging technique	Preferred tissue	Highest resolution	Scan time	Maximum volume	Safety/compliance
MRI (3T)	Soft tissue and bone	250 μ m \times 250 μ m \times 0.5 mm	5–40 min.	Human body	Anxiety/claustrophobia
CT	Bone*	0.24–0.33 mm	5 min. (8–40 sec of actual scan time)	Human body	Ionizing radiation
μ CT	Bone*	1 -200 μ m	2–4 hrs	Whole rat	Ionizing radiation
Ultrasound	All tissues	1 \times 1.5 \times 0.2 mm	10–15 min.	Blood vessel - neonatal	N/A
3D digital photogrammy	External structures (craniofacial)	150 μ m	<1 min.	Whole head	N/A

CT scans can generate higher resolution images than MRI (0.24 – 0.3mm), but can only image bone without the use of contrast agents (Table 2.1). 3D models are more readily generated from CT scans with little to no manual editing, where as MRI requires many manual techniques to acquire the geometry [66]. Scan times are much shorter for CT than for MRI, but this imaging technique requires the use of ionizing radiation. This presents a minimal but finite risk to individual patients, but collectively a much bigger risk to larger patient population.

μ CT has ultra high resolution (1-200 μ m), but is limited by the volume in which it can scan (Table 2.1). Due to the volume limitation of μ CT, it cannot be

considered non-invasive for animals larger than mice. Also, μ CT, like CT, will not readily register soft tissues in the absence of contrast agents, which may alter tissue structure or geometry.

Ultrasound can readily image most tissue and does not use ionizing radiation or require a person to be in an enclosed area. While scan times for ultrasound are short, it is limited in the resolution quality it can provide (1mm X 1.5mm X 0.2mm) [65]. Typical volumes that are scanned via ultrasound include small structures such as blood vessels to large ones such as neonatal infants (Table 2.1).

3D digital photogrammy can obtain high resolution images (150 μ m) in less than a minute (Table 2.1). 3D photogrammy is primarily used for external structures it is done in an open area so patients do not have to worry about the claustrophobia that is common to MRI. Further, there is no ionizing radiation associated with 3D digital photogrammy, unlike CT or μ CT.

The process for selecting the most appropriate imaging method is tightly coupled to the target tissue. For example, if the desire is to obtain medical imaging data from a patient to generate a femoral head, meniscus, or heart leaflet valve, three very different approaches would be used. In the case of the femoral head, while CT would provide the highest resolution image of the boney structure, it does not image cartilage or soft tissues readily. μ CT would not be used because the femoral head is too large to fit into current scanning devices. An MRI scan, on the other hand, could be used to obtain both the articular surface and boney structure without contrast agents.

In the case of the meniscus, the most medically relevant choice is MRI. High resolution images of the meniscus can be obtained via MRI by increasing the scan time. However, increased scan time increases cost and becomes a compliancy issue for the patient. The longer the patient is required to remain still during the scan the higher

the probability of geometry artifact due to movement. The alternative would be to excise the tissue from the joint, soak it in a contrast agent to allow for μ CT scanning. It is important to note that MRI can acquire geometries under loaded conditions whereas μ CT may have altered geometry due to being soaked in a contrast agent. In the case of the heart valve, MRI and CT both require contrast agents to visualize the inner workings of the heart and have similar image resolutions. Due to the high radiation exposure needed to perform a CT scan of the heart and the high expense associated with MRI usage, echocardiography (cardiac ultrasound) is becoming a more widely used noninvasive method to obtain 3D geometric models of mitral valves [67, 68]. However, to maximize resolution, the valve can still be excised, soaked in a contrast agent and scanned via μ CT.

2.4 Fabrication Techniques

Generating anatomically shaped engineered tissues does not require medical images. As mentioned earlier, many early TE efforts to generate anatomically shaped constructs used impression molds [61, 62, 69-72] to serve as negative templates. The paradigm shift to using medical images for CAD design has only very recently been established [29]. There are multiple methods to replicate anatomical shape through injection molding or different rapid prototyping techniques and for each method there exists an even larger choice of biomaterials to use as a scaffold. Choice of scaffold will dictate the design and fabrication process of the engineered tissue, which is driven by the application and tissue one is trying to generate. Here we will briefly take a look at some promising results across a number of different engineered tissues.

Injection Molding

As stated above, scaffold choice has a major role in guiding the fabrication process of generating TE constructs. Many traditional scaffold materials (e.g. polyglycolic acid fibers (PGA), polylactic acid (PLA), polycaprolactone (PCL)) require processing at high temperatures or in organic solvents to control shape. As such cells cannot be introduced until the scaffold has cooled and solvents have been removed. In contrast, materials such as hydrogels undergo phase transitions that enable maintenance of cell viability during gel formation. As such, cells can be introduced to these materials prior to molding.

Initial efforts in cartilage tissue engineering used acellular scaffolds and began with the simple geometries in the shape of triangles, rectangles and cylinders [71]. More complicated geometries were also achieved, such as a human ear using a synthetic nonwoven mesh composed of PGA [61]. The PGA mesh was molded into desired geometries through the use of plaster prosthetic mold, cells were then later seeded onto PGA scaffolds and allowed to culture subcutaneously in nude mice [61, 71].

Similarly, bone TE requires scaffolds with a high rigidity that emulates the physical properties of native bone. The processes involved in bone scaffold formation are often unfavorable for cell viability and therefore seeding of these constructs occurred after they were constructed. One such study successfully tissue engineered phalanges and small joints through the use of PGA and PLA [70].

The seeding of acellular scaffolds has also been applied to engineered cardiovascular tissue such as blood vessels and heart valves. In one promising study, PCL was electro-spun into the shape of a trileaflet valve using a custom designed aluminum template modeled after native tissue before being seeded with cardiac cells for in vitro culture [73].

While seeding cells after scaffold generation has produced promising results, this methodology is very time consuming and does not ensure equal cell distribution throughout the scaffold. A more efficient approach would be to seed scaffolds before they are formed, though this would require biomaterials with a non-toxic liquid phase that maintaining viability during the solidification or gelation process. Biomaterials that allow this approach include, but are not limited to, alginate, agarose, chitosan, collagen gel, fibrin glue, and poly(lactide-co-glycolide) (PLG). Some of the first such studies involved seeding chondrocytes into alginate [69]. The alginate-cell solution was cross-linked with CaSO_4 and injected into silastic impression molds of chin and nose implants for facial reconstruction. Using various cell seeding densities they were able to culture these implants in the back of nude mice for 30 weeks and maintain both shape and cell viability [69].

Uniform cell distribution becomes more critical when generating injection molds of larger constructs, such as the mandible for craniofacial reconstruction [69, 72] or the meniscus of the knee [29]. Seeding the scaffold while it is liquid enhances homogeneity of cell distribution upon initial construct formation. CAD-based injection molds have been used to design a wide array of geometries from very small volume structures such as tympanic membrane patches (3 μL) [74], and engineered heart valves (~ 1 mL) [75], to larger sized tissues such as the meniscus (2-5 mL) [29]. The resolution for injection molding has been reported to be 600 μm [76].

Injection molding techniques, while not optimal for multi-material constructs, can be altered to generate more complex tissues. A prime example is the production of an anatomically shaped osteochondral construct based on stereophotogrammetry data via injection molding [77]. Patellar shaped composites were made possible through computer numerical control (CNC) milling of demarrowed bone blocks that fit into a mold allowing for injection of cell seeded agarose resulting in partially integrated

bone plugs [77]. Another composite injection moulding study by Mizuno *et al.* produced both a multi-material and multi-cellular TE intervertebral disc [78, 79]. The IVD was composed of an annulus fibrosus (AF) made from PLA/PGA scaffold and a nucleus pulposus (NP) made from calcium cross-linked alginate that was injected into the center void of the PLA/PGA scaffold. Each region was composed of its respective cell type and exhibited both biochemical and mechanical properties similar to that of native tissue [78, 79].

One of the most recent advances in generating patient specific implants via injection molding were achieved using alginate and meniscal fibrochondrocytes from bovine knees [29]. The geometry was obtained using both MRI and mCT scans of sheep knees and used to produce CAD moulds that were 3D printed out of Acrylonitrile Butadiene Styrene (ABS) plastic. Alginate-cell solution was cross-linked with CaSO_4 and cultured for up to 8 weeks *in vitro*. Anatomical shape was retained and constructs had both mechanical and biochemical properties similar to that of native tissues [29] (Fig. 2.2A). Future efforts are now focusing on stimulating extracellular matrix (ECM) production as well as evaluation of geometric fidelity based on imaging type and time in culture.

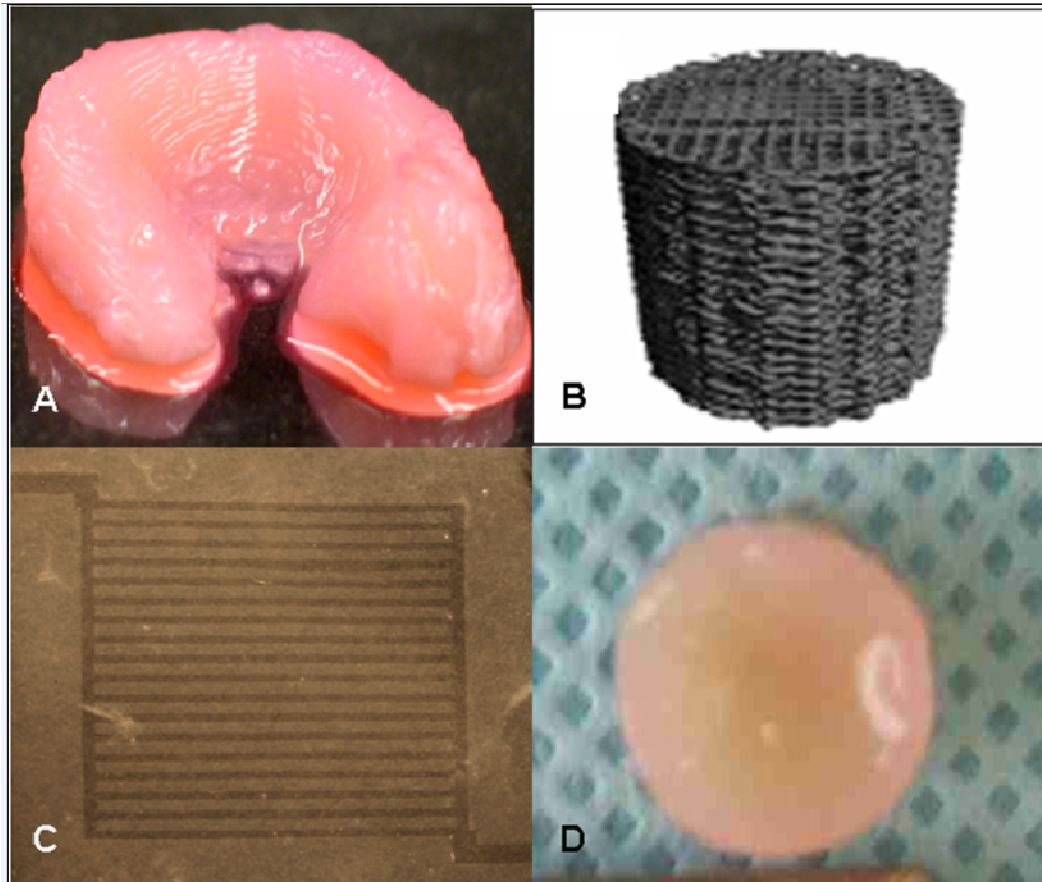


Figure 2.2: (A) An injection molded meniscus derived from a μ CT scan and fibrochondrocyte seeded alginate after 8 weeks of *in vitro* culture [29]. (B) Medical grade PCL composite formed via fused deposition modeling (Image provided by Dr. Dietmar Hutmacher, Queensland University of Technology, AU). (C) Chondrocyte seeded alginate micro-channel network with $50 \times 50 \mu\text{m}$ channels spaced $100 \mu\text{m}$ apart [80]. (D) Cartilaginous disc 1 cm in diameter composed of PLG micro-beads seeded with chondrocytes after 8 weeks of *in vitro* culture [81].

Rapid Prototyping

Rapid prototyping has many different variations (Table 2.2). The basis for this technique is to produce usable scaffolds in a short time scale (i.e. hours to days). Solid

freeform fabrication (SFF) and 3D printing are two of the more popular rapid prototyping techniques that are capable of generating multi-material and multi-cellular anatomical constructs. Hutmacher and Cool have nicely reviewed applications of SFF on bone tissue engineering in this journal [82] (Fig 2.2B).

Most bone TE methods involve seeding of acellular constructs or insertion of acellular implants with the expectation of cellular ingrowth *in vivo*. Some successful studies include the use of porous coral in the shape of a distal phalanx seeded with periosteal cells for thumb reconstruction [63], 3D printing brushite implants [83] and a cranial segment [84] using tricalcium phosphate (TCP) and tetracalcium phosphate respectively. Shek et al. used localized gene therapy to increase and localize cellular and tissue ingrowth using a SFF polypropylene fumarate/TCP composite that provided a stable matrix that could be matched to specific patient defect geometry [85]. Work by Sherwood et al. in conjunction with Therics, Inc. produced osteochondral composites using TCP combined with either PLG or PLA for the chondral surface [86]. The composite structure exhibited region specific mechanical properties and integration between the two biomaterials making it suitable for implantation [86]. Therics, Inc. also has a number of other TCP based therapeutic products that are currently undergoing clinical studies. SFF techniques are able to produce patient specific scaffolds that can be modified to increase and guide cellular in growth through variation of surface roughness, chemically bonded growth factors, and altered scaffold porosity [82].

Table 2.2: Fabrication techniques and the various biomaterials used for cell seeded scaffolds and acellular scaffolds as well as multi-cell/material capability and current resolution capabilities.

Fabrication techniques	Variations	Seeded biomaterials	Non-seeded biomaterials	Multi-material/ multi-cell capable	Resolution
Moulding	Injection moulding	Alginate	PCL	No	600 μm
	Electro spun moulding	Agarose	PGA		
		Chitosan	PLA		
		Collagen			
		Fibrin glue			
PLG					
Rapid prototyping	SFF	Alginate	PEG	Yes (but not CNC milling)	250 μm
	3D printing	Agarose	Porous coral		
	CNC milling	Chitosan	TCP		
		Collagen	Tetracalcium phosphate		
Lithography	N/A	Alginate	Silicon	Yes	25 μm
		PEG	PEG		
		Collagen	PLG		
		Matrigel	PVA		
		Agarose	Collagen		
Sintering	N/A	PLG	PLG	No	40–600 μm
			PVA		
			HA		
			TCP		

For more heterogeneous tissues, such as the meniscus, heart valve and liver, control over spatial and temporal differences in cell type/morphology and mechanical properties is necessary. Achieving structures that have the necessary cell distributions and biomechanical properties is a major challenge. Cytoscribing, as termed by Klebe involved alternating deposition of layers of cells and materials to generate 2 and 3D tissues [87]. Klebe established this technique using a variety of different cell types from different species and bound them to substrates using fibronectin that was deposited via Hewlett Packard graphics plotter of ink jet printer [87]. More recently several groups have demonstrated simultaneous co-deposition of cells and materials. An excellent example of this is by Cohen et al. via SFF using alginate and chondrocytes [88]. The work established the ability to print cell seeded alginate using different materials (i.e. two different grades of alginate) and in different structurally sound shapes including a disc, crescent, and meniscus based on μCT data with

printing resolution of 720 μm [88] (Table 2.2). Rapid prototyping has also been used in the fabrication of 3D hepatic tissues with complex internal microstructure. Constructs were generated using both multi-cell and multi-material as means to improve nutrient transport [89]. Cell printing efforts by Chang et al. have evaluated cell viability of HepG2 cells based on dispensing pressure and nozzle diameter with calcium cross-linked alginate [90] and combined these SFF techniques with lithography methods to generate 3D microorgans [91]. The microorgans had vascular networks serving as pharmacokinetic models and were able to replicate consistent prints with 250 μm resolution [91] (Table 2.2).

Lithography

The transport of solutes and removal of waste products is a large concern in TE, especially when trying to engineer large volume tissues or engineering organs like the liver. In the body this solute transport is accomplished primarily by the vascular system, which is effectively a network of perfused micro channels. Traditionally, engineered scaffolds have relied on the host to provide vascularization [92]. Lithography techniques have been applied to tissue engineering to produce predefined vasculature. Preliminary studies using a PDMS substrate established the efficacy of this technique using both hepatocytes and endothelial cells [92]. Other biomaterials used in lithography TE efforts include polyvinyl alcohol (PVA) with fibroblasts [93], PCL and PLG with vascular smooth muscle cells [94], PEG with osteoblasts [95] and embryonic stem cells [96], matrigel with epithelial [97] cells and fibroblasts [98], as well as collagen and agarose with fibroblasts [98]. Other work done by Khademhosseini et al. generated 3D micropatterned substrates consisting of

hyaluronic acid and fibronectin seeded with cardiomyocytes which aligned along the interface between the scaffold and glass substrate [99].

Recent innovative studies using chondrocytes seeded in alginate have shown great promise in their ability to generate various micro-fluidic patterns via laminated sheets with sealed channels as small as 25 μm X 25 μm [80, 100] (Table 2.2). After 4 weeks in culture laminated sheets integrated well with no visible interface [101] (Fig 2.2C). This work by Choi and coworkers really demonstrates the resolution of image based TE and can be implemented to produce larger volume constructs that not only have a custom circulation network, but a network that can be controlled spatially with gradients of nutrients, growth factors, and region-specific flow rates [80, 100, 101].

Sintering

The deposition of micro-particles or micro-beads to alter surface properties or to build up structures is known as sintering. Sintering has become a valuable fabrication technique that allows designation of specific localized properties that control for porosity, surface chemistry, and mechanical properties. Most sintering efforts have focused on its application to bone TE through the use of PVA [102], hydroxyapatite (HA) [102], TCP [103], and PLG [104]. Studies have shown improved osteoblast cell growth throughout the sintered matrix [104].

Other works done with PLG and its application to cartilage tissue engineering have shown its ability to be used as a moldable scaffold [81] capable of cellular proliferation and infiltration *in vivo* [105] (Fig 2.2D). The use of sintering cell seeded PLG micro-beads in combination with free chondrocytes can be used to address focal defects *in vivo*. Furthermore, integrating the use of image guided tissue engineering bead-cell mixtures can be deposited to repair articular surfaces to their original

geometry before injury. The repair resolution of this technique is only limited by the consistency and size of the micro particles/bead which can range from 40 – 600 μm [81, 102-105] (Table 2.2).

2.5 Conclusions

Image guided tissue engineering shows great promise for the generation of patient specific engineered tissues. CT and MRI can provide adequate templates for custom, patient-specific implants. Other imaging modalities do hold promise but have yet to be established. While most image based efforts have focused on musculoskeletal tissues, image-based templates are starting to be used for cardiovascular models and small scale micro-vascular channels for hepatic tissues via CAD. The methods for generating these constructs vary greatly depending on the scale, tissue type and biomaterial. There exists the possibility to not only generate constructs that mimic the gross anatomy, but also generate proper substructure and networks of the desired tissue.

Both injection molding and SFF techniques can generate anatomically shaped tissue engineered constructs that appear to have high geometric fidelity. A major challenge to all who work on image-guided tissue engineering lies in the lack of methods to quantify shape fidelity of fabricated implants. Similarly, there is essentially no data describing how shape fidelity is maintained throughout culture whether *in vivo* or *in vitro*. These issues are complicated by the fact that there is still no established technique for evaluating shape fidelity of anatomically shaped TE constructs. The topic of shape fidelity is still in dire need of further investigation, because for many of these complex shaped tissues such as the meniscus [24, 106, 107] or heart valve [108, 109] critical dimensions and tolerance levels for implantation are still being debated.

It is clear that medical imaging is an excellent tool to quantitatively define the geometry of structures especially *in situ*, such as the meniscus or heart valve. Now with new advances in medical imaging techniques, location specific microstructure can be extracted as well. 3D printing can provide the ability to create tissue-specific properties that vary with location within the tissue/organ (i.e. cell type, mechanical properties, porosity, etc.) which would otherwise not be possible with injection molding. Spatial properties can be gathered from medical images to aid in the construction of engineered tissues. MRI [110] and μ CT [111] have been used to look at GAG concentration in cartilage, CT to look at bone density and trabecular architecture [112], second harmonic generation microscopy to look at collagen fiber orientation [113] and density [114]. Combining imaging data techniques with rapid prototyping could allow generation of anatomical structures *in situ* with region specific microstructure similar to that of native tissues.

Imaging tools and fabrication techniques have enhanced fabrication of engineered constructs, but on the list of tissue engineering goals this seems to be only the tip of the iceberg. How exactly does one go from a newly fabricated construct and produce engineered tissues ready for implantation? Even without considering shape fidelity, quality control for TE implants involves confirming that these tissues have the appropriate biochemical composition and mechanical function. For dynamically loaded tissues such as the heart valve or meniscus, complicated geometry often results in complicated mechanics. For years, medical imaging has been used to extract geometries of bones, muscles, and cartilage to develop constitutive models to better describe the inner workings of joints in the body through finite element modeling (FEM). Medical imaging combined with FEM will continue to play a major role in assessing the functionality and durability of engineered tissues. As new knowledge is

acquired about *in vivo* behavior through FEM simulations, engineered tissues can be specifically conditioned *in vitro* to withstand these stresses.

The idea of *in vitro* conditioning is becoming more and more popular not only for engineered tissues such as tendon [115], heart valve [116], bone [117] and cartilage [118], but for cadaveric explants as well [48, 118]. Exposure to limited *in vivo* like stimuli in a reduced or gradual manner has shown to be beneficial to cells and resulted in increased ECM formation as well as corresponding improvements in mechanical behavior. Optimal *in vitro* conditioning settings have yet to be elucidated, but as it stands now the time scale for generating functional tissues is lengthy.

Nonetheless image-guided tissue engineering is still likely a very valuable tool for generating patient specific tissues and organs. Challenges still lie in the ability to integrate these techniques to engineer large volume tissues with micro-vasculature and generate proper ECM organization and alignment. These techniques in combination with *in vitro* conditioning will enable the generation of spatially complex and more functional tissues.

CHAPTER 3

IMAGE-GUIDED TISSUE ENGINEERING OF ANATOMICALLY SHAPED IMPLANTS VIA MRI AND MICRO-CT USING INJECTION MOLDING

Published in *Tissue Engineering*² [29]

3.1 Abstract

This study demonstrates for the first time the development of engineered tissues based on anatomic geometries derived from widely used medical imaging modalities such as computed tomography (CT) and magnetic resonance imaging (MRI). Computer-aided design and tissue injection molding techniques have demonstrated the ability to generate living implants of complex geometry. Due to its complex geometry, the meniscus of the knee was used as an example of this technique's capabilities. MRI and microcomputed tomography (μ CT) were used to design custom-printed molds that enabled the generation of anatomically shaped constructs that retained shape throughout 8 weeks of culture. Engineered constructs showed progressive tissue formation indicated by increases in extracellular matrix content and mechanical properties. The paradigm of interfacing tissue injection molding technology can be applied to other medical imaging techniques that render 3D models of anatomy, demonstrating the potential to apply the current technique to engineering of many tissues and organs.

3.2 Introduction

A major advantage to tissue engineering technologies is that they enable the generation of tissue in specific shapes. Shape generation is critical for craniofacial

² Ballyns JJ, Gleghorn JP, Niebrzydowski V, Rawlinson JJ, Potter HG, Maher SA, Wright TM, and Bonassar LJ. Image-guided tissue engineering of anatomically shaped implants via MRI and micro-CT using injection molding. *Tissue Eng Part A* 2008;14:1195-1202.

[119] and plastic surgery [120] applications as well as orthopaedic applications [23, 121] where joint conformity is required. Efforts to engineer tissue in anatomic shapes have shown promise, including forming cartilage into the shape of a human ear [61], injecting periosteal cells into porous coral in the shape of a distal phalanx for thumb reconstruction [63], generating a bone-cartilage composite shaped as a human mandibular joint [62], creating anatomically shaped patellar articular cartilage using stereophotogrammetry data [77], and forming phalanges and small joints through selective placement of bone and cartilage cells into a biodegradable synthetic polymer scaffold [70]. Recurring challenges in these methods include the accuracy, speed, and reproducibility of the process by which these implants are made. For example, methods to create anatomic geometries by molding polyglycolic acid (PGA) or polylactic acid (PLA) [61, 122] or carving of ceramic implants [63] require extensive time for implant fabrication, and separate procedures for cell seeding are inefficient. Other procedures involving 3D printing of anatomically shaped scaffolds have faced similar challenges in efficiently localizing cells on the scaffolds [123]. No method currently exists for rapidly incorporating patient specific geometry into tissue engineered implants.

Injection molding techniques could provide an innovative approach to generating implants of complex geometry in a much shorter time [69, 72]. Previous work showed that computer-aided design (CAD) can be combined with tissue injection molding technologies to fabricate very small, precise, cell seeded alginate structures that maintain shape fidelity throughout *in vitro* culture [74]. CAD-based techniques have also been applied to casting osteochondral constructs with conformal joint surfaces [77]. However, no study has yet demonstrated an ability to produce cell-seeded geometries derived from clinically used imaging modalities.

The goal of this study was to apply CAD tissue injection molding techniques to engineer a whole meniscus. Medically, injuries to the meniscus pose a relevant clinical problem with over 750,000 meniscal surgeries conducted each year, the most common treatment for which is partial or total removal of the injured tissue (i.e. meniscectomy) [23]. Current meniscal tissue engineering efforts have focused on developing repair methods through the use of mesenchymal stem cells [124] to address point defects and using scaffolding materials such as a collagen-based meniscus implant [125, 126] to aid in regeneration of complex tears and defects. The concept of using fibrochondrocyte seeded scaffolds for generation of meniscal tissue has been demonstrated with several scaffolding materials including agarose gels [31], non-woven PGA meshes [37], and polyethylene terephthalate scaffolds [127]. Further, exposing these constructs to different growth factors [31] and media mixing culture conditions [37, 127] has been used to stimulate meniscus tissue growth.

Cadaveric meniscal allografts are clinically used, but this method of treatment suffers due to the scarcity of donor tissue, difficulties in matching the native joint architecture and the risk of disease transmission. Matching the size of the native meniscus is of particular importance to ensure the appropriate distribution of pressure across the joint. Image guided TE of the meniscus address the existing issues associated with meniscal allografts. There have been very few studies that attempt to engineer whole menisci [27, 128], which could be due to the large size of these constructs and difficulty in replicating its complex geometry.

The current research focuses on the incorporation of standard medical imaging tools, specifically magnetic resonance imaging (MRI) and computed tomography (specifically for the current work, microcomputed tomography or μ CT), to design templates for tissue engineered implants. Both of these imaging methods are commonly used for diagnosis and monitoring of tissue disease and thus could be easily

incorporated into the process of designing therapies. While MRI is commonly used for diagnosis of soft tissue injuries, issues of resolution and thresholding are challenging in delineating the meniscus from adjacent soft tissue. In contrast, CT/ μ CT is not typically used for soft tissue imaging, but had necessary resolution to facilitate tissue delineation. To test the feasibility of using MRI and μ CT imaging data for tissue engineering, an injection molding system was designed based on these imaging modalities and constructs generated by this technique were cultured for 8 weeks and monitored by gross shape inspection, assessment of compressive mechanical properties, quantification of biochemical composition, and analysis of ECM localization by histology.

3.3 Materials and Methods

Imaging

Magnetic resonance imaging of 5 skeletally mature sheep knees (donated by Dr. Simon Turner; Colorado State University) was performed on a clinical 3T MR unit (Twin Speed, General Electric Health Care, Milwaukee, WI) using a commercially available, 8 channel, receive-only knee coil (In vivo, Milwaukee, WI). Sagittal fast spin echo (FSE) sequences were acquired with a repetition time (TR) of 4800 ms, echo time (TE) of 26.8 ms (effective), echo train length of 12, field of view of 13cm, matrix of 512 x 416, and slice thickness of 2.0 mm with no gap, resulting in a spatial resolution of 253.9 μ m (frequency) x 312.5 μ m (phase) x 1 mm, at three excitations. Phase direction was superior to inferior and receiver bandwidth was 62.5 kHz over the entire frequency range.

In addition, sagittal three-dimensional spoiled gradient echo (SPGR) sequences were acquired with selective water excitation, using a flip angle of 10 degrees, TR of

16.8 ms, TE of 4.1 ms, field of view of 13 cm, matrix of 512 x 512, and slice thickness of 0.5 mm with no gap, resulting in a spatial resolution of 253.9 μm (frequency) x 253.9 μm (phase) x 0.5 mm at one excitation. Receiver bandwidth was again 62.5 kHz over the entire frequency range.

The medial meniscus from each knee was dissected, soaked in Omnipaque® Iohexol 300 mg I/ml contrasting agent for two hours, and μCT scanned using an Enhanced Vision Systems Model Ms-8 In Vitro Micro-CT Scanner (GE Healthcare, formerly EVS Corporation, Ontario, Canada). The scans were taken using short scan x-ray settings of 70kV, 90mA, 3000 ms exposure time, with 400 views, and 0.023 mm/pixel resolution. Scans were calibrated using values for bone, air, and saline. Sheep menisci were the largest animal menisci that would fit into the μCT core, and were thus used for both imaging modalities.

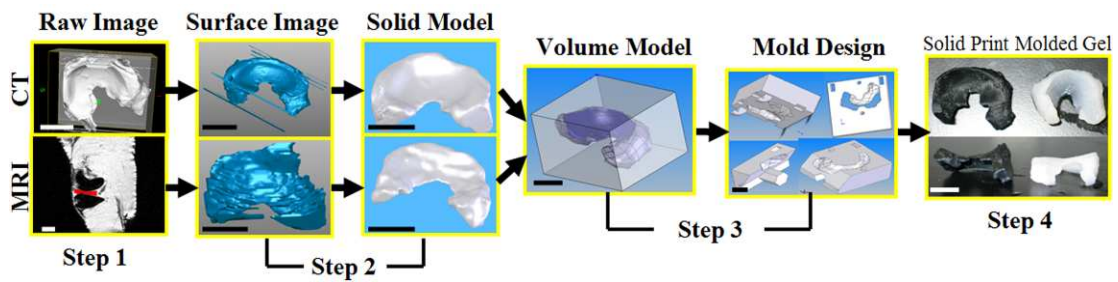


Figure 3.1: Image processing steps for CT and MRI scans of an ovine meniscus being converted from its raw form to a surface image (step 1), then cleaned and converted to a solid model (step 2), and imported into CAD software for mold design (step 3). The embedded meniscus generated a suitable mold that achieved good shape fidelity as compared with the solid printed model (step 4). Scale bar=10 μm .

Mold Design

MRI data sets in DICOM format were viewed and manually segmented for isolation of the meniscal area (Fig. 3.1: Step 1). Isolated meniscal segments from DICOM files were used to render a 3D representation in a point cloud image (SliceOmatic v4.3; TomoVision). Conversion of the point cloud image to a surface image allowed for formatting and generation of a solid model (Geomagic Studio 4.0; Raindrop). The meniscus was then ready to be imported into CAD and be employed for mold design.

The μ CT scan was visualized as a surface image (MicroView) and exported for processing and file conversion. Upon conversion to a solid representation (Geomagic Studio 4.0), the image was used for mold design in CAD (SolidWorks Educational Edition) or converted to an STL file to 3D print an ABS plastic replica of the tissue on a fused deposition modelling platform or FDM 3000 machine (Stratasys; Eden Prairie, MN).

The CAD mold design process was identical for both μ CT and MRI (Fig. 3.1). The image of the solid meniscus was embedded into a block and served as a virtual negative for the mold. The block was divided into 4 sections that allowed for removal of intact meniscus constructs from the mold. Molds were printed using a FDM 3000 machine.

Injection Molding

Using previously developed methods [69], the meniscus was removed intact from 1-3 day old bovine knee joints (Gold Medal Packing; Oriskany, NY) and diced into 1 mm³ cubes. Bovine cells were used instead of sheep cells because they were the most readily available and consistent cell source. The tissue was digested overnight in

0.3% collagenase, 100 µg/ml penicillin, and 100 µg/ml streptomycin in Dulbecco's Modified Eagle Medium (DMEM) (Gibco; Invitrogen Corporation, Grand Island, NY). The following day the cells were washed, isolated, and counted. Viability ranged between 82 and 87%. To generate the 50 molded constructs in this study, cells from 52 menisci and 16 animals were harvested. The 50 constructs were produced in 9 batches with each batch containing cells pooled from 1-2 animals and 4-8 menisci. The engineered constructs made from these 9 batches were distributed randomly across time points.

Cells were then seeded at 50 million cells per mL in 2% LVG alginate (FMC Biopolymer; Drammen, Norway), mixed with CaSO₄ (Sigma-Aldrich, Inc.; St. Louis, MO) at 0.02 g/ml to crosslink the alginate, and injected into meniscus molds. This cell seeding density was chosen based on prior studies using injection molding technology to deliver articular chondrocytes. The current cell seeding density was optimal for tissue growth in articular chondrocytes [69, 72, 74, 129]. The alginate remained in the mold for 20 minutes to allow for sufficient crosslinking before removing the gel structure from the mold. Average molded construct size was 25.3mm x 17.4mm x 6.6mm (length from the outside of each horn x average width from the front of the horn to the back of construct x height). Samples were placed into static culture for up to 8 weeks in culture media composed of DMEM, with 10% FBS, 100 µg/ml penicillin, and 100 µg/ml streptomycin.

Biochemistry

Native and engineered samples harvested at 0, 1, 2, 4, 6, and 8 weeks were photographed, cut into cross-sections and photographed again. 6mm diameter by 1mm thick discs were biopsied from cultured menisci as well as from native tissue. The

discs were cored from similar locations in both engineered and native tissues and used for biochemical analysis or mechanical testing. Other cross-sections were fixed for histology. Samples reserved for biochemical analysis were weighed, frozen, lyophilized, and weighed again. Lyophilized discs were digested in 1.25 mg/mL papain solution overnight at 60°C [130]. Papain digests of tissue engineered constructs and native controls were analyzed for DNA content via Hoechst DNA assay [131], glycosaminoglycans (GAG) through a modified DMMB spectrophotometric assay done at pH 1.5 [132], and collagen content via hydroxyproline assay [133]. Nine samples per meniscus were gathered for biochemical analysis of extracellular matrix (ECM) composition.

Histology

Cross-sections of molded constructs were fixed in 10% buffered formalin with 1mM CaCl₂ to prevent gel solubilization [134]. Fixed sections were then stained with Safranin-O at pH = 2.0 to observe GAG formation. Sections were then stained with picrosirius red to observe collagen localization.

Mechanical Testing

Discs (6 mm diameter, 1mm thick) were tested in confined compression to determine the equilibrium modulus (EnduraTech; Electroforce (ELF) 3200 System, Minnetonka, MN). As described previously [69], stress relaxation tests were performed by imposing 10 steps of 50 µm on the gels and native controls with resultant loads fit to a poroelastic model to calculate the equilibrium modulus.

Statistical Analysis

Data were analyzed by 1-way ANOVA to detect differences in aggregate modulus, GAG, collagen, and DNA content over time using $p < .05$ as a threshold of statistical significance. Times points that were found to be significantly different were then further analyzed through post-hoc comparisons with the Bonferroni correction. All statistical analyses were implemented with Sigmastat version 3.0 (SYSTAT; San Jose, CA), and all data expressed as mean \pm SEM.

3.4 Results

Inspection of cross-sections demonstrated increases in opacity of the construct with time in culture, indicative of ECM deposition. This matrix deposition was heterogeneous with more pronounced opacity in the center. Gross inspection of MRI and μ CT generated models (Fig. 3.1: Step 4) indicate that both imaging modalities can serve as a template for mold design. While the μ CT model has excellent surface resolution compared to MRI, MRI imaging produced anatomically similar geometries with superior fibrocartilage-bone contrast. There were no significant differences between samples made by MRI and μ CT (data not shown). Samples shown are representative of both. Anatomically shaped constructs retained shape for the duration of culture with ~87% (33/38) remaining as intact constructs (Fig. 3.2A). Although quantitative volume measurements were not taken, gross inspection did not reveal any changes in size. Whole construct weights were not measured due to fragility of constructs at early times.

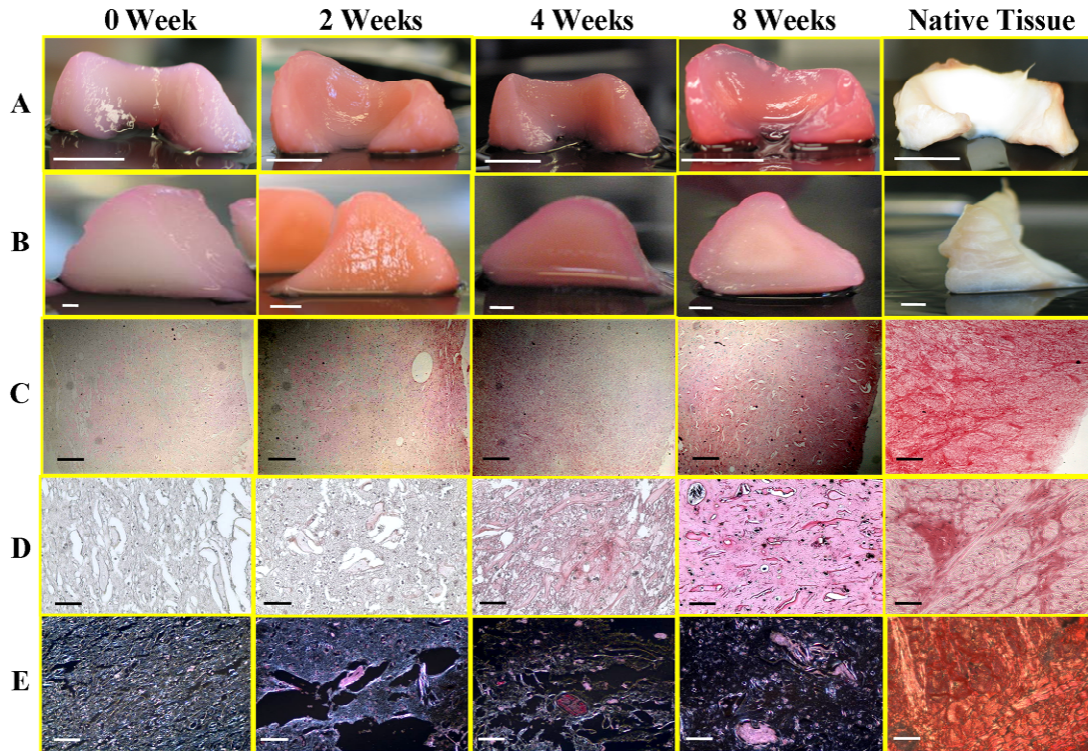


Figure 3.2: Photographs of (A) intact implants, (B) cross-sectional views, (C) tissue sections stained with Safranin-O at 40x original magnification, (D) tissue sections stained with Safranin-O at 200x original magnification, and (E) tissue sections stained with picrosirius red at 200x original magnification for engineered cartilage at 0, 2, 4, or 8 weeks and native meniscal tissue. Scale bars represent (A) 10 mm, (B) 2 mm, (C) 500 μm , and (D, E) 100 μm .

Safranin-O staining of engineered tissue cross-sections demonstrated progressive proteoglycan deposition, with spatial patterns of staining that were consistent with observations of opacity from gross inspection of cross-sections (Fig. 3.2B&C). Picrosirius red staining of sections from the molded constructs revealed progressive deposition and orientation of collagen across eight weeks of culture (Fig. 3.2D), trending toward the highly organized matrix of native meniscus.

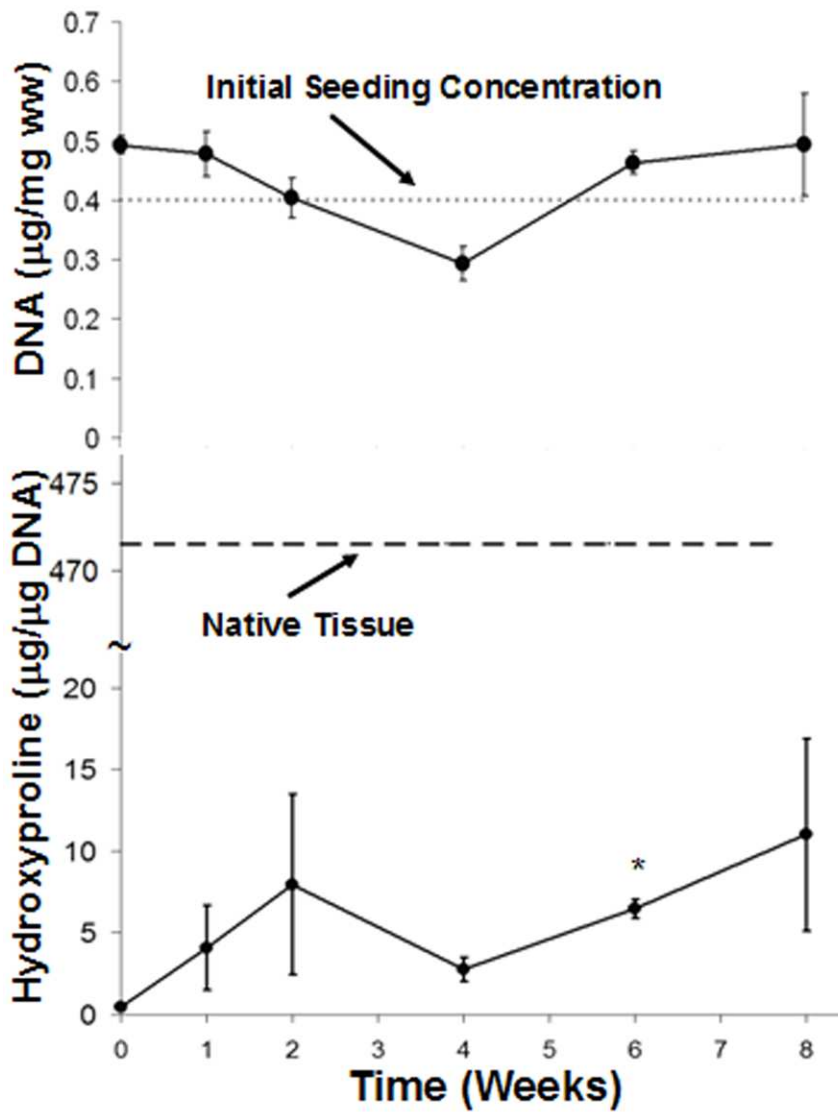


Figure 3.3: Temporal changes in DNA content and hydroxyproline content in tissue-engineered menisci and native meniscus. Data represent mean±SEM for n=5–8 samples.

Progressive tissue formation, as indicated by the accumulation of ECM, occurred throughout the entire culture period. Cell density as indicated by DNA content did not vary with time (Fig. 3.3) and remained within 25% of the initial seeding density. Collagen content indicated by hydroxyproline content (Fig. 3.3)

increased significantly up to 6 weeks ($p < .05$). At 8 weeks engineered tissue containing approximately 2.3% of the collagen found in tested native tissue controls normalized to DNA. At 4 and 8 weeks, a significant increase in GAG content ($p < .05$) occurred, reaching 36% that of native tissue controls (Fig. 3.4). The equilibrium modulus in the engineered menisci reached 50% of the native tissue controls at 6 weeks and showed significant increases in modulus at 6 ($p < .01$) and 8 weeks ($p < .05$). Tests of native tissue controls yielded values for hydroxyproline content [134, 135], GAG content [135, 136], and equilibrium modulus [9, 10, 135] similar to those reported previously.

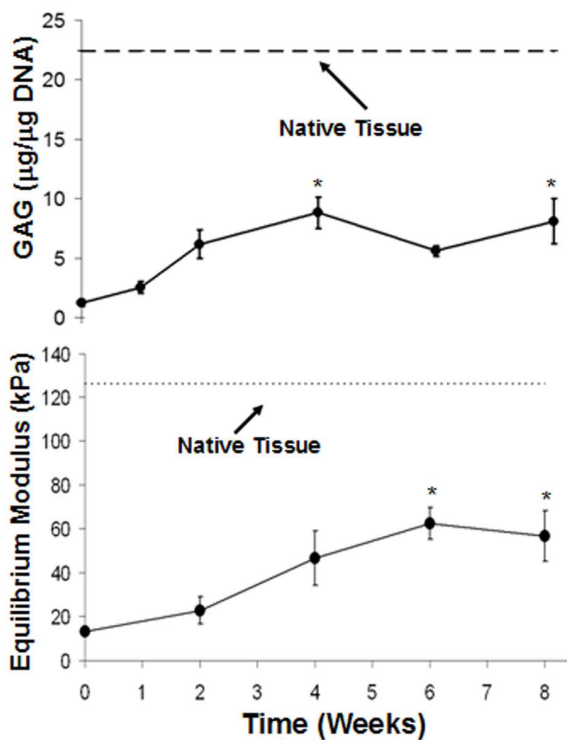


Figure 3.4: Temporal changes in GAG content and compressive equilibrium modulus in tissue-engineered menisci and native meniscus. Data represent mean \pm SEM for n=5–8 samples.

3.5 Discussion

This study established the design of an injection molding system based on medical imaging data to produce tissue engineered constructs that reproduced the geometric properties of native tissue. Injection molded samples retained geometry over 8 weeks in culture. The few constructs that did fail did so due to tears formed when removing constructs from molds, which propagated when being moved in and out of the incubator for media changes. Progressive tissue formation was demonstrated by monotonic increases in ECM content and mechanical properties. After 8 weeks, the compressive modulus of engineered tissue was ~50% that of native meniscus. These results demonstrate the ability to use patient specific geometry to rapidly engineer tissue, a feature unavailable in other current tissue engineering methods.

GAG and collagen contents after 8 weeks were similar to other studies [27, 31, 37, 127]. Unlike culture studies of meniscal fibrochondrocytes in agarose gels [37], no significant cell loss or cell death was observed. DNA content did not significantly change over the course of this study. Consistent with previous studies documenting delivery of articular chondrocytes by injection molding in alginate [69, 74]. Further cell distribution was uniform throughout culture, suggesting that there were no regions of central necrosis even in these relatively large samples (Fig. 3.2). In contrast to other studies, ECM loss did not occur at later time points as seen in PGA meshes [37]. The continuing problem remains in the ability to generate mechanically equivalent tissues to that of a native meniscus [27, 37, 128]. Upregulating collagen production could provide increased mechanical stability and aid in decreasing GAG loss to the surrounding media [37]. The confined compression modulus determined in the current study is thought to relate primarily to GAG content [137, 138]. Indeed the GAG/DNA has 36% of native meniscus and equilibrium modulus was 50% of native. Clearly collagen content was lower, but this would likely be reflected in other testing

geometries such as tension or shear, that were not reported here. No ascorbic acid was added to the culture medium in this study, which could explain why collagen content was low. Studies that have implanted engineered meniscal scaffolds into an animal model [27, 128] have had varying results, all of which suffer from a mismatch of mechanical properties and accurate geometry. Application of the technologies presented in this study could aid in the process of guiding meniscal constructs to reach their proper mechanical function.

Unlike the studies described above, the current experiments focused on reproducing meniscal geometry with tissue engineered meniscus. A consequence of this approach is the development of spatial gradients within tissue constructs with time in culture. Gross morphology and histology show inhomogeneities in ECM accumulation with more tissue localized in the center. Even though our engineered constructs were relatively large in size compared to other studies [31, 37, 127], this is inconsistent with central necrosis or nutrient deposition. The preferential accumulation of ECM in the center of these constructs could be due to a lack of ECM loss to the media compared to the surface. The centers of these constructs were probably hypoxic, and previous studies show that low O₂ enhances ECM formation for articular chondrocytes [139] as well as meniscal fibrochondrocytes [140]. Future studies will characterize spatial and directional properties in these samples to understand the effects of heterogenous matrix accumulation in engineered 3D anatomical structures.

While the process of generating anatomically shaped cell-seeded menisci does appear to be manpower heavy, the total time from start to finish was approximately 10 hours, half of which was for image processing. Production time can be greatly reduced by auto-segmentation algorithms to extract data from MRI images, improved editing functions to aid in formatting and conversion to a solid model, and automated algorithms for mold design in CAD software. However, even with the current system

described here, clinical deployment time between imaging for diagnosis and surgical therapy would likely be days to weeks, which would be adequate time to design an implant.

The success of image based injection molding in medicine relies on integrating the use of clinically relevant field strength MRI and other accepted imaging techniques. Further, through use of diffusion tensor imaging, the ability to map orientation through fractional anisotropic mapping and microstructural features of soft tissues [141] may make MRI the preferred modality for design and assessment of structures such as meniscus. μ CT images are typically used to image dense tissue, but was used in this study to obtain a high resolution template for construct generation. While MRI imaging would more likely be used in a clinical setting, it is possible that μ CT could be used. Palmer and coworkers have established a technique to visualize articular cartilage in vitro with μ CT with contrast agents that may be used in vivo [111].

Obtaining high geometric fidelity can be of great importance, especially for the meniscus where a deviation by more than 10% in meniscal size matching [24] can result in detrimental loads across the joint. Due to the complex geometry of the meniscus, correct size matching to restore normal contact pressure is no trivial task. Current efforts are being made to denote the critical geometric parameters of the meniscus [106] as well as improve the allograft matching process [107]. Lastly, efforts are being made to quantify geometric accuracy of injection molds compared to native tissue. Geometric quantification will also aid in tracking shape fidelity over culture time.

The interface of tissue injection molding technology is not limited to μ CT and MRI, but can be applied to any other medical imaging technique that has the ability to render a 3D model, including angiography, fluoroscopy, mammography, and

ultrasound. Similarly, the injection molding technique presented here is not limited to the use of alginate as a scaffold material and could be adopted for use with other common tissue engineering scaffolds such as collagen, agarose [77], chitosan, or PLG [81]. Further, the combination of tissue injection molding with medical imaging is not limited to musculoskeletal tissues. The meniscus was chosen as an example of the capabilities of this technique due to its complex geometry. Given the promise demonstrated in this study, the potential exists to apply the current technique to engineering of many tissues and organs, including cartilage, bone, skeletal muscle, cardiac muscle, and neural tissue.

CHAPTER 4

AN OPTICAL METHOD FOR EVALUATION OF GEOMETRIC FIDELITY FOR ANATOMICALLY SHAPED TISSUE-ENGINEERED CONSTRUCTS

Published in *Tissue Engineering Part C: Methods*³ [142]

4.1 Abstract

Quantification of shape fidelity of complex geometries for tissue engineered constructs has not been thoroughly investigated. The objective of this study was to quantitatively describe geometric fidelities of various approaches to the fabrication of anatomically shaped meniscal constructs. Ovine menisci (n=4) were imaged using MRI and μ CT. Acrylonitrile butadiene styrene (ABS) plastic molds were designed from each imaging modality and 3D printed on a Stratasys FDM 3000. Silastic impression molds were fabricated directly from ovine menisci. These molds were used to generate shaped constructs using 2% alginate with 2% CaSO₄. SFF (Solid Freeform Fabrication) was conducted on a custom open-architecture 3D printing platform. Printed samples were made using 2% alginate with 0.75% CaSO₄. Hydrogel constructs were scanned via laser triangulation distance sensor. The point cloud images were analyzed to acquire computational measurements for key points of interest (e.g. height, width, and volume). Silastic molds were within $\pm 10\%$ error with respect to the native tissue for 7 key measurements, μ CT molds for 6 of 7, μ CT prints for 4 of 7, MRI molds for 5 of 7 and MRI prints for 4 of 7. This work shows the ability to generate and quantify anatomically shaped meniscal constructs of high geometric fidelity, and lends insight into the relative geometric fidelities of several TE techniques.

³ Ballyns JJ, Cohen D, Malone E, Maher SA, Potter HG, Wright TM, Lipson H, and Bonassar LJ. An Optical Method for Evaluation of Geometric Fidelity for Anatomically Shaped Tissue Engineered Constructs. *Tissue Eng Part C Methods* 2009; In Press.

4.2 Introduction

Reproducing geometry has been a goal of tissue engineering since its inception. Early studies began by forming cartilage in the shape of an ear [61] and creating bone cartilage composites in the shape of the mandible joint [62]. Later works have generated anatomically shaped menisci for the knee [29], cranial segments [84], and leaflet valves for the heart [73]. Ideally these anatomically shaped constructs would be tailored to meet patient-specific needs, but before patient-specific geometries can be achieved a method to evaluate the geometric fidelities of various tissue engineering techniques must be developed.

Geometry plays a crucial role in construct identity, function, and effectiveness. The importance of geometry spans across many tissue types. Facial reconstruction marks a corner stone of plastic surgery, interfacing cosmetic and reconstructive procedures to repair the contours of the nose, cheek bones, and mandible/chin, thus restoring physical and aesthetic identity [60]. In the heart, the shape and intricate folds of a leaflet for heart valves aid in regulating blood flow [108, 109]. Given the diversity of size and surface architecture in articular joints, geometry and size matching are critical for the success and longevity of surgical repair, whether it be for cadaveric allografts [143, 144] or more commonly used synthetic implants.

Generating complicated geometries for tissue engineering purposes has become possible by combing computer aided design (CAD) with a plethora of innovative fabrication methods such as injection molding, solid freeform fabrication (SFF) or 3D printing, and lithography. At the macro level, current efforts have concentrated on generating novel applications for injection molding and SFF technology using CAD programs to generate a variety of shapes to engineer tympanic membrane patches for the ear [74], bone structures [82-84], and heart valves [73, 145]. At the micro level intricate networks of micro channels can be generated through

lithography [80], and specific cell and matrix deposition can be achieved through inkjet printing techniques for use in hepatic tissue [89], and advance organ printing efforts [146].

As more techniques are developed to generate complex geometries, improved tools to quantify the accuracy of the end product's shape fidelity must be developed. Presently, geometry comparisons of tissue engineered constructs are made through simple visual inspection and manual measurements using rulers or calipers [27, 126]. Visual comparisons are not quantitative, and manual measurements suffer from lack of repeatability. Manual measurements are also time intensive and can result in damage to fragile implants such as hydrogels. Cohen et al. developed a method that compared engineered construct geometries using contact points throughout the hydrogel surface, whereby contact with the construct would complete an electrical circuit outputting an x-y-z location in 3D space [88]. Building upon work done by Cohen et al., a method could be developed that is automated, repeatable, and does not damage or contaminate the construct.

We propose such a method to compare anatomical constructs via a commercially available laser triangulation distance sensor and commercially available software designed to compare geometries. The methods are commonly used practices for non-tissue engineering applications such as quality control to verify surface roughness when rolling sheet metal [147] or to assess the source of vibrations in production equipment [148]. Here we focus on generation of anatomically accurate engineered menisci. The meniscus is pertinent for three reasons: (1) clinical relevance: meniscal lesions are one of the most common injuries in the knee [23] with >1.5 million knee surgeries involving the meniscus and usually resulting in removal of damaged tissue as opposed to repair or replacement [23]; (2) complex geometry: predicting and calculating meniscal shape based on MRI images can be quite time

consuming, and the algorithms for making these predictions are continually being modified [24, 106, 107, 149, 150]; (3) accurate meniscal geometry is crucial for proper mechanical function of the knee joint [5], its primary function being to aid in joint load distribution, thus decreasing contact stresses on the underlying articular cartilage. A deviation by >10% in size matching [24] can result in detrimental joint loading and more rapid development of osteoarthritis.

Having generated anatomically shaped menisci via injection molding [29] and 3D printing [88] in prior studies, our current objective was to quantify and compare shape fidelity between these two fabrication methods and to observe differences in constructs generated from MRI and μ CT imaging modalities.

4.3 Materials and Methods

Imaging

Four ovine menisci underwent both MRI and μ CT imaging as described previously [29]. Briefly, an MRI scan of each knee was performed on a clinical 3T MR unit (Twin Speed, GE Health Care, Milwaukee, WI) using a commercially available, 8-channel, receive-only knee coil (In vivo, Milwaukee, WI). Sagittal 3D spoiled gradient echo (SPGR) sequences were acquired resulting in a spatial resolution of 253.9 μ m (frequency) x 253.9 μ m (phase) x 0.5mm at one excitation.

The medial meniscus was then dissected, soaked in Omnipaque® Iohexol 300mg I/ml contrasting agent for 2 hrs, and scanned using an Enhanced Vision Systems Model Ms-8 In Vitro Micro-CT Scanner. Each scan was taken using short scan x-ray settings with 0.023mm/pixel resolution. Scans were calibrated via values for bone, air, and saline.

Mold Design

Injection molds were designed as previously described [29]. Briefly, MRI and μ CT data sets were used to render a 3D representation that allowed for formatting and generation of a solid model (Geomagic Studio 4.0; Research Triangle Park, NC). The model was then imported into CAD for mold design for both imaging modalities. Molds were printed using a Stratus FDM 3000 machine (Stratasys; Eden Prairie, MN).

Silastic impression molds were generated via room-temperature-vulcanizing (RTV) silicone rubber impression molds [69] (Silastic [®] brand; Dow Corning) of the same ovine menisci that underwent MRI and μ CT imaging.

Injection Molding

Alginate hydrogel was prepared by mixing 2% wt. low viscosity, high G-content alginate with 2% CaSO_4 [29]. Alginate hydrogel was then injected into the molds and allowed to gelate for 20 minutes in 2% CaCl_2 solution. Constructs were manually de-molded [29].

3D Printing

Alginate hydrogel was prepared by mixing 2% wt. low viscosity, high G-content alginate with 0.75% CaSO_4 . Alginate hydrogel was immediately loaded into a disposable plastic syringe and allowed to crosslink for 7 mins before being loaded into a custom, stepper motor-driven syringe pump. The pump was mounted onto a custom gantry robot which had 25 μm accuracy in the X-Y plane. Accuracy in the z-axis is equal to the tip diameter from which the hydrogel was extruded. Alginate hydrogel

was extruded layer-wise, through 0.5 mm diameter syringe tips (EFD Inc.; East Providence, RI) along paths planned by custom STL-slicing software.

To support overhangs, the construct was printed on top of a contoured substrate generated from the medical imagery (the substrate was fabricated prior to the start of the print using the Stratasys platform). After printing, the constructs were allowed to further cross-link in 2% CaCl₂ solution.

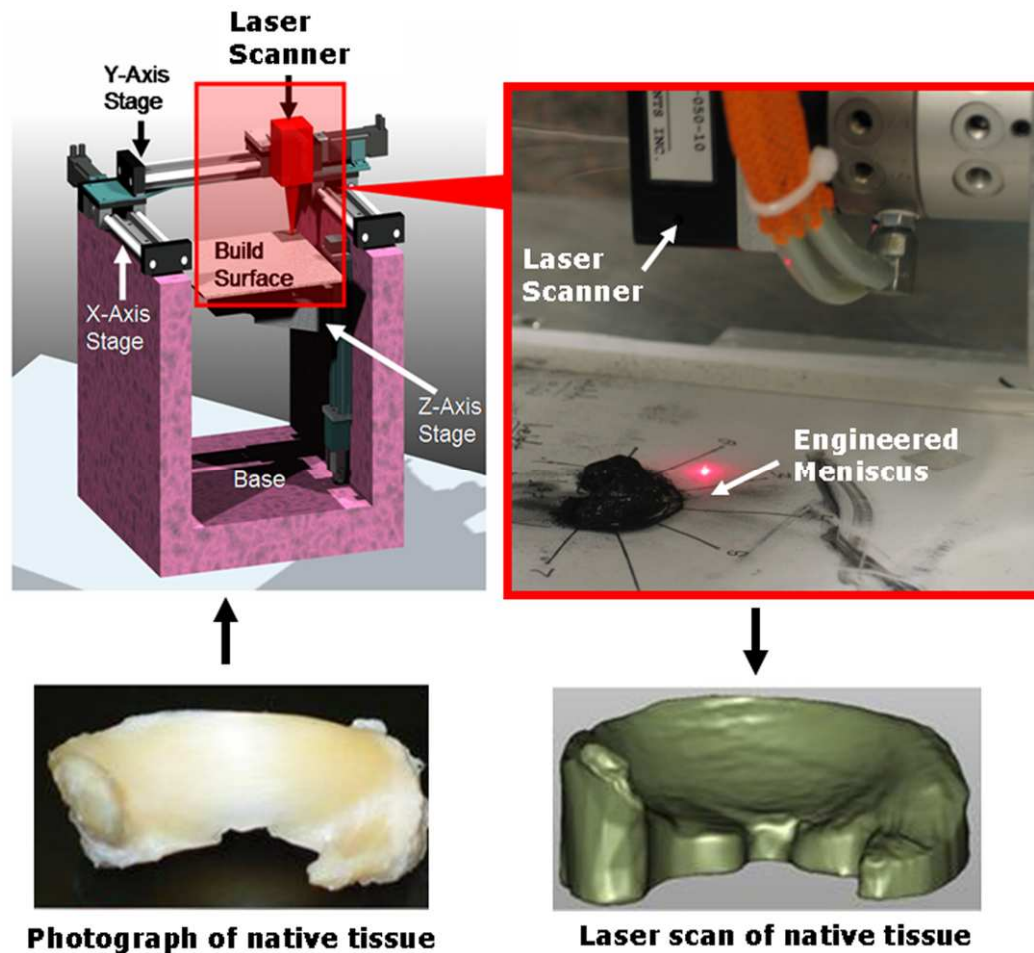


Figure 4.1: Custom gantry robot with laser triangulation distance sensor capturing surface of native and engineered sample. Note the projected surface of the native tissue overhangs on its respective laser scan (right).

Geometric Analysis

The native tissue was set on a transparency where an outline was made of the tissue then placed onto the gantry robot's Z-platform to be scanned via laser triangulation distance sensor (Microtrak II, MTI Instruments, Inc., Albany, NY). Alginate hydrogels were then placed on the transparency to fit the outline as best as possible then laser scanned. The distance sensor resolution was $50\mu\text{m} \times 50\mu\text{m} \times 1\mu\text{m}$ (x-y-z) and collected data at 40 KHz. Operations performed in Qualify v8.0 (Geomagic) included importing a point cloud of the scan data, reconstructing the surface, and running a shape auto-registration function to allow for proper alignment between the native and engineered laser scan for analysis of % error volume (Fig. 4.1). Key dimensions were measured, and % errors were calculated based on specific points established by Haut and coworkers [107, 150] (Fig. 2). Manual and computational measurements were taken and showed similar trends and values. Manual measurements were taken after the completion of the laser scan. Samples were aligned on a transparency to take all key dimensions (i.e. height, width, span, depth, etc.) using calipers. Manual and computational measurements showed similar trends and values to within 2-10%. Only computational data are presented here.

Errors associated with importing geometry would be caused by reconstruction of surfaces with radii of curvature less than the resolution of the scanner ($\sim 50\mu\text{m}$). As a result Qualify-based reconstruction did not represent surface roughness accurately. However, surfaces deviations were binned at $300\mu\text{m}$, which is 6 times larger than the resolution of the process. All key measurements (i.e. volume, height, width, span, depth, etc.) were automated to be taken from both native and engineered samples. Auto-registration was used to generate surface-to-surface deviation heat maps in Qualify to denote differences in overall surface geometry. Errors in auto-registration were determined by performing this task multiple times with varying starting

positions. The effect of starting position was minimal, compared to the 300 μm bins used to generate frequency histograms.

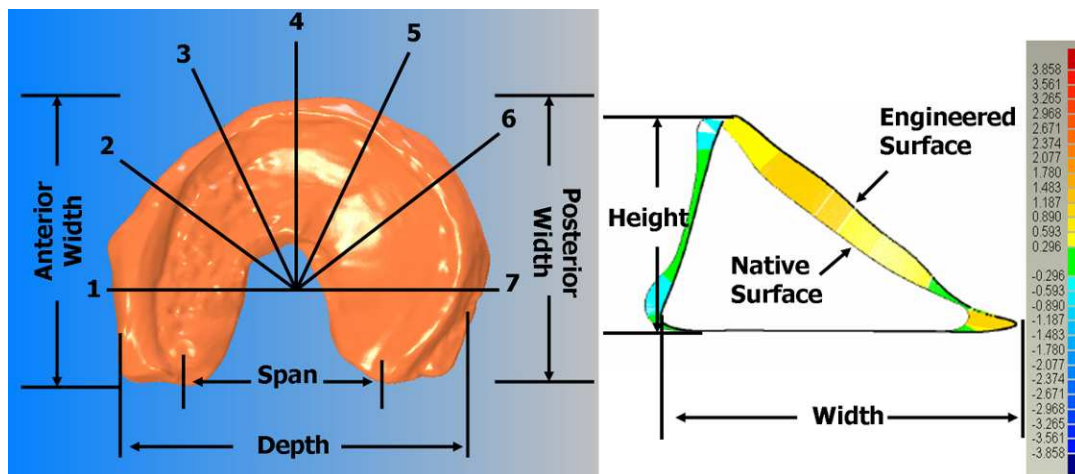


Figure 4.2: Key dimensions that were measured physically and computationally (left). Heights and widths were measured at the seven radial locations (1-7). Height was measured from the base of the meniscus to the top most point of the cross-section and the width was measured across the thickest portion of the cross section (right). Colored striations denote surface-to-surface deviations between native tissue and engineered hydrogel.

Statistics

A total of 6 replicates were made from each animal's medial meniscus ($n = 4$) for each fabrication method based on either MRI, μCT , or silastic impression mold, resulting in a total of 120 engineered samples. Both one-way and two-way ANOVAs were performed to determine significant differences with Tukey post hoc comparison using Sigmastat version 3.0. All data are presented as mean \pm SD with significance at $p < 0.05$.

4.4 Results

Quantification of Gross Anatomy

Visual inspection showed that both 3D printing and injection molding were capable of generating meniscal-shaped constructs of grossly comparable accuracy (Fig. 4.3). Similarly, initial observations of MRI and μ CT samples showed that both imaging modalities can be used to design menisci. Samples produced from silastic molds had superior surface quality compared to those produced from ABS plastic molds and 3D printed samples. Laser scans captured surface geometry well, but contained additional volume due to projection of overhanging surfaces (Fig. 4.1).

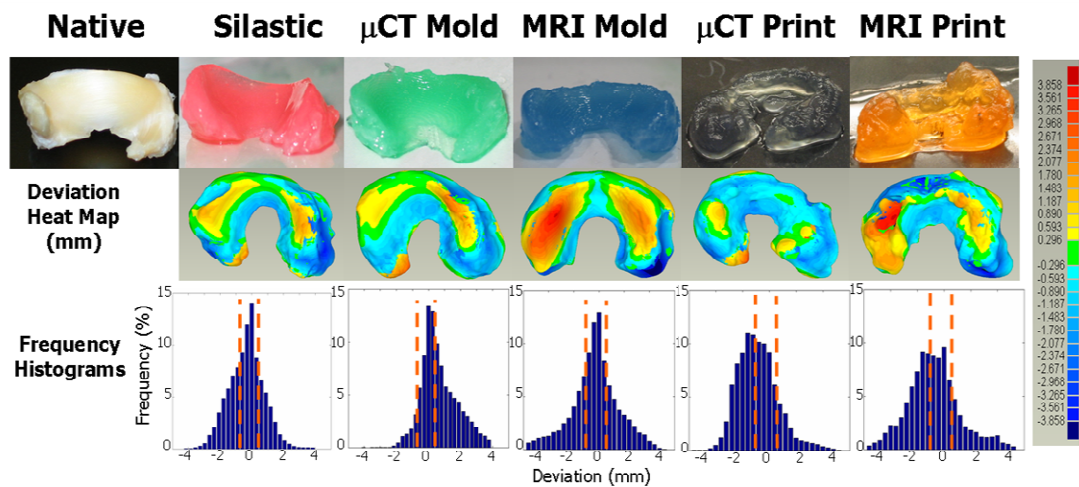


Figure 4.3: Photographs of engineered menisci (top row) and respective deviation color heat maps (middle row). Hot colors (reds) designate positive errors and cool colors (blues) designate negative errors relative to the native tissue surface. The bottom row contains %-error frequency histograms where bars located between the orange dashed lines are within $\pm 10\%$ error.

Computationally rendered images of the surface-to-surface deviation between native tissue and engineered constructs indicated errors ranging from -4mm to 3.8mm (Fig. 4.3). Heat maps of deviation show the most extreme errors in samples molded

and printed from MRI scans. Printed samples produced from μ CT scans had a prevalence of negative deviations, as indicated by cooler colors. Samples produced from silastic or μ CT-based molds had similar deviation maps, with slightly hotter patterns in μ CT-based samples (Fig. 4.3).

Frequency histograms of the deviation data indicate the fraction of points within $\pm 10\%$ of target height. Distributions of deviation were Gaussian for samples generated from silastic molds. Samples generated from MRI molds had minor skew from Gaussian, and all other had significant skews. All samples made from molds had deviation distributions centered at 0mm, while those of printed samples were centered at approximately -1mm (Fig. 4.3).

Pooled Measurements

Measurements of key dimensions (i.e. height, width, depth, span, posterior and anterior width) were pooled for all sheep to compare imaging and fabrication techniques (Fig. 4.4). All imaging and fabrication techniques produced desired dimensions for depth, span, anterior width and posterior width to within $\sim 10\%$ of target sizes. The 7 heights and widths were pooled (Fig. 4.2), since only a significant difference existed among groups. Molding was more accurate in achieving desired heights than the printing ($p < 0.05$) (Fig. 4.4). The μ CT molds were less accurate in replicating the desired width than MRI molds and both printed groups ($p < 0.01$) (Fig. 4.4). Overall, the samples made from silastic molds were within the $\pm 10\%$ range for 7 of 7 measurements, μ CT molds 6 of 7, μ CT print 4 of 7, MRI mold 5 of 7, and MRI print 4 of 7.

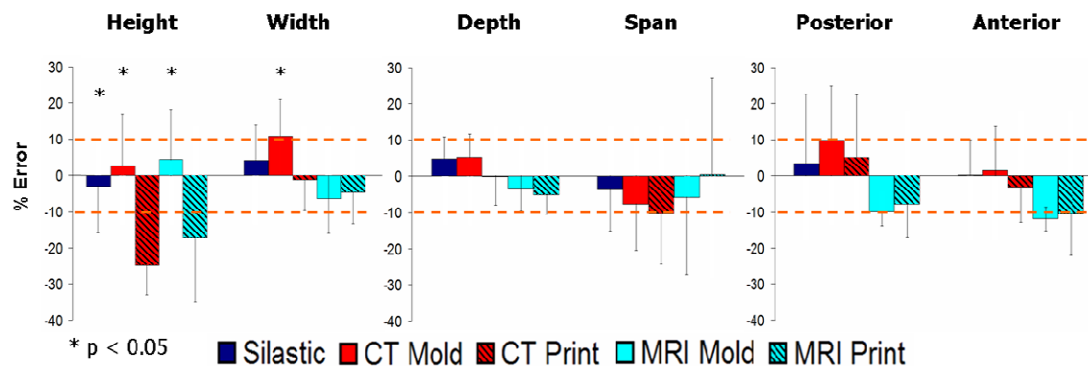


Figure 4.4: Average % error across key dimensions as a function of fabrication method. The height and width errors are pooled averages across the seven radial positions since no significant difference was present on location, but was dependent on fabrication method.

When data was pooled across all sheep (Table 4.1), no significant difference in volumetric error was found between fabrication groups ($p = 0.08$), despite a 3-4 fold difference between MRI molds and silastic molds. These trends in volumetric error (Table 4.1) are consistent with the heat map and frequency histogram data. As denoted by the orange dotted lines in the frequency histograms (Fig. 3), 43 - 50% of points fell within $\pm 10\%$ of intended heights (Table 4.1). There was no difference in the number of points that fell within $\pm 10\%$ between groups ($p = 0.931$).

Table 4.1: Average volumetric error, percentage of points from deviation heat maps that fell within $\pm 10\%$ of the native tissue, and repeatability error of fabrication methods. Lower repeatability error denotes higher repeatability of the technique.

	<i>Silastic</i>	<i>μCT mold</i>	<i>μCT print</i>	<i>MRI mold</i>	<i>MRI print</i>
Volumetric error (%)	-8.3 ± 19.5	-8.7 ± 31.4	-21.7 ± 19.0	-19.8 ± 7.7	-30.7 ± 9.4
$\pm 10\%$ (%)	49.1 ± 3.8	48.4 ± 10.7	45.9 ± 9.9	47.4 ± 13.8	43.5 ± 7.7
Repeatability error ($\pm\%$)	7.7	6.7	8.0	7.1	8.7

To compare reproducibility, the standard deviation of the error for all key measurements was averaged for each sample, sheep, and then for all sheep. The resulting value, denoted as repeatability error, indicates how consistently each technique can generate the desired geometry (i.e. a lower reproducibility error value means the technique is more consistent). For all techniques the repeatability error was <10% (Table 4.1), indicating that sample-to-sample construct generation was highly consistent.

Individual Sample Analysis

Despite low average errors, high variances were observed for some key dimensions (Fig. 4.4). The origin of this variance is unclear, but may be due to image source, fabrication process, or animal-to-animal variability. To elucidate the origin of this variation, scatter plots of percent error for height (Fig. 4.5), width (Fig. 4.6), and depth, span, posterior width, anterior width, and volume (Fig. 4.7) were constructed for all fabrication methods. Noticeable shifts in error and increases in variance of scatter profiles were observed for different fabrication processes. This was particularly noticeable for height measurements of MRI mold groups and both printed groups compared to the silastic mold and μ CT mold groups (Fig. 4.5). Across all 7 width measurements, there was little variation due to fabrication method (Fig. 4.6). The trend of increased variance and error for MRI and printed groups was also observed for other measurements, particularly depth and span (Fig. 4.7). The opposite trend was found for posterior width, anterior width, and volumetric error, for which there was a decrease in the scatter profile for both the MRI mold and MRI print groups (Fig. 4.7).

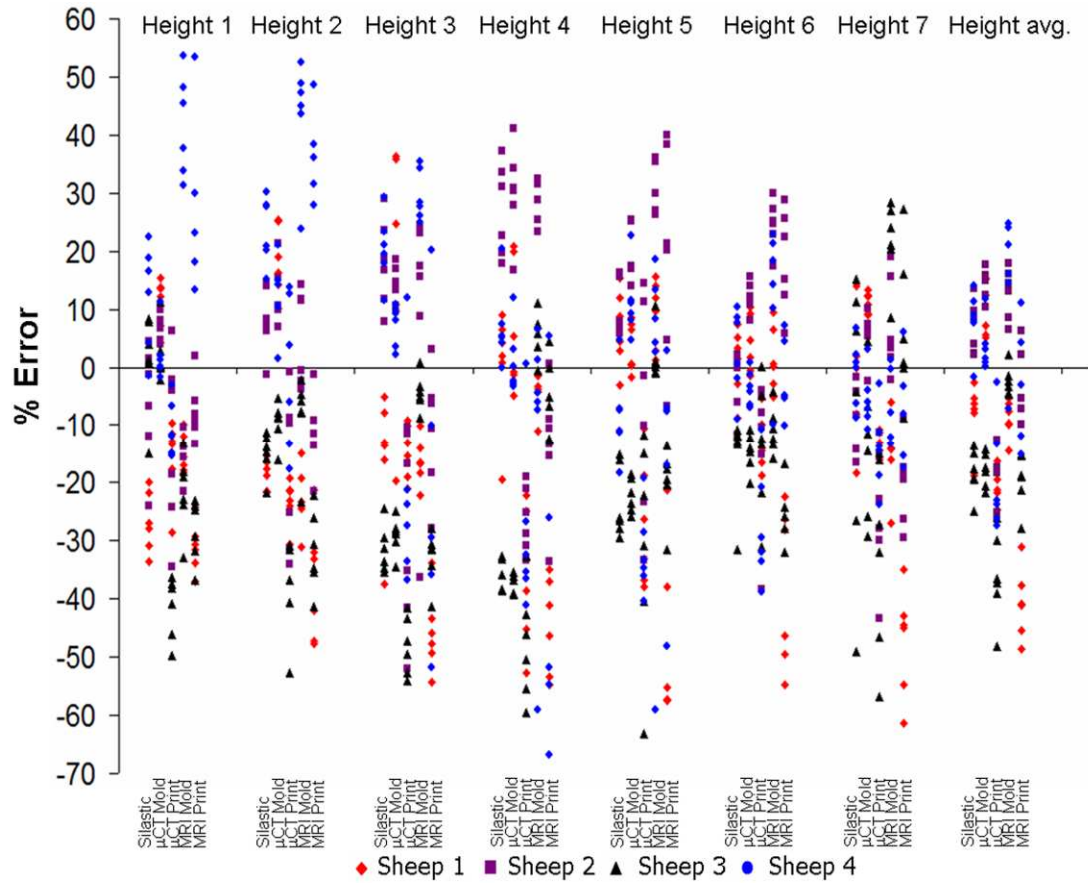


Figure 4.5: Scatter plot of height errors showing significant deviation mostly dependent on animal variation and fabrication technique but not location along the seven radial positions.

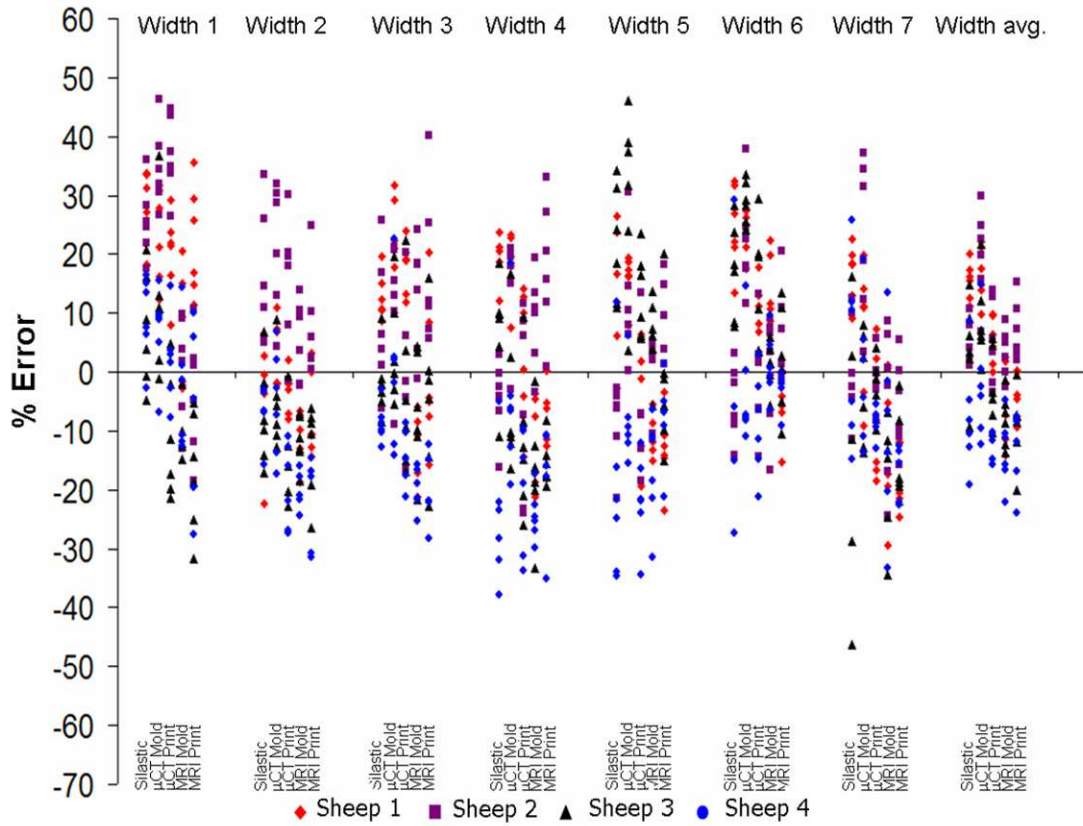


Figure 4.6: Scatter plot of width errors showing significant deviation mostly dependent on animal variation and fabrication technique but not location along the seven radial positions. Note width data scatter had less variance than height data in Figure 4.5.

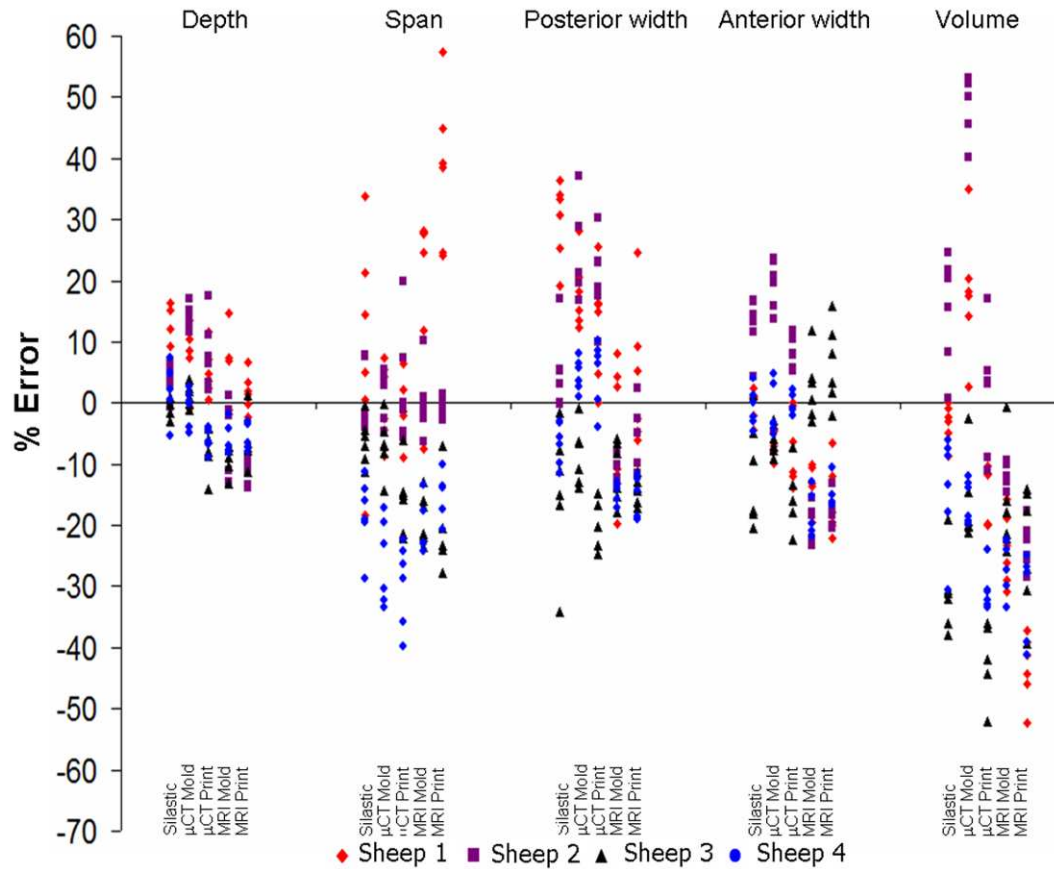


Figure 4.7: Scatter plot of depth, span, volume, and posterior and anterior width errors showing significant deviations dependent on animal, fabrication technique, and location, specifically span and volumetric errors.

The ability to accurately reproduce geometry varied significantly from animal-to-animal (Fig. 4.8) ($p < 0.01$). Sheep 1 and Sheep 3 had more accurate MRI molds than MRI prints ($p < 0.01$) while Sheep 2 and Sheep 4 had the opposite trend ($p < 0.01$). On the basis of average height measurements (Fig. 4.8) all μ CT molded groups were more accurate than μ CT printed groups ($p < 0.01$).

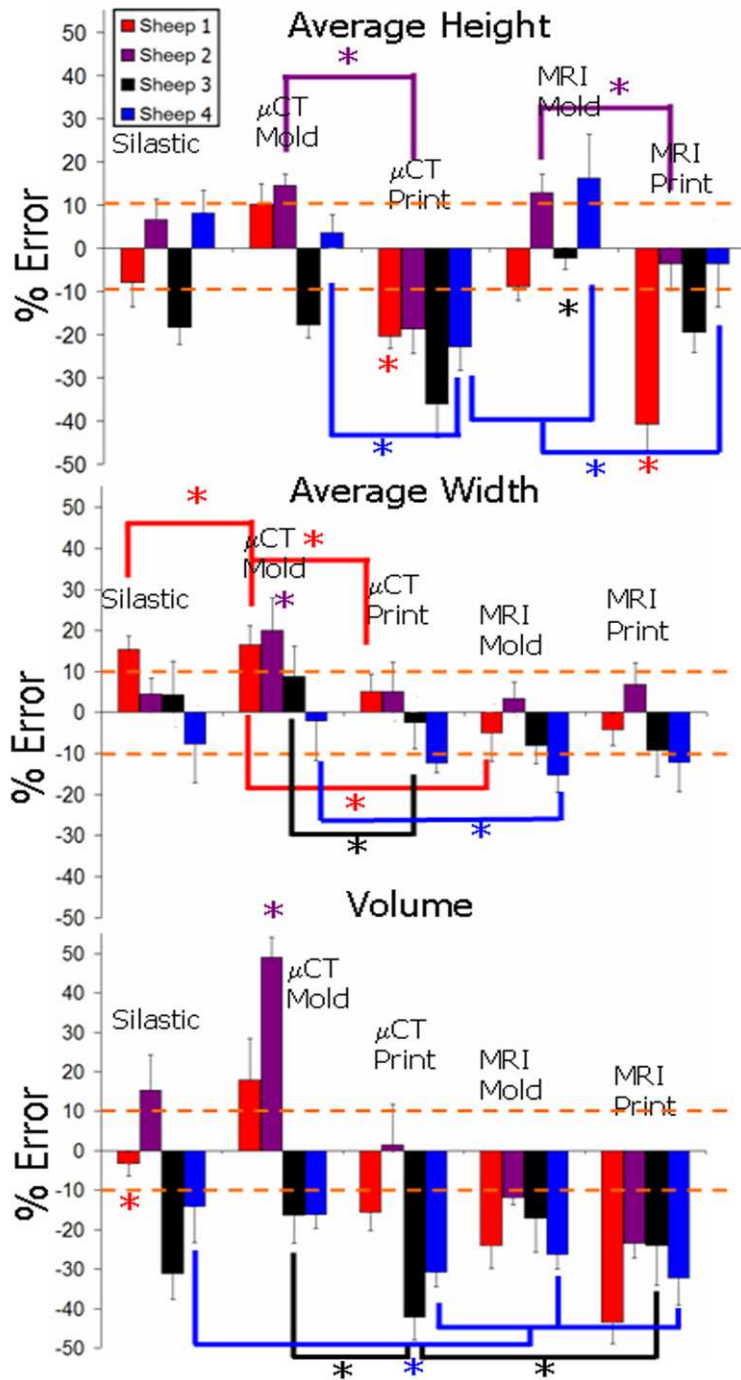


Figure 4.8: Average % error for height width and volume across different sheep and fabrication methods. Height and width data were pooled averages across the seven radial positions. Note differences between animals where sheep 3 was consistently negative for height, volume, and in most cases for width.

Average width data (Fig. 4.8) showed that printed samples generated the desired widths very well from both MRI and μ CT images. μ CT molds were more accurate than μ CT prints for Sheep 1, 2, and 3 ($p < 0.01$). MRI scans also provided accurate reproduction of width, as seen by the MRI mold group being more accurate than the μ CT mold groups for Sheep 1, 2 and 4 ($p < 0.05$).

Volumetric error (Fig. 4.8) was most dependent on imaging and fabrication method. MRI and printed groups were more consistently undersized for all sheep. μ CT and silastic mold groups were more likely to be accurately sized or oversized. Depth data was at or near $\pm 10\%$ for all fabrication methods for all sheep (Fig. 4.9).

Span data was more variable from animal-to-animal (Fig. 4.9). Sheep 3 and 4 were consistently undersized while Sheep 2 matched the target dimension very well. Silastic and μ CT methods were most accurate for Sheep 1, while MRI-based samples were over sized.

For posterior width MRI-based samples were consistently undersized for all sheep, but absolute errors were relatively low (Fig. 4.9). In contrast μ CT-based samples were variable, with some oversizing and undersizing that was sheep-specific. Trends in anterior width data (Fig. 4.9) were similar to posterior width trends. MRI-based samples were also undersized with slightly more absolute error.

Success Criteria

Matching key dimensions to within 10% is an established criterion for use of meniscal allografts [24]. We evaluated the fraction of data points that met this criterion for each sheep. The fraction of points that fell within $\pm 10\%$ error was greater than 33% for all sheep across all fabrication methods (Table 4.2). Silastic and μ CT molded samples were the most consistent with 40 – 64% of points meeting the $\pm 10\%$

error criterion. In comparison printed and MRI-based samples were more variable with 33 – 66% of points meeting the $\pm 10\%$ criterion.

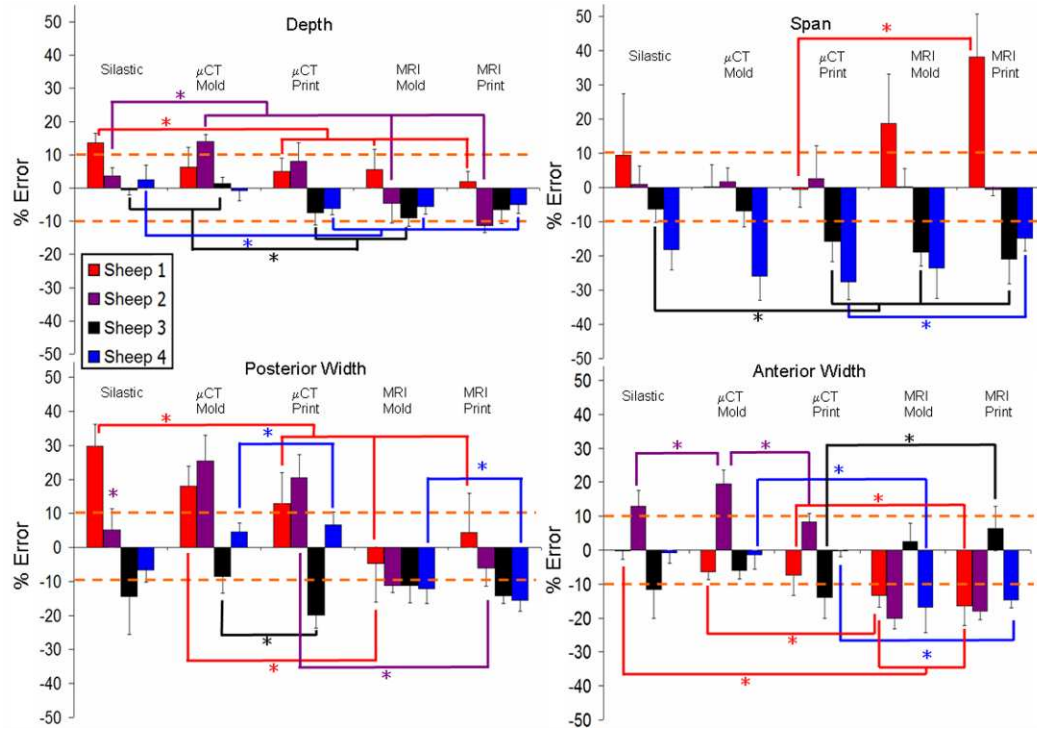


Figure 4.9: Average % error across different sheep and fabrication methods for depth, span, and posterior and anterior widths. As noted in Fig. 4.8, Sheep 3 and 4 are consistently more negative compared to the native tissue across the different points of interest regardless of fabrication technique or imaging modality.

Table 4.2: Percentage of points that fell within $\pm 10\%$ deviation from native tissue.

Note that with the exception of sheep 2 MRI mold and sheep 4 printing groups, most engineered samples were near 50% of the point being within the threshold.

	$\pm 10\%$ (%)				
	<i>Silastic</i>	<i>μCT mold</i>	<i>μCT print</i>	<i>MRI mold</i>	<i>MRI print</i>
Sheep 1	48.3 ± 5.8	45.9 ± 2.8	48.0 ± 2.3	66.3 ± 4.4	44.8 ± 3.5
Sheep 2	52.1 ± 3.1	40.7 ± 4.8	41.4 ± 5.4	33.5 ± 5.9	43.8 ± 4.6
Sheep 3	52.0 ± 2.0	64.1 ± 3.9	58.6 ± 4.6	47.2 ± 3.0	52.1 ± 3.0
Sheep 4	44.1 ± 4.2	42.8 ± 5.3	35.5 ± 3.3	42.5 ± 5.4	33.4 ± 3.3

Repeatability error (Table 4.3) for all methods for all sheep was quite low (5.9 – 11.0%). As might be expected from other data, repeatability was consistently lowest in all molded groups (5.9 – 8.7%). Printed samples were slightly less consistent with repeatability errors ranging from 5.9 – 11.0%.

Table 4.3: Repeatability error for each sheep meniscus and fabrication method. All samples except for sheep 4 MRI print had a repeatability error below 10%.

	<i>Repeatability error ($\pm\%$)</i>				
	<i>Silastic</i>	μ CT <i>mold</i>	μ CT <i>print</i>	<i>MRI</i> <i>mold</i>	<i>MRI</i> <i>print</i>
Sheep 1	7.1	6.9	6.7	7.0	8.5
Sheep 2	7.1	7.6	10.7	7.3	8.0
Sheep 3	8.7	6.5	8.9	5.9	7.5
Sheep 4	8.1	6.7	5.9	8.1	11.0

4.5 Discussion

This work is one of the first studies to present a method to quantitatively compare the geometry of tissue engineered constructs. The technique presented here uses a commercially available laser scanner and commercially available software that allows for automated measurements and quantitative geometric comparisons. This protocol was used to assess the geometry of the meniscus, a highly complex anatomic structure. This is a tissue where rudimentary techniques have been developed to quantify geometry as a standard for tissue transplantation [24, 107, 150, 151]. Using this new process enabled automated comparisons to these standards, and yielded a host of additional data about other tissue dimensions and sample volume. Although these

results are specific to regeneration of the meniscus, this approach is widely applicable to other tissues with complex geometry such as the ear, bones, and heart valve.

The technique described above was used to quantify the geometry of meniscal constructs designed from MRI and μ CT scans and fabricated via tissue injection molding and 3D tissue printing. The feasibility of using medical imaging data to design tissue engineered constructs has only been investigated very recently [29, 32]. Similarly, over the past decade a number of efforts have demonstrated the utility of injection molding [29, 69, 72, 74] and 3D tissue printing [88, 146] in fabricating engineered tissues with complex geometry. Despite all this work there is limited information on the geometric accuracy of these techniques and how this geometric accuracy might compare between techniques. The current paper directly compares the geometric fidelity of meniscal constructs produced by tissue injection molding and 3D printing designed from MRI and μ CT data.

Both imaging modalities and both fabrication techniques produced anatomically shaped constructs of high geometric fidelity. Injection molded samples were more accurate and reproducible than 3D printed samples. Constructs based on μ CT images were more accurate than MRI-based samples, likely due to difference in resolution based on the chosen scan parameters. It is true that this method may not be a fair comparison of the MRI scan's ability to provide an accurate model of the meniscus because it is in a loaded condition. However, MRI molds did yield samples with a significant fraction of key dimensions within $\pm 10\%$ error with respect to the native tissue. This suggests that the effect of loading may not be large for these measurements. Furthermore this study was interested in finding out whether a simulated *in vivo* MRI scan of the native meniscus could compete with a high resolution μ CT scan of excised tissue. We chose not to do an *in vivo* μ CT scan as μ CT does not readily visualize soft tissue without the use of a contrast agent. Delivery of a

contrast agent to a sheep meniscus *in vivo* would prove quite cumbersome such that it was not thought to be a medically relevant option for this method of image based tissue engineering. Instead we wished to implement a method that could be clinically relevant and non-invasive, as MRI obviates the need for ionizing radiation and avoids the potential of adverse contrast reactions.

Silastic impression molds were used as a benchmark since it is a widely used method for replicating complex geometries (e.g., dental records) and has been used to generate molded engineered tissue [29, 69, 78]. Comparing deviation heat maps and frequency histograms of injection molds using either MRI or μ CT showed that both were very close to silastic impression molds (Fig. 4.3). However, global trends across the seven points of interest [107, 150] showed that injection molds were close to or within $\pm 10\%$ range (Fig. 4.4). Furthermore, observations from pooled values across the seven height and width locations showed that each sheep had a distinct error pattern regardless of imaging or fabrication method (Fig. 4.8). While MRI based molds were more accurate at generating desired widths compared to μ CT based molds, all imaging and fabrication methods for all sheep were close to the acceptable error range with respect to width values. Current printing techniques still suffer in achieving the desired heights. These findings were supported by volumetric error data (Table 4.1 and Fig. 4.8), which were largest in printed tissues, most likely due to stochastic print errors. μ CT molds tended to be larger than native tissue, possibly due to swelling after the tissue was excised and soaked in contrast agent before imaging.

Silastic and μ CT fabricated constructs showed less deviation than MRI generated constructs. This finding was not surprising due to the much higher image resolution of μ CT. MRI samples were consistently undersized, possibly due to *in vivo* loading conditions that occur naturally when these joints are being imaged (Fig. 4.7). Another factor that could cause inaccurate amplification of deviation measurements is

projection-based 3D image reconstruction from the laser scans (Fig. 4.1). This is especially problematic with rigid native tissue that did not sit flat on the platform. Errors that can arise as a result of the projection-based 3D image reconstruction from laser scans will only affect height measurements near the horns, the volume estimate of the native tissue, and the deviation heat maps will be affected near the horns and white zone for some samples. These errors were consistent for all comparisons for a given sheep meniscus. This could be corrected with the addition of a second laser that would spiral around the menisci to gather radial data along the z-axis so that overhanging and elevated surfaces could be visualized and accounted for during the modeling process.

Further evidence of large differences between individual sheep menisci are also evident in the number of points that fell within $\pm 10\%$ (Table 4.2). For example, Sheep 1 had its highest score of 66.3% for MRI mold, while Sheep 2 had its lowest score of 33.5% for the same method. Sheep 3 had μ CT mold as its highest score of 64.1%, and Sheep 4 had no imaging modality or fabrication method that scored above 50% (Table 4.2).

The most promising result was that all fabrication methods and imaging modalities had repeatability errors below 10%, a necessary threshold to validate the practicality of this method for clinical purposes (Tables 4.1 and 4.3). The high repeatability is extended to all sheep as well, since all methods were below 10% with the exception of Sheep 2 μ CT print and Sheep 4 MRI print (Table 4.3). Having low repeatability error is more important than low linear error because simple linear errors can be addressed in the CAD portion of the fabrication process. Since the templates for these geometries are based on CAD software, geometries can be scaled accordingly to increase or decrease volume and thus compensate for shrinkage due to phase change (i.e., liquid

to gel). Altering the geometries in this way will allow deviation histograms to be centered about 0% error (Fig. 4.2).

A major challenge to image-based approaches to recreating patient-specific geometry is that the structure in need of replacement may not be intact or have the original or correct shape. In such cases there are at least three scenarios for image-guided tissue engineering: (1) the use of data on the geometry of the meniscus from the contralateral knee; (2) the use of data from the target knee obtained prior to an injury; (3) the development of a database of meniscal geometry from a large number of patients that could be used to find a match for a specific patient based on the anatomy of other structures in the knee. Obtaining meniscal data from the contralateral knee would require the assumption that both joints are symmetric. While this is not likely a perfect assumption, this approach would likely be more accurate than matches generated from available cadaveric donor tissue. This information might then be used to compare intact and deficient meniscal geometries in the setting of collagen meniscal scaffold replacement or more accurately sizing meniscal transplantation. Poor matching of native meniscal geometry has been implicated in failure of transplantation [152, 153]. If the patient has prior scans of the knee where the meniscus was undamaged (as might be the case for elite athletes or military personnel or individuals scanned for other reasons such as extensor tendon pathology), the relevant geometry could be extracted using the same technique we have presented here, even if MRI data were not as high a resolution as our scans. The last possibility is using current meniscal designs and scaling them to fit dimensions of the knee based on the tibial plateau, contralateral knee or other knee dimensions. The third option is using work already being explored by Haut and coworkers to develop proper parameters to match cadaveric donor tissue to patients in need of a total meniscal replacement.

With the method presented here, many steps can be taken to improve geometric fidelity in tissue engineered scaffolds. Future efforts should focus on development of higher resolution 3D printing of tissues implementing control feedback to prevent stochastic deposition print errors. Given its lack of ionizing radiation and no requirement for contrast agent (with the attendant risks of contrast reaction), MRI holds several advantages over CT for projected clinical use. Newer, more efficient 3D pulse sequences that provide sufficient boundary recognition and isotropic voxels will likely be more amenable to semiautomatic segmentation algorithms and more efficient generation of MRI-derived data sets [154]. The future of this methodology still lies in further development of both 3D printing and MRI technology to generate high resolution scans in a relevant clinical practice time frame and then print them with minimal deviation from the native tissue.

CHAPTER 5

EFFECT OF MEDIA MIXING ON ECM ASSEMBLY AND MECHANICAL PROPERTIES OF ANATOMICALLY SHAPED TISSUE ENGINEERED MENISCUS

Published in *Biomaterials*⁴

5.1 Abstract

This study investigated the hypothesis that controlled media mixing will enhance tissue formation and increase mechanical properties of anatomically-shaped tissue engineered menisci. Bovine meniscal fibrochondrocytes were seeded in 2% w/v alginate, cross-linked with 0.02 g/mL CaSO₄, and injected into molds of menisci. Engineered menisci were incubated for up to 6 weeks. A mixing media bioreactor was designed to ensure proper mixing of culture medium while protecting constructs from the spinning impeller. Impeller speeds were calibrated to produce Reynolds number (Re) of 0.5, 2.9, 5.8, 10.2, and 21.8. Constructs were divided and tested in confined compression and in tension to determine the equilibrium and tensile moduli, respectively. Media stimulation resulted in a 2 to 5 fold increase in mechanical properties and a 2 to 3 fold increase in matrix accumulation in constructs over 6 weeks in culture. Benefits from mixing stimulation for collagen accumulation and compressive modulus appeared to peak near Re 2.9, and decreased with increased mixing intensity. This study suggests that fluid mixing can be optimized to enhance mechanical properties of anatomically-shaped engineered constructs.

5.2 Introduction

Meniscal lesions are frequent injuries that lead to degeneration of knee articular cartilage [23]. Cadaveric meniscal allografts remain a preferred method of

⁴ Ballyns JJ, Wright TM, and Bonassar LJ. Effect of media mixing on assembly and mechanical properties of anatomically shaped tissue engineered meniscus. *Biomaterials* 2010; In Press.

treatment [149], but this approach suffers from the scarcity of donor tissue and the risk of disease transmission. Moreover, size matching is of high importance because geometry is crucial for proper functional performance [5, 24]. Collectively, these factors have spurred interest in meniscal tissue engineering (TE).

Current meniscal TE efforts have focused on the repair of focal defects through the use of stem cells [155, 156] and scaffold materials [157, 158]. There have also been efforts to characterize the behavior of meniscal fibrochondrocytes and how these cells generate extracellular matrix (ECM) in scaffolds with simple geometry, including agarose [31], alginate [159], chitosan-graft-poly(N-isopropylacrylamide) [160], poly(ϵ -caprolactone) [30], polyglycolic acid (PGA) [31], polyethylene terephthalate [37], and poly(L-lactic acid) [161]. Few studies have attempted to engineer whole menisci [27, 29, 142], due to the large size and the challenges associated with replicating the complex geometry.

Many biomaterials have been used to engineer small tissue samples, few can be formed into a prescribed geometry, especially an anatomical one such as the meniscus. Fewer still, can be combined with cells and formed into a desired shape while maintaining cell viability. Recently, the generation of anatomically-shaped engineered menisci based on MRI and μ CT images was made possible using alginate combined with tissue injection molding [29, 32]. These studies were encouraging, but the implants had heterogeneous matrix distribution and mechanical properties that were significantly worse than those of native tissue. Producing constructs that mimic the mechanical properties of native tissue still remains a challenge.

Controlled media mixing is widely used to stimulate TE constructs seeded with articular chondrocytes (AC) [33-36] and has been used with meniscal fibrochondrocytes [37, 38]. Several studies demonstrated that mixing bioreactors increase the amount of extracellular matrix (ECM) 3 to 9 fold and mechanical

properties 3 to 4 fold for TE cartilage [31, 34-37]. Media mixing stimulation is relatively simple to implement compared to direct compressive or tensile stimulation.

Based on the large size and unusual geometry of anatomically-shaped TE menisci, significant gradients in nutrient transport and ECM composition likely exist [29]. We hypothesized that media mixing will enhance transport of nutrients and ECM around and inside of TE constructs, improving the amount and homogeneity of ECM assembly. To test this hypothesis, we developed a bioreactor to control the extent of media mixing and determined how mixing affected the spatial pattern of ECM assembly and mechanical properties in anatomically shaped TE menisci.

5.3 Materials and Methods

Molded Constructs

Molds for generating anatomically-shaped TE menisci were made as previously described [29, 69]. Briefly, bovine meniscal fibrochondrocytes were isolated from freshly slaughtered 1 to 3 day old calves by 0.3% collagenase digestion. Cells were then seeded into sterile 2% w/v low viscosity high G-content alginate at 50×10^6 cells/mL. The alginate-cell suspension was combined with 0.02 g/mL CaSO_4 and injected into either silastic impression molds of bovine menisci or $\mu\text{CT/MRI}$ -based ABS plastic molds of ovine menisci. Molds were allowed to post-crosslink in 60 mM CaCl_2 for 20 minutes so that gels could be removed intact. Silastic impression molds of bovine menisci produced constructs with a volume of 4.5 to 5.0 mL (large volume constructs), while ovine molds volume ranged from 1.5 to 1.8 mL (small volume constructs).

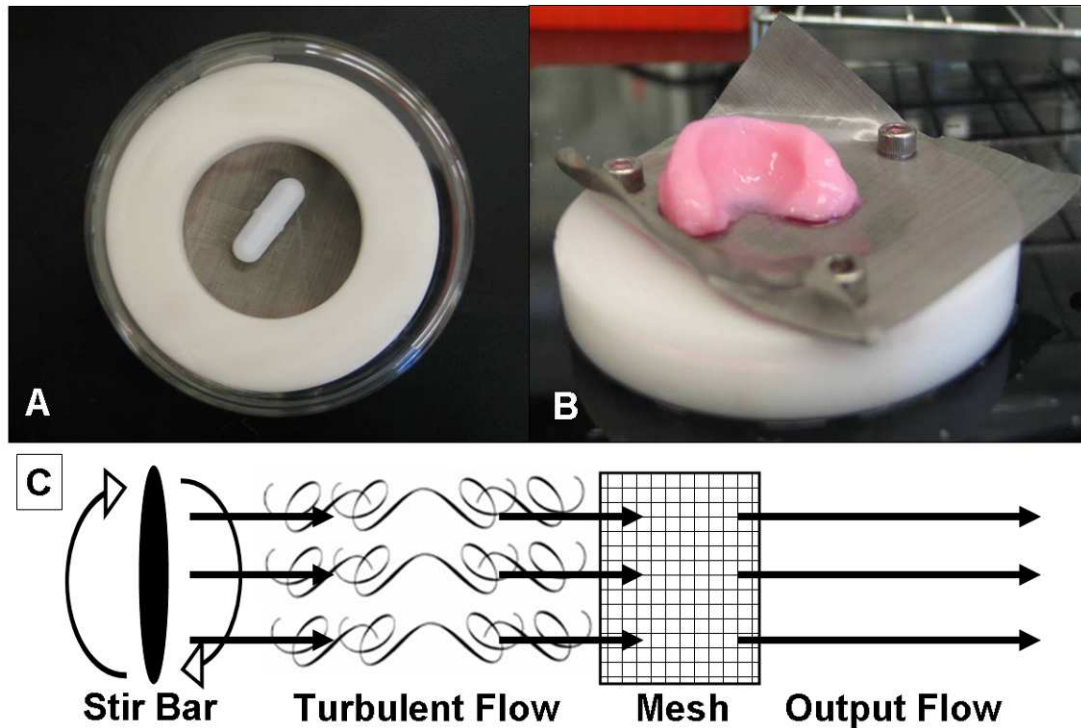


Figure 5.1: (A) Bottom view of mixing media bioreactor with magnetic impeller and a white delrin plastic ring. (B) Engineered menisci resting on stainless steel wire mesh that is attached to the delrin ring. (C) Grid flow model of turbulent flow generated by the magnetic impeller where eddies are attenuated by the fine wire mesh producing a more steady flow.

Culture Environment

A total of 25 small volume and 19 large volume constructs were cultured statically to compare spatial differences between the two groups. Larger volume constructs exhibited detectable spatial heterogeneity in both mechanical and biochemical properties, so these were chosen as the focus for mixing bioreactor studies. 51 molded constructs were cultured in a mixing media bioreactor consisting of

a plastic delrin ring with stainless steel wire mesh to support the meniscal construct over a magnetic stir bar (Fig. 5.1 A&B). Mixing intensity was quantified by the Reynolds number (Re); $Re < 10$ was assumed to produce laminar flow (i.e., relatively low mixing), and $Re > 10$ was assumed to produce turbulent flow (i.e., high mixing). Re was calculated using established models of flow through a grid [33, 162, 163]. In these models, fluid flow through the grid, in our case a wire mesh, attenuates eddy waves generated by the oscillations of the stir bar (Fig. 5.1C). Re was calculated as: $Re = \frac{\rho\omega L\ell}{\mu}$, where ρ was the fluid density (1 g/mL), ℓ was the mesh pore size (38 μm), μ was the fluid viscosity (0.001 Pa·s), ω was the angular velocity (varied from 1 to 15.7 rad/s) and L was the stir bar length (varied from 14 to 38 mm). Mixing intensity was altered by changing stir bar length and angular velocity (Table 5.1).

Table 5.1: For each mixing intensity represented by a Reynolds number, listed is the respective magnetic stir bar length, the number of rotations per minute (RPM), and the resulting type of flow in the mixing media bioreactor.

Re#	Stir bar length (cm)	RPM	Flow mode
0.5	1.4	10	Laminar
2.9	2.5	30	Laminar
5.8	3.8	40	Laminar
10.2	3.8	70	Turbulent
21.8	3.8	150	Turbulent

Samples were cultured at Re 0.5 (n = 9), Re 2.9 (n = 9), Re 5.8 (n = 12), Re 10.2 (n = 12), and Re 21.8 (n = 9). All constructs were incubated in DMEM with 10% FBS, 100 U/mL penicillin, 100 $\mu\text{g/mL}$ streptomycin, 0.1 mM non-essential amino acids, 50 $\mu\text{g/mL}$ ascorbate, and 0.4 mM L-proline medium for up to 6 weeks.

Sample Preparation

Upon removal from culture, the menisci were photographed then cut to expose and photograph the cross section. 2 sets of 6mm x 1mm plugs were cut from the face, center and bottom (Fig. 5.2) and used for mechanical analysis. Excess surrounding tissue from respective spatial locations was used for biochemistry; this tissue was weighed to obtain the wet weight (WW), frozen, lyophilized, then weighed again to obtain the dry weight (DW), and digested in papain for biochemical analysis [131].

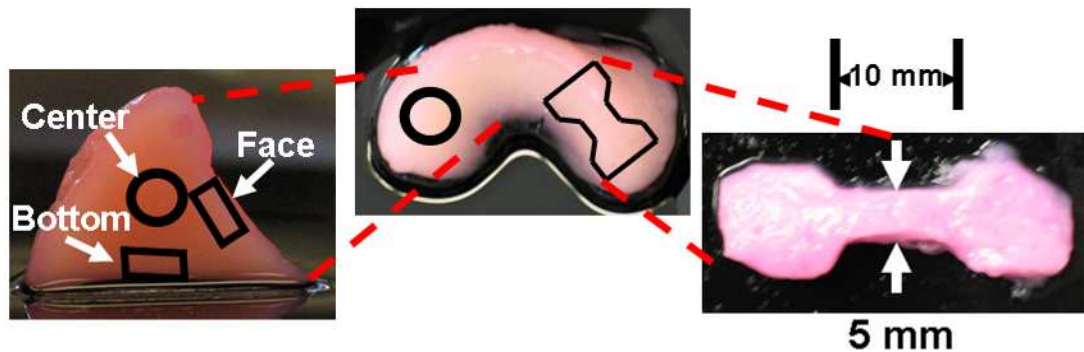


Figure 5.2: (Left) Spatial locations of biopsy plugs taken for confined compression and biochemical analysis. (Right) Sample dog bone of engineered tissue taken for tensile testing. The test area dimensions are 10 mm x 5mm x 2mm.

Mechanical Analysis

As described previously [69, 129] equilibrium modulus was determined under confined compression via stress relaxation tests by imposing 10 x 50 μm steps on the gel discs and fitting resultant loads to a poroelastic model [164] (EnduraTech; Electroforce (ELF) 3200 System, Minnetonka, MN).

Dog bones for tensile testing were cut from the same construct (Fig. 5.2). Samples were tested to failure at a strain rate of 0.75%/s, slow enough to assume

quasi-static loading and ensure failure at the central test region, not at the grips [165]. The tensile modulus was calculated as the slope of the linear elastic region of the stress-strain curve, using linear correlation analysis [165].

Biochemistry

A modified DMMB dye assay at pH 1.5 [132] was performed to determine GAG content in both TE constructs and culture media. The hydroxyproline assay was used to measure total collagen content [133]. DNA content was measured via Hoechst dye assay [131]. Data were not normalized to DNA content due to significant decreases in DNA content for constructs exposed to mixing media stimulation. Instead, all data were normalized to wet weight.

Histology

Cross-sections of molded constructs were fixed in 10% buffered formalin with 1mM CaCl₂ to prevent gel solubilization [134]. Fixed sections were then stained with Safranin-O to observe GAG formation and picrosirius red to observe collagen localization. The latter were viewed with polarized light to observe collagen fiber organization.

Statistics

Data were analyzed by 2-way ANOVA using Bonferroni t-test for post-hoc analysis. All statistical analyses were implemented with Sigmastat version 3.0, and all data are expressed as mean \pm SD.

5.4 Results

Construct Appearance and Composition

All groups of engineered constructs retained shape for the duration of culture (Fig. 5.3, column 1). Large volume static samples at 6 weeks exhibited a dense region of tissue formation at the center of the cross-sections (Fig. 5.3, columns 1&2). Visual inspection of cross-sections at 6 weeks showed an increase in tissue homogeneity with increased mixing intensity. As mixing intensity increased, the constructs contained a darker and more opaque center compared to static samples (Fig. 5.3, column 2). Safranin O staining at 6 weeks indicated a large increase in GAG accumulation for all groups (Fig. 5.3, column 3). Collagen accumulation at 6 weeks was not uniform across mixing intensities. Static samples and those at lower mixing intensities (Re of 0.5 and 2.9) showed accumulation of small fiber bundles, while the highest mixing intensity, Re 21.8, did not (Fig. 5.3, column 4).

Comparison between Large Volume and Small Volume Constructs

To compare the heterogeneity, we examined constructs spatially at the bottom, center, and face locations (Fig. 5.4, columns 2&3). We also compared overall construct performance by averaging the 3 locations (Fig. 5.4, column 1). Both small and large volume constructs were near the initial target seeding density of 0.4 μg DNA/mg WW (Fig. 5.4 row 1), but DNA content in small volume constructs was significantly lower than in large volume constructs for all three time points ($P < 0.01$). Neither large nor small volume constructs showed any significant differences between the bottom, center, or face locations for any time point, except for large constructs at 6 weeks. At 6 weeks, large constructs had significantly higher DNA content in the bottom compared to the center and face ($P < 0.05$).

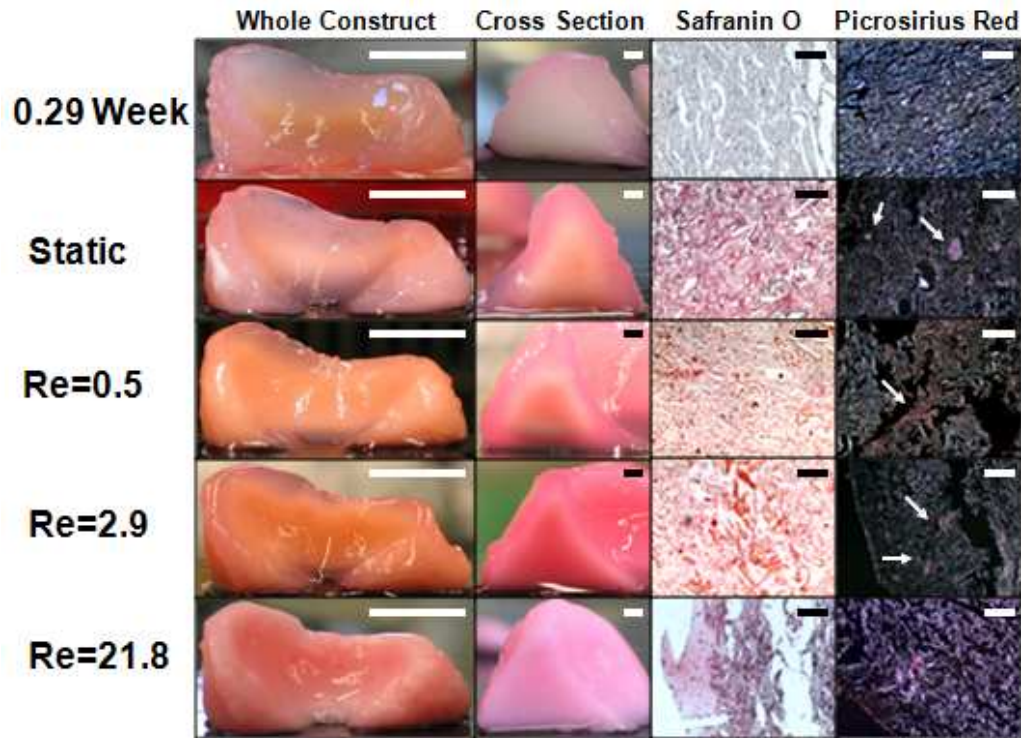


Figure 5.3: Photographs of (column 1) intact implants, (column 2) cross-sectional views, (column 3) tissue sections stained with Safranin-O at 200X original magnification and (column 4) tissue sections stained with picrosirius red at 200X original magnification for engineered cartilage at 0.29 weeks and 6 weeks for static and mixing intensities of Re 0.5, Re 2.9, Re 21.8. Scale bars represent (column 1) 10mm, (column 2) 2mm, and (column 3&4) 100 μ m. Arrows point to collagen fiber bundles.

No significant difference in collagen content was found between small and large constructs across all time points (Fig. 5.4, row 2). Large volume constructs had a significant increase in collagen content at 6 weeks ($P < 0.001$), while small constructs had significant increases in collagen at both 2 and 6 weeks ($P < 0.01$). No detectable difference in collagen content was found with location for either large or small volume constructs.

GAG content in both small and large constructs had increased at 2 and 6 weeks compared to 0 week controls ($P < 0.001$). Large volume constructs at 6 weeks had significantly higher GAG content than small constructs ($P < 0.05$) (Fig. 5.4, row 3). Large constructs showed spatial variation in GAG content at later times. Specifically, GAG content was higher on the bottom compared to other locations ($P < 0.01$).

Compressive equilibrium modulus (Fig. 5.4, row 4) increased for both small and large constructs at later time points ($P < 0.001$). Small constructs were stiffer in compression compared to large constructs at 2 and 6 weeks ($P < 0.01$). At later time points, large constructs showed spatial variation with a higher compressive modulus at the center compared to the bottom ($P < 0.05$).

Large constructs tended to have larger differences between locations compared to small constructs particularly for DNA and GAG contents. As a result, all mixing media comparisons were conducted using large volume constructs.

Effect of Mixing Intensity

Mixing decreased DNA at all intensities ($P < 0.001$) (Fig. 5.5). The decrease was a function of mixing intensity, with higher intensities causing more DNA loss ($P < 0.001$).

Despite the loss of DNA, at 6 weeks all mixing intensities increased GAG content ($P < 0.001$) (Fig. 5.5). Re 21.8 had a 2 to 3 fold increase in GAG content compared to all other groups ($P < 0.001$). Collagen content at 6 weeks followed a similar trend; all groups showed an increase with the exception of Re 21.8 ($P < 0.001$) (Fig. 5.5). The highest mixing intensity hindered collagen accumulation. Collagen content peaked at Re 5.8 for 6 weeks of culture, a 2 fold increase compared to static controls ($P < 0.05$).

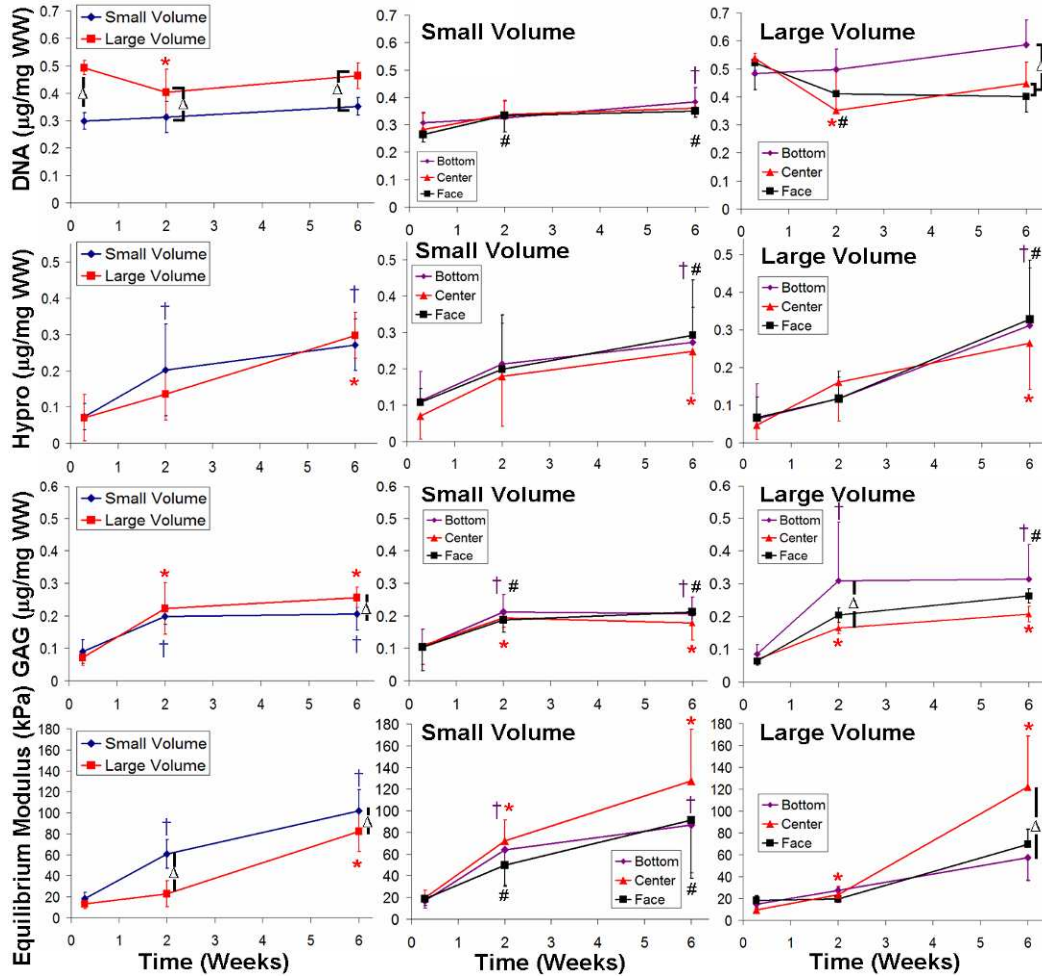


Figure 5.4: Plots of DNA content (row 1), collagen content (row 2), GAG content (row 3), and compressive modulus (row 4) comparing large and small volume constructs (column 1) and looking at the individual spatial properties for each volume size (column 2&3 respectively). For column 1 a “*” denotes significant differences with respect to 0.29 weeks culture time in large volume constructs, a “†” denotes difference in small volume constructs, and a “Δ” denotes differences between small and large volume constructs. For columns 2 and 3 a “†” denotes significant differences with respect to 0.29 weeks culture time in the bottom location, a “*” denotes differences in the center location, a “#” denotes differences in the face locations with time, and a “Δ” denotes differences between bottom, center, or face locations for a given time point. Data represented as mean \pm SD and $P < 0.05$.

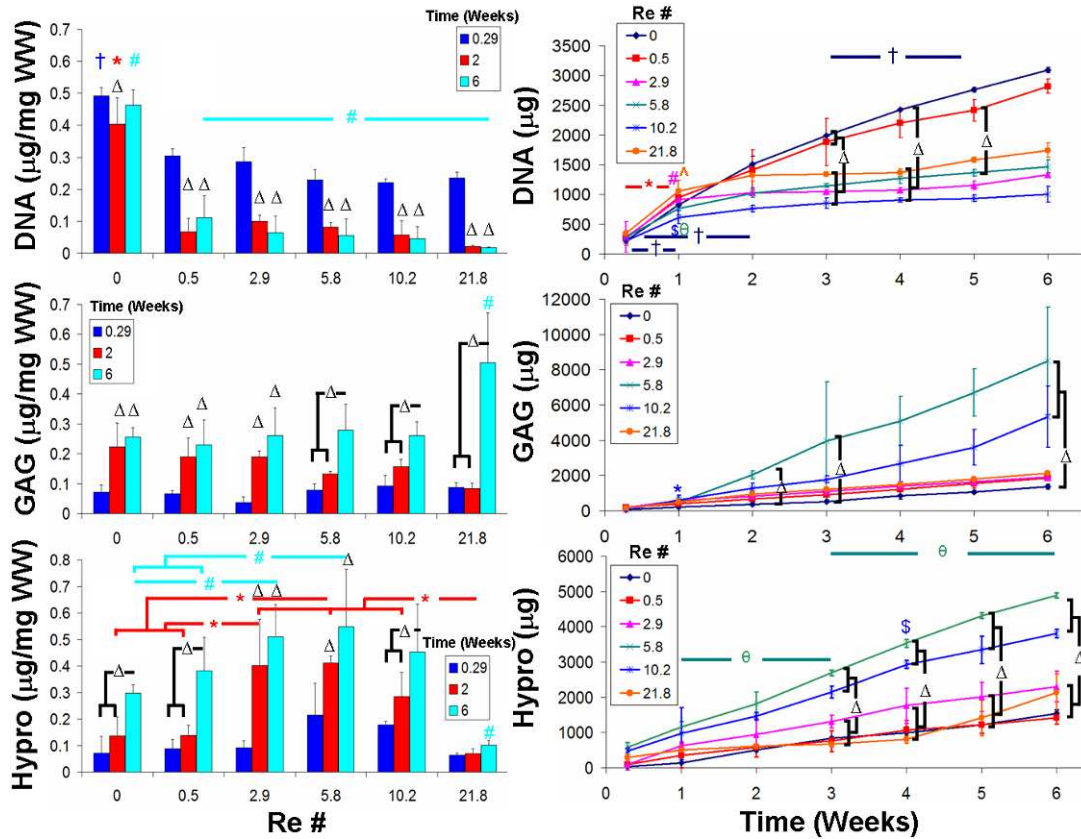


Figure 5.5: DNA content, GAG content, and collagen content found in engineered constructs (column 1) and cumulative release to the culture medium (column 2) for different mixing intensities. For column 1 a “ Δ ” denotes a significant difference with respect to 0.29 weeks cultures unless otherwise specified within a given mixing intensity, a “ \dagger ” denotes significant differences compared to all other 0.29 weeks values of different mixing intensities unless otherwise specified, a “ $*$ ” denotes a difference compares to all other 2 weeks values, and a “ $\#$ ” denotes a difference compared to all other 6 weeks values. In column 2 a “ Δ ” denotes a significant difference between media values for that given time point, and the remainder denote differences between respective time points for a given mixing intensity: “ \dagger ” = static, “ $*$ ” = Re 0.5, “ $\#$ ” = Re 2.9, “ θ ” = Re 5.8, “ $\$$ ” = 10.2, and “ \wedge ” = Re 21.8. For symbols not accompanied by bars signifies a significantly higher concentration than all other time points. Data presented as mean \pm SD and $P < 0.05$.

The media were analyzed biochemically because of the possibility that increasing mixing intensity could extract cells and ECM from engineered constructs to the media (Fig. 5.5). Cumulative DNA content accumulation in the media was greatest for static and at Re 0.5 while all other mixing intensity groups were similar. For all culture groups except Re 10.2, a large initial DNA release to the media occurred at 1 week ($P < 0.05$), followed by minimal DNA release. For the static and Re 0.5 culture group, DNA accumulation in the media continued to increase throughout culture.

GAG lost to the media was lowest for static cultures and greatest for Re 5.8 and Re 10.2 (Fig. 5.5). At week 1, significantly more GAG was lost to the media from Re 10.2 constructs compared to any other group ($P < 0.001$), while Re 5.8 constructs had significantly higher GAG accumulation in the media than static media samples at weeks 2 and 3 ($P < 0.01$). Collagen accumulation in the media followed a similar trend as GAG content, with static and Re 0.5 having the lowest amounts of collagen in the media (Fig. 5.5). Throughout all 6 weeks of culture Re 5.8 and Re 10.2 had significantly higher amounts of collagen found in the media than any other culture group ($P < 0.01$).

Mechanical Analysis

Compressive equilibrium modulus increased 2 to 5 fold during the course of 6 week culture (Fig. 5.6). This increase was most prominent (4 to 5 fold, $P < 0.05$) for $Re \leq 2.9$ and less pronounced for Re 5.8, 10.2, and 21.8.

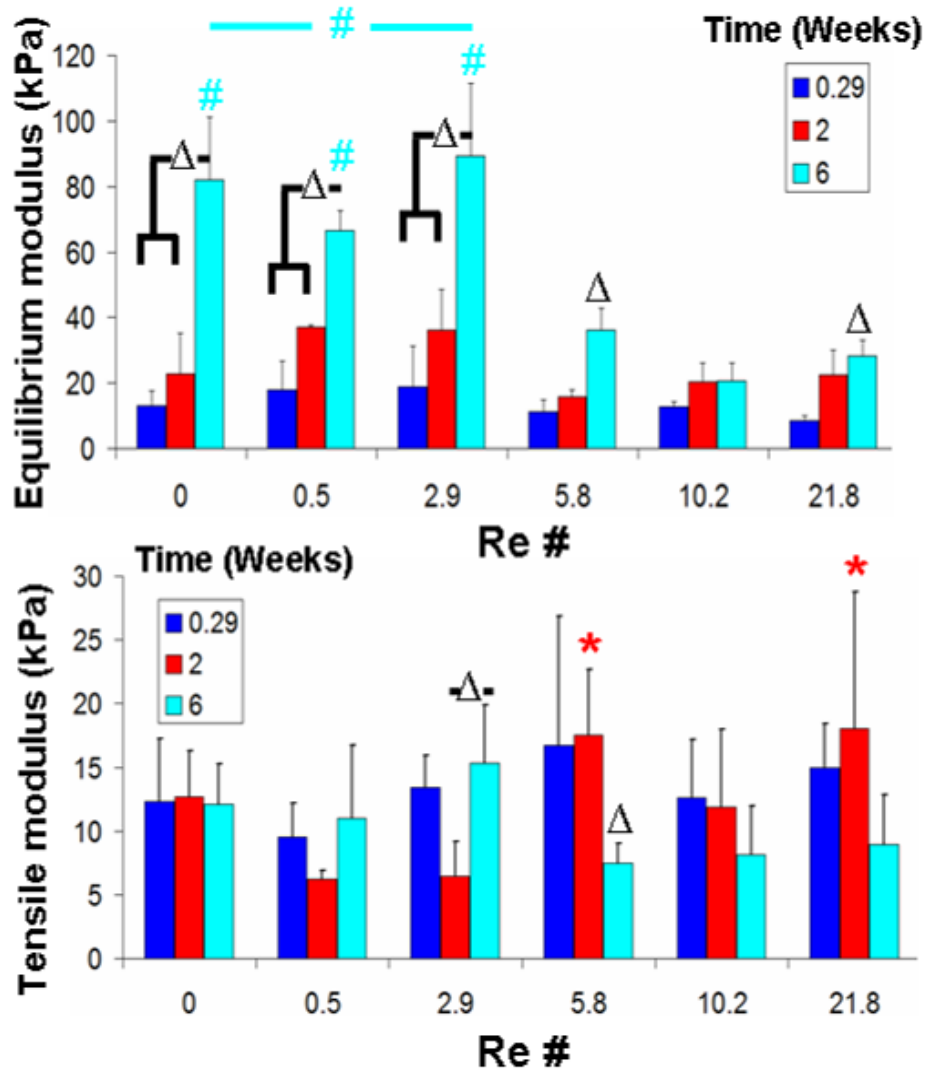


Figure 5.6: Compressive equilibrium modulus and tensile modulus for different mixing intensities across culture time. A “Δ” denotes significant difference compares to 0.29 weeks respective mixing intensity groups unless otherwise denoted. A, “*” denotes a difference between Re 0.5 and 2.9 within 2 week groups and “#” denotes a difference with the top 3 mixing intensities within 6 weeks values of different mixing intensities unless otherwise specified. Data presented as mean \pm SD and $P < 0.05$.

Higher mixing intensities (Re 5.8 and 21.8) had a 3 to 4 fold increase compared to lower intensities (Re 0.5 and 2.9) ($P < 0.05$) (Fig. 5.6) on tensile modulus. However, increases did not continue with culture time. Re 5.8 ($P < 0.05$) and above tended to have a consistent decrease in tensile modulus at 6 weeks compared to 0 and 2 week samples. Re 2.9 had a significant increase in tensile modulus at 6 weeks compared to 2 week constructs ($P < 0.05$).

Spatial Comparison between Mixing Intensities

Differences in spatial accumulation of matrix were observed between culture conditions (Fig. 5.7). With mixing GAG accumulation increased to a great degree with the highest intensity (Re 21.8) (Fig. 5.7, row 3 column 3). Most of the GAG was concentrated at the face of Re 21.8 constructs significantly more so than in the bottom and center locations ($P < 0.01$). While static samples had significantly more GAG located at the bottom compared to the center at 2 weeks ($P < 0.01$), other mixing intensities (with the exception of Re 21.8) became more homogeneous in GAG concentration throughout culture (data not shown for Re 5.8 and Re 10.2).

Similar trends were found for equilibrium compressive modulus (Fig. 5.7, row 4). Static samples at 6 weeks had a significantly higher modulus at the center ($P < 0.05$). Mixing intensities of Re 0.5, Re 2.9, and Re 5.8 all had significant increases in modulus by 6 weeks, but no significant difference was found with location across all culture times. Mixing intensities Re 10.2 and Re 21.8 did not increase compressive modulus globally or for any individual location, and as such was not significantly different among locations with time. Locations that did have significant increases in modulus at 6 weeks included Re 0.5 center, Re 2.9 center, and Re 5.8 bottom (all $P < 0.05$, data no shown).

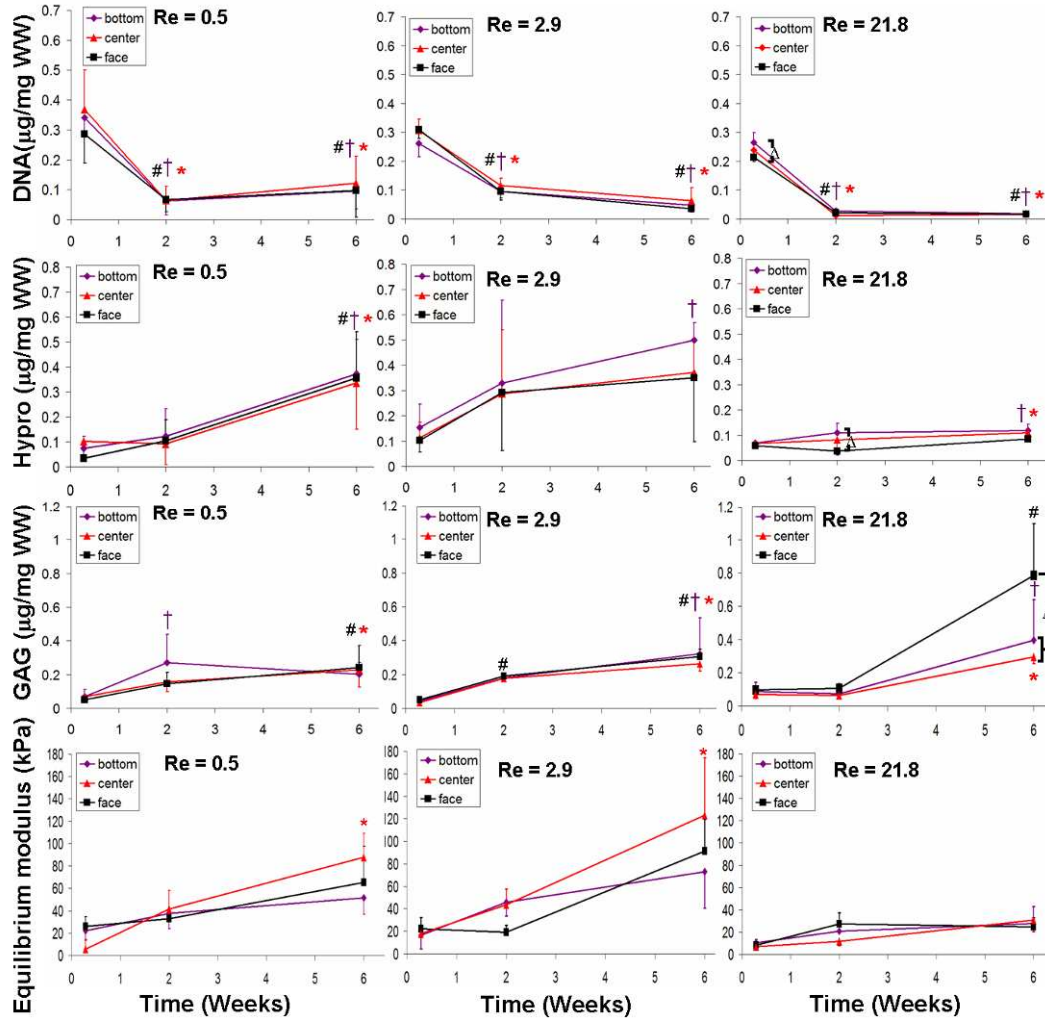


Figure 5.7: Spatial properties for DNA content (row 1), collagen content (row 2), GAG content (row 3) and compressive modulus (row 4) for Re 0.5 (column 1), Re 2.9 (column 2), and Re 21.8 (column 3). A “†” denotes significant difference compared to 0.29 weeks in the bottom location, a “*” denotes a difference compared to 0.29 weeks in the center location, a “#” denotes a difference compared to 0.29 weeks in the face locations, and a “Δ” denotes differences between bottom, center, or face locations for a given time point. Data represented as mean \pm SD and $P < 0.05$.

Collagen content in mixed media had high variance throughout the construct (Fig. 5.7, row 2). No spatial differences were detected for any mixing group except for Re 21.8, which had low collagen throughout. At 2 weeks, Re 21.8 constructs had significantly higher collagen content in the bottom than in the face ($P < 0.05$), but no location showed a significant increase with time. At 6 weeks statically cultured constructs had significant increases in collagen content with respect to 0.29 week cultures across all spatial locations ($P < 0.001$), as did Re 0.5 ($P < 0.05$). Re 2.9 only had a significant increase at 6 weeks at the bottom location ($P < 0.05$), Re 5.8 at both the bottom and face locations ($P < 0.05$), and Re 10.2 at the bottom and center locations ($P < 0.05$).

None of the mixing media groups showed any significant spatial differences in DNA content throughout culture (Fig. 5.7, row 1). However, as previously stated, static constructs had significantly higher DNA content in the bottom compared to the center and face at 6 weeks ($P < 0.05$). All mixing media locations showed uniform decreases in DNA content at 2 and 6 weeks compared to the 0.29 week time point ($P < 0.01$).

5.5 Discussion

We investigated the hypothesis that media mixing will enhance transport of nutrients and ECM around and inside of TE meniscal constructs, improving the amount and homogeneity of ECM assembly. We found that the process of ECM assembly in injection molded TE menisci was significantly altered by culture in a mixing bioreactor (Figs. 5.5-5.7). The primary effects were to redistribute ECM, forming a tissue that was more spatially homogeneous than static controls, with the exception of the highest mixing intensity (Fig. 5.7). However, mixing also enhanced the loss of ECM to the culture media compared to static controls (Fig. 5.5) and

detrimentally affected compressive modulus at higher intensities (Fig. 5.6). These results demonstrate the ability to modulate spatial heterogeneity of TE menisci and also show that mixing media stimulation was not uniformly beneficial across all mixing intensities.

Spatial properties were of interest because both ovine and bovine menisci have a unique shape and a larger volume than the types of constructs used in other studies. Prior TE meniscal and cartilage studies focused on small simple geometries ranging in volume from 0.06 to 1.8 mL [31, 34, 37], while we used anatomically shaped constructs ranging from 1.5 to 5.0 mL. The larger volume could result in different nutrient transport and ECM production behavior. Static cultures showed that large volume constructs had larger differences in their spatial profile compared to smaller constructs (Fig. 5.4). As a result large constructs were used to study the effect of mixing media stimulation. Trends found by averaging all locations showed that small and large constructs were similar across all biochemical and mechanical measures (Fig. 5.4, column 1), though compressive modulus was higher in smaller constructs, possibly related to the additional crosslinking step needed to remove constructs from molds. Post-crosslinking with CaCl_2 creates a more rigid skin at the surface of meniscal constructs that thickens with exposure time. While time was kept constant for both large and small constructs, the thickness of the skin with post-crosslinking represented a larger fraction of the cross-sectional area of small constructs and thus would explain higher compressive properties.

Temporal patterns in ECM accumulation were similar in large and small volume constructs (Fig. 5.4, columns 2&3). The only difference was that larger constructs tended to have larger spatial differences, as evidenced by the visual heterogeneity seen at the cross sections (Fig. 5.3, column 2). As observed previously [29] the TE menisci appear to grow ECM from the center out. Since larger constructs

have a larger volume to fill, the spatial heterogeneity in biochemical composition and mechanical properties is more evident. As a result, we used large volume constructs to better examine the effect of mixing media stimulation on these anatomical TE menisci.

We used mixing media stimulation because of positive results found in prior studies using this type of stimulation of articular cartilage [33-36]. The observed 2 to 3 fold increase in matrix accumulation and 1.2 to 4 fold increase in mechanical properties correspond to findings in the literature. The most surprising trend was the large loss of DNA content with media mixing (Figs. 5.5&5.7). Increasing mixing intensity increased the loss of DNA content in the constructs, but did not increase the amount found in the media (Fig. 5.5). In fact, increasing mixing intensity resulted in decreased DNA content in the media. The lower DNA content with higher mixing intensities could be due to cell destruction as a result of the spinning impeller (Fig. 5.1 A). The loss of DNA content in alginate constructs could be due to cells being washed out as a result of increased fluid flow from media mixing. This behavior was observed in studies with PEG gels in a rotating wall bioreactor [31]. GAG content did not change with mixing except for the large increase at the highest intensity (Re 21.8) (Fig. 5.5), but this large increase did not result in an expected increase in compressive modulus and the trend was towards decreasing tensile modulus for higher mixing intensities by week 6. GAG and collagen loss to the media was increased as a result of mixing intensity particularly for Re 5.8 and Re 10.2 constructs. The observed loss in collagen with no improvement in mechanical properties was also seen in engineered agarose gels from Aufderheid et al [31], in which GAG loss at later time points was attributed to the lack of collagen assembly in constructs.

The observed increase in ECM homogeneity with mixing (Fig. 5.7) is consistent to findings by Neves et al. who observed enhanced homogeneity in TE fibrocartilage [37]. However, collagen accumulation remained highly localized with a

specific region of the tissue (Fig. 5.3). The lack of organization could be due to the inability of collagen to bind to alginate and remain in the construct long enough to be organized into a cohesive matrix that would resemble native tissue. The redistribution of ECM away from the center observed at the highest mixing intensity agrees with bi-zonal findings by Marsano et al [34]. The increased fluid flow could have stimulated cells at the surface, increasing GAG production. However, GAG was more likely produced at the center and was pulled to the surface as a result of turbulence with mixing. Loss of GAG to the media as a result of fluid flow is further supported by the significant DNA loss in constructs and observed cell loss histologically, which occurred more at the surface.

Due to the high GAG content localized at the face, but no change in compressive modulus, we speculate that other mechanisms were responsible for the changes in mechanical properties in mixing media samples. The higher mixing intensity could have increased the rate of degradation of the alginate scaffold and removed the newly formed matrix. Our data are supported by an alginate degradation study that compared unseeded alginate meniscal gels under static, Re 5.8, and Re 21.8 mixing intensities in PBS supplemented with .2g/L of CaCl₂ to mimic calcium concentration in DMEM (See supplementary data). We found that over the course of 3 weeks increasing the mixing intensity resulted in a significant decrease in construct weight and more obvious alterations of meniscal shape. This is in great contrast to what was observed in cell seeded constructs, suggesting that there exists some cell matrix interaction that aided in maintaining geometry throughout 6 weeks of culture for all mixing intensities.

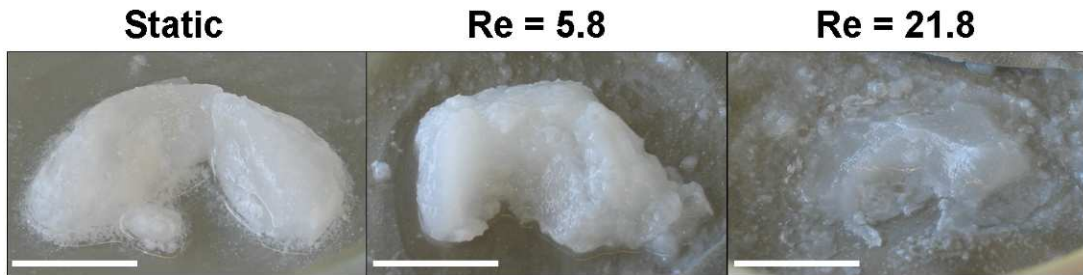


Figure 5.8: Photographs of a cellular alginate gels after 3 weeks of culture in static, Re 5.8 and Re 21.8 mixing intensities. Visually it can be seen that increasing mixing intensity has a large effect on overall shape on constructs. Scale bars represent 10mm.

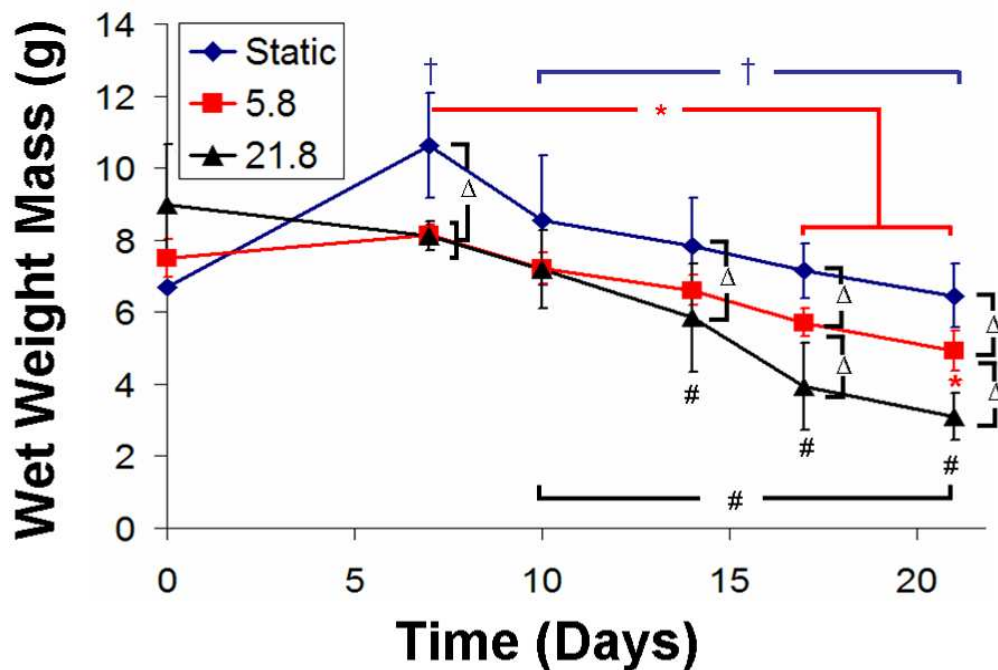


Figure 5.9: Plot of wet weight mass for acellular alginate hydrogels over 21 days of culture. A “+” denotes a significant difference for static samples compared to 0 day unless otherwise specified, a “*” denotes a difference for Re 5.8 compared to 0 day, a “#” denotes differences in Re 21.8 compared to 0 day, and a “Δ” denotes differences between static, Re 5.8, or Re 21.8 for a given time point. Data represented as mean \pm SD and $P < 0.05$.

5.5 Conclusion

This study began with the hypothesis that mixing media stimulation would enhance construct development. We found that mixing does affect ECM accumulation in large volume anatomically shaped TE menisci. The largest effect of mixing was the redistribution of ECM and the enhanced homogeneity in large volume constructs. However, mixing stimulation was not uniformly beneficial as indicated by DNA and ECM loss to the media and increased rate of scaffold degradation. But intermediate intensities appear to exist that can be optimally beneficial for construct growth.

5.6 Supplementary Data

To test the hypothesis that mixing intensity increased the rate of degradation of alginate hydrogels, we cultured acellular 2% w/v alginate hydrogels cross-linked with 0.02 g/mL CaSO₄. Constructs were cultured for up to 3 weeks in PBS supplemented with .2g/L of CaCl₂ to mimic the calcium concentration in DMEM. Upon removal from culture at 3 weeks, mixing intensity was found to have had a detrimental effect on overall shape fidelity (Fig. 5.8). Wet weights (WW) of constructs throughout culture showed (Fig. 5.9) that all samples tended to swell in the first week, especially static samples ($P < 0.001$). Significant decreases in WW also occurred with time for all 3 culture groups, with the largest being for the highest mixing intensity ($P < 0.05$). At the later time points, 17 and 21 days, significantly more WW mass was lost with each increase in mixing intensity ($P < 0.05$).

CHAPTER 6

DYNAMIC COMPRESSIVE LOADING OF IMAGE-GUIDED TISSUE ENGINEERED MENISCAL CONSTRUCTS

Submitted to the *Journal of Biomechanics* 5/14/2010⁵

6.1 Abstract

This study investigated the hypothesis that dynamic compression loading enhances tissue formation and increases mechanical properties of anatomically shaped tissue engineered menisci. Bovine meniscal fibrochondrocytes were seeded in 2% w/v alginate, crosslinked with CaSO₄, injected into μ CT based molds, and post crosslinked with CaCl₂. Samples were loaded via custom bioreactor with loading platens specifically designed to load anatomically shaped constructs in unconfined compression. Based on the results of finite element simulations, constructs were loaded under sinusoidal displacement to yield physiological strain levels. Constructs were loaded 3 times a week for 2 hours with 1 hour of intervening rest for up to 6 weeks. After 2 weeks of culture, loaded samples had 2 – 3.2 fold increases in extracellular matrix (ECM) content and 1.8 – 2.5 fold increases in compressive modulus. After 6 weeks of loading, glycosaminoglycan (GAG) content and compressive modulus both decreased compared to 2 week cultures by 2.3 – 2.7 fold and 1.5 – 1.7 fold respectively, whereas collagen content increased 1.8 – 2.2 fold. Prolonged loading of engineered constructs could have altered alginate scaffold degradation rate and/or initiated a catabolic cellular response, indicated by significantly decreased ECM retention at 6 weeks compared to 2 weeks. However, the data indicates that dynamic loading had a strikingly positive effect on ECM accumulation and mechanical properties in short term culture.

⁵ Ballyns JJ and Bonassar LJ. Dynamic compressive loading of image-guided tissue engineered meniscal constructs. *J Biomech*. Under review 2010.

6.2 Introduction

In the United States more than one million surgical procedures are performed each year to repair injury to the meniscus [3]. While there have been improvements in suturing techniques and medical devices to repair focal lesions [22], no options exist for whole meniscal replacement other than cadaveric allograft. To this end, tissue engineering techniques have been used in efforts to replicate the complex shape of the meniscus and generate constructs that can mimic biochemical and mechanical properties of native tissue [27, 29, 142, 166].

Meniscal tissue engineering approaches have primarily focused on repairing focal injuries or examining meniscal fibrochondrocyte behavior in various scaffolds including agarose [31], poly(ethylene glycol) (PEG) [167], poly(ϵ -caprolactone) (PCL) [30], and poly(L-lactic acid) (PLLA) [161]. Many of these cell seeded scaffolds lack the necessary biochemical and mechanical properties necessary to withstand implantation *in vivo*. As such, some type of mechanical conditioning might be necessary for engineered constructs before implantation into an animal model.

Several studies have established that dynamic compression enhances the production of extracellular matrix (ECM) and mechanical properties of meniscal explants and meniscal fibrochondrocyte-seeded seeded [41, 46, 161, 168] and articular chondrocyte-seeded discs [39, 43, 167, 169]. Typical loading regimes included compressive strains of 3-20% at frequencies of 0.3-1 Hz over the course of 0.5-14 days.

Very few studies have examined the effects of prolonged loading on engineered constructs [39, 43, 167], and no studies have attempted to dynamically load complex anatomically shaped engineered tissues in dynamic compression. Loading anatomically shaped engineered tissues presents several challenges. The first is designing a system that can apply loads to the complex shaped of the meniscus. The

second is estimating the stresses and strains that result from loading materials of complex shape with non-linear, non-elastic properties. As such, the goals of this study were to 1) design and fabricate a loading device for compressing anatomically shaped menisci; 2) develop and validate a finite element (FE) model to estimate levels of deformation necessary to produce physiologic levels of strain in anatomically shaped constructs; 3) determine the effect of physiological strains on ECM assembly and mechanical properties of tissue engineered (TE) menisci. We hypothesize that dynamic compression will enhance ECM and mechanical properties of anatomically shaped TE meniscal constructs.

6.3 Methods

Mold and Loading Platen Design and Fabrication

Micro computed tomography (μ CT) scans of ovine sheep served as a virtual negative for mold design as previously described [29, 142]. Briefly, the image was visualized as a surface (Microview, GE Healthcare), converted to a solid object (Geomagic Studio 4.0, Geomagic Inc., Research Triangle Park, NC) and imported into CAD software. In SolidWorks (Educational Edition, Concord, MA) loading platens were designed to match the complex surface of the meniscus (Fig. 6.1A&B). The CAD design process was similar to mold design using the meniscus as a virtual negative. The block was extruded to remove all but the concave surface of the meniscus then attached to the loading platen. A loading tray was similarly designed with an impression at the bottom surface to restrict motion of engineered menisci under loading (Fig. 6.1). Molds, loading platens, and loading trays were printed out of acrylonitrile butadiene styrene (ABS) plastic via fusion deposition modeling platform (FDM 3000 Stratasys; Eden Prairie, MN).

Molds for generating anatomically shaped TE menisci were made using previously described methods [29, 69]. Briefly, bovine meniscal fibrochondrocytes were isolated from freshly slaughtered 1-3 day old calves by 0.3% collagenase digestion. Cells were then seeded into sterile 2% w/v low viscosity high G-content alginate at 50×10^6 cells/mL. The alginate-cell suspension was combined with 0.02 g/mL CaSO_4 , and injected into mCT/MRI based ABS plastic molds of ovine menisci. Molds were allowed to post-crosslink in 60 mM CaCl_2 for 20 minutes so that gels could be removed intact.

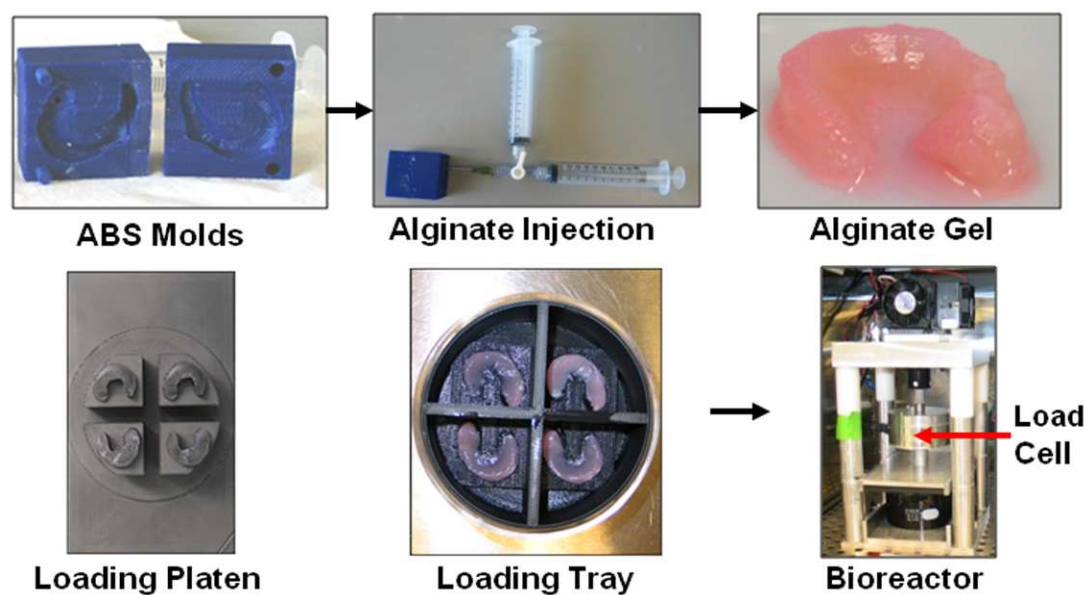


Figure 6.1: 3D printed ABS plastic parts generated via μCT data used for injection molding (top) and dynamic compression in custom bioreactor (bottom).

Dynamic Loading Conditions

Determining the appropriate loading regime for anatomically shaped hydrogel is challenging due to the complex geometry and material behavior. *In vivo*

measurements of meniscal displacements found that under full body weight maximal meniscal horns displacements range from 0.7-0.8 mm [21]. To estimate the stresses and strains resulting from displacements, we developed a linear poroelastic finite element (FE) model of meniscal alginate scaffolds undergoing unconfined compression using COMSOL MULTIPHYSICS software (COMSOL, Burlington, MA)(Fig. 6.2&6.3). This model was developed using previously described methods [44]. Briefly, the model was of the same 3D meniscus solid used to fabricate the injection molds and contained 6,419 tetrahedral elements that yielded a total of 141,504 degrees of freedom. The scaffold was assumed to be 98% porous, with Poisson's ratio of 0.167 and an average solid density of 1240 kg/m^3 [44]. The constructs was simulated to be fully hydrated with the fluid having an assumed viscosity of 0.001 Pa s and a density of 1000 kg/m^3 . Boundary conditions (Fig. 6.2) allowed displacement to occur freely on the concave loaded surface (Fig. 6.2A) and along the free faces (Fig. 6.2B), but was fixed along the Z-axis and free along X and Y-axis on the bottom supported surfaces (Fig. 6.2C). Loading was simulated using an impermeable frictionless loader with fluid movement allowed at the free surfaces (Fig. 6.2B).

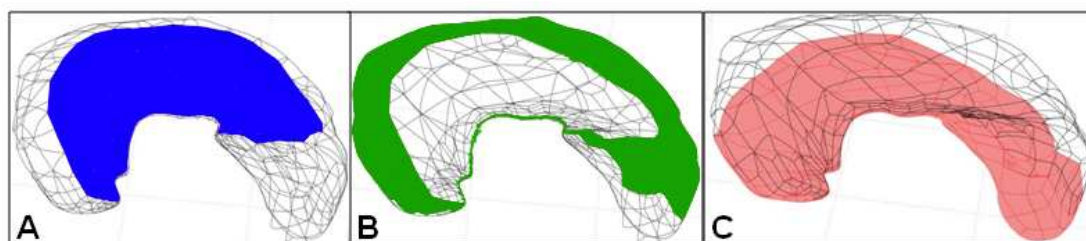


Figure 6.2: Boundary conditions for linear poroelastic FE model. (A) loaded surface exposed to sinusoidal wave form (blue), (B) free surfaces from which fluid can leave and enter the sample (green), and (C) supported bottom surface fixed along the Z-axis (pink).

Fluid/solid interactions in loaded alginate constructs were modeled via time dependent coupled pore pressure/effective stress analysis using the structural mechanics and chemical engineering modules of COMSOL MULTIPHYSICS as previously described [44]. Based on the FE analysis we created a low loading regime (171 μm group) and a high loading regime (352 μm group) with maximum imposed displacements of 342 μm and 704 μm respectively. The FE model (Fig. 6.3) predicted compressive strains of 7% and 15% for 171 μm and 352 μm groups respectively for the majority of the concave surface on the meniscus. The compressive strains calculated by our FE model were within the range of strain values used in other dynamic compression studies [39-41, 46, 170].

Anatomically shaped constructs were exposed to three different loading conditions, static free swell culture (n = 24), 171 μm group (n = 12), and 352 μm group (n = 20). Engineered menisci were loaded via custom bioreactor (Fig. 6.1) three times a week for 2 hrs at 1 Hz with an hour or rest in between loading cycles. The 171 μm group was compressively loaded under sinusoidal displacement control with a 171 μm offset and a 171 μm amplitude, while the 352 μm group had a 352 μm offset and 352 μm amplitude. The bioreactor was also fitted with an iLoad TR Digital 10 lb. Load Cell (Loadstar Sensors, Fremont, CA) to measure loads throughout culture. All constructs were incubated in DMEM with 10% FBS, 100 U/mL penicillin, 100 mg/mL streptomycin, 0.1 mM non-essential amino acids, 50 mg/mL ascorbate, and 0.4 mM L-proline medium for up to 6 weeks. Culture medium was changed three times a week and saved for biochemical analysis.

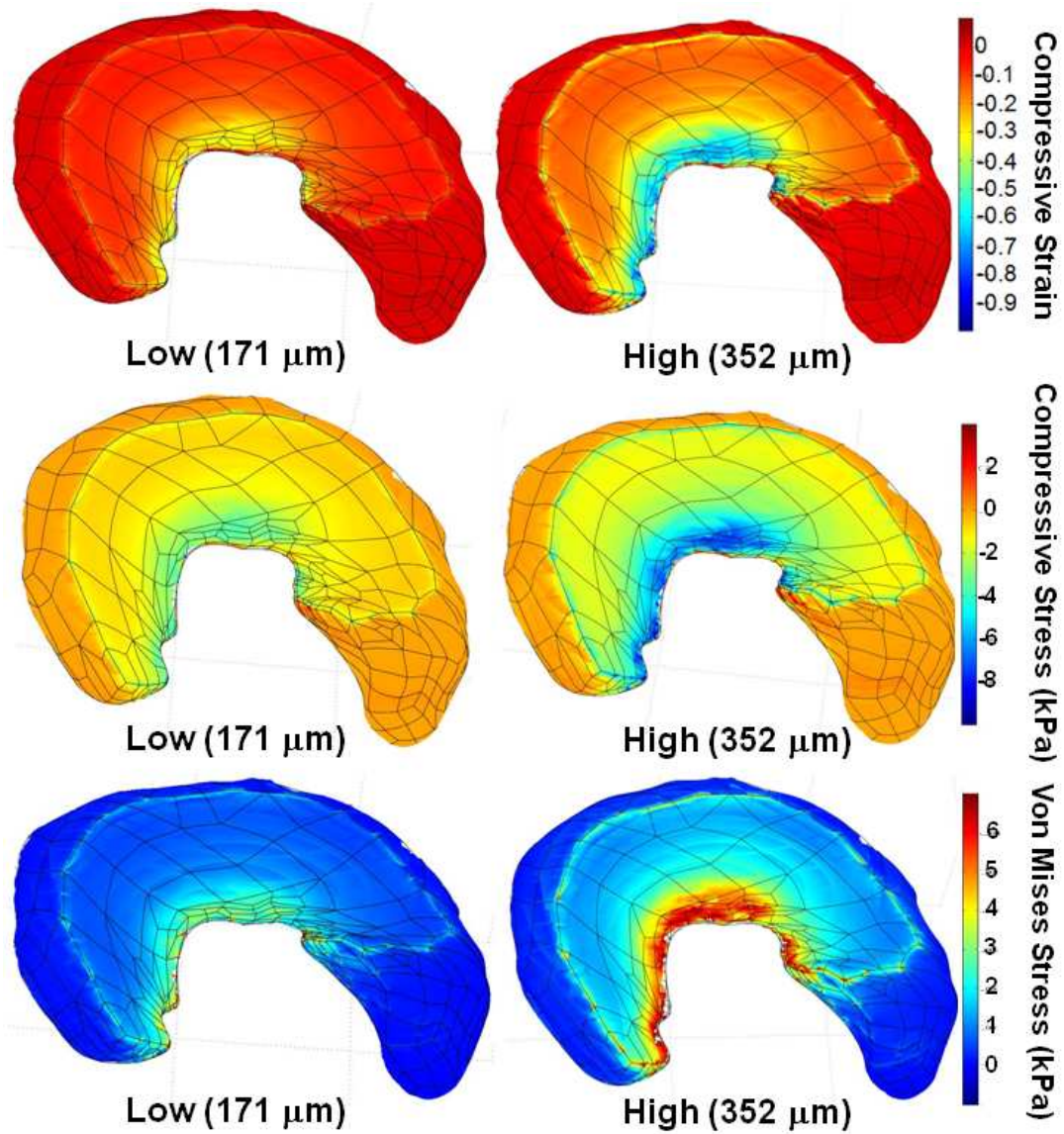


Figure 6.3: Predicted compressive strains (top), stresses (middle), and Von Mises stresses (bottom) for high (352 μm) and low (171 μm) imposed displacement groups.

Post Culture Sample Analysis

To determine the extent to which dynamic compression affected the shape of TE menisci, upon removal from culture engineered menisci were photographed, weighed and scanned via laser triangulation distance sensor (OADM12 Laser, Baumer

Ltd., Southington, CT) using the Fab@Home printing platform. 3D scans were taken at a resolution of 100 x 100 x 78 μm (x – y – z). Scanned data was used for geometric shape comparison in Qualify v8.0 (Geomagic, Research Triangle Park, NC) as described previously [142].

Engineered menisci were then processed for histology, biochemistry, and mechanical analysis as described previously [29]. Briefly, cross-sections were cut and fixed in 10% buffered formalin with 1mM CaCl_2 to prevent gel solubilization [134]. Fixed sections were then stained with Safranin-O to observe glycosaminoglycan (GAG) formation and picosirius red to observe collagen localization. Picosirius red stained samples were exposed to polarized light to observe collagen fiber organization.

For each sample, 6mm diameter and 1mm thick plugs were cut from the face, center, and bottom of sample surfaces. Plugs were used for mechanical analysis and excess surrounding tissue from respective spatial locations was used for biochemistry. Excess tissue was weighed to obtain the wet weight (WW), frozen, lyophilized, weighed again to obtain the dry weight (DW), and digested in papain [131]. As described previously [69, 129] equilibrium modulus was determined via stress relaxation tests by imposing 10 x 50 μm steps on the gels and fitting resultant loads to a poroelastic model (EnduraTech; Electroforce (ELF) 3200 System, Minnetonka, MN). A modified DMMB dye assay at pH 1.5 [132] was performed to determine GAG content in both TE constructs and culture medium. The hydroxyproline assay was used to measure total collagen content [133]. DNA content was measured via Hoechst dye assay [131].

Statistics

Data were analyzed by 2-way ANOVA using Tukey t-test for post-hoc analysis. All statistical analyses were implemented with Sigmastat version 3.0, and all data are expressed as mean \pm SD.

6.4 Results

FE Model

Predicted compressive stresses were highest at thin regions of the meniscus for both 171 μ m and 352 μ m groups with peak stresses of -3 kPa and -8 kPa respectively (Fig. 6.3 row 2). Integrating over the loaded surface (Fig. 6.2A) at maximum displacement yielded a max load of 1.09 N (0.74 kPa) and 1.25 N (1.52 kPa) for 171 μ m and 352 μ m loading conditions respectively. The applied loading protocol did result in relatively large tensile stresses in the thin regions of the meniscus based on von Mises stress calculation with values of 2.5 kPa and 6 kPa occurring at maximum displacement for 171 μ m and 352 μ m loading groups (Fig. 6.3 row 3).

Construct Shape Fidelity and Composition

All groups of engineered constructs retained shape for the duration of culture (Fig. 6.4 column 1). Heat maps of deviation show that static samples had little to no change in surface fidelity while loaded constructs had increasing surface deviation with culture time. The fraction of points that were within \pm 10% of the target height was constant throughout culture for all culture groups (35% – 40%) except the 171 μ m group which had a decrease at 2 and 6 weeks (31.5% and 28.2% respectively, $P < 0.01$)(Table 6.1). At weeks 2 and 6 both loading groups had fewer points that fell

within $\pm 10\%$ error that statically cultured samples ($P < 0.05$). However, despite the decrease in points that were within $\pm 10\%$ of target height, all culture groups maintained the target volume of 1.5 mL and maintained construct mass through out 6 weeks of culture with the exception of 171 μm 6 week constructs (Table 6.1).

All constructs increased in opacity throughout culture, particularly at the horns of loaded constructs at 6 weeks (Fig. 6.4 column 1). Safranin O staining showed a large accumulation of GAG occurring as early as 2 weeks in both loading groups that was not observed in static samples until week 6 (Fig. 6.4 column 3). However, after 6 weeks of culture there was a decrease in GAG localization from 2 weeks in both loading groups. Collagen accumulation followed similar trends, with collagen bundles in loaded samples visible as early as 2 weeks, compared to static constructs that did not show staining for collagen until week 6 (Fig. 6.4 column 4).

The Effect of Dynamic Compression

The most surprising finding was the observed increase in compressive equilibrium modulus by 1.8-2.5 fold for loaded constructs compared to static samples after just 2 weeks of culture ($P < 0.01$) (Fig. 6.5). Increased compressive modulus at 2 weeks coincided with a 70% increase in peak to peak stress during stimulation for 352 μm samples at 11 days compared to 2 days and a 90% increase for 171 μm samples at 2 and 3 weeks compared to 2 days. The increased mechanical performance at 2 weeks did not continue with prolonged loading, with a significant decrease in compressive modulus from 2 to 6 weeks for both samples ($P < 0.05$) as well as a decrease in peak to peak stress (Fig. 6.5).

Table 6.1: Shape fidelity data for cultured samples represented by the number of points from deviation heat maps that fell within $\pm 10\%$, construct volume (target volume 1.5 mL), and construct mass. “*” = difference from 0 week, “+” = difference from static, “%” = difference from 352 μm where $P < 0.05$.

$\pm 10\%$ (%)			
Load	0.29 Week	2 Week	6 Week
Static	43.7 ± 2.2	43.5 ± 2.4	45.1 ± 2.3
171 μm	42.0 ± 2.8	$31.5 \pm 5.1^{*+}$	$28.2 \pm 8.5^{*+}$
352 μm	35.7 ± 2.9	$33.8 \pm 7.3^{+}$	$35.4 \pm 1.5^{+}$
Volume (mL)			
Load	0.29 Week	2 Week	6 Week
Static	1.6 ± 0.3	1.3 ± 0.1	1.5 ± 0.1
171 μm	1.4 ± 0.2	1.3 ± 0.3	$1.1 \pm 0.1^{+%}$
352 μm	1.5 ± 0.1	$1.2 \pm 0.1^{*}$	1.5 ± 0.2
Mass (g)			
Load	0.29 Week	2 Week	6 Week
Static	1.8 ± 0.1	1.6 ± 0.2	1.8 ± 0.1
171 μm	1.6 ± 0.1	1.7 ± 0.3	$1.3 \pm 0.1^{*+%}$
352 μm	1.9 ± 0.1	$1.6 \pm 0.1^{*}$	1.7 ± 0.3

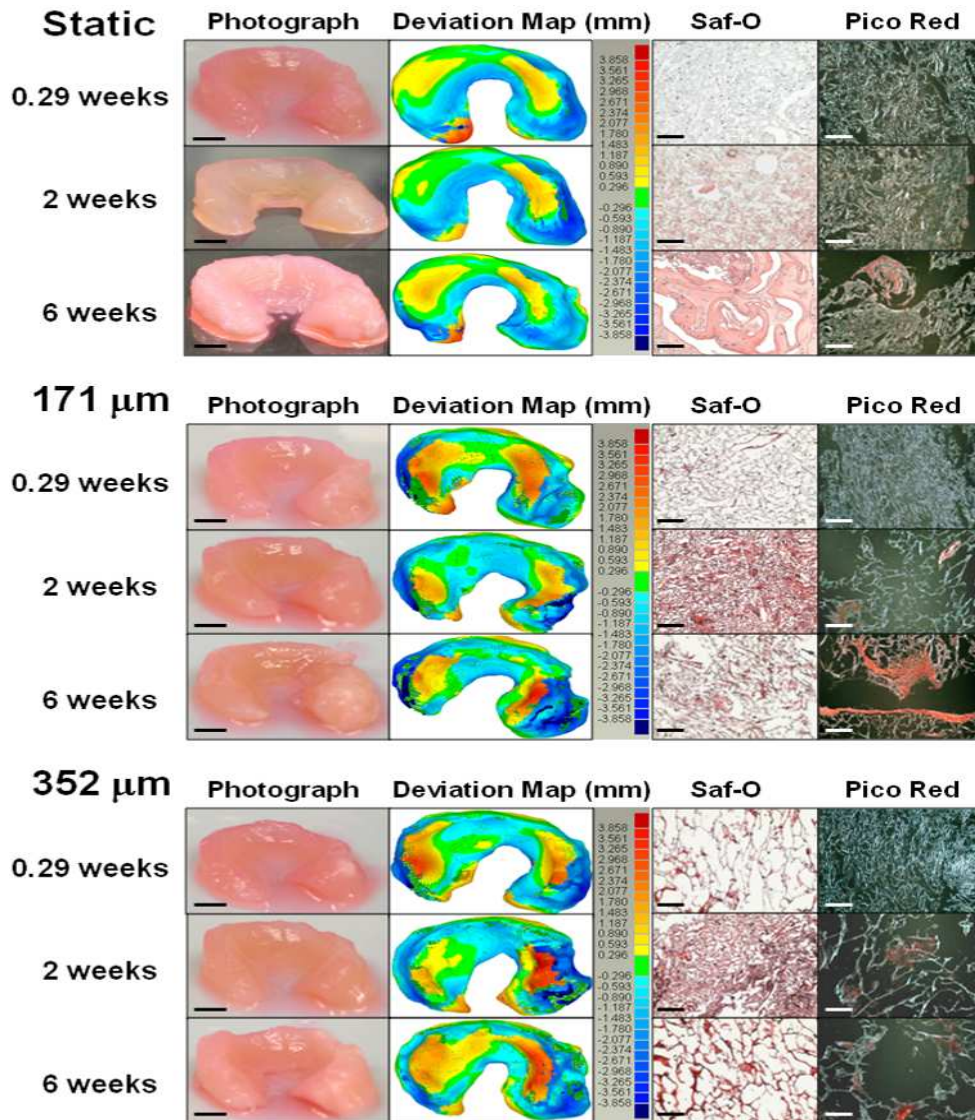


Figure 6.4: (column 1) Photographs of static, 171 μm , and 352 μm groups across 6 weeks of culture, scale bar = 5mm. (column 2) Deviations heat maps of cultured samples, hot colors represent positive errors while cool colors represent negative errors. Each bin represents 5% error from target height. Computationally rendered images from laser scan data yielded surface to surface deviations between native tissue and engineered constructs with errors ranging from -4.3 to 3.9 mm and the majority of deviations between $\pm 593 \mu\text{m}$. (column 3) Tissue sections stained with Safranin-O at 200X original magnification and (column 4) tissue sections stained with picrosirius red at 200X original magnification under polarized light for engineered cartilage at 0, 2, or 6 weeks. Scale bars for stained sections represent 100 μm .

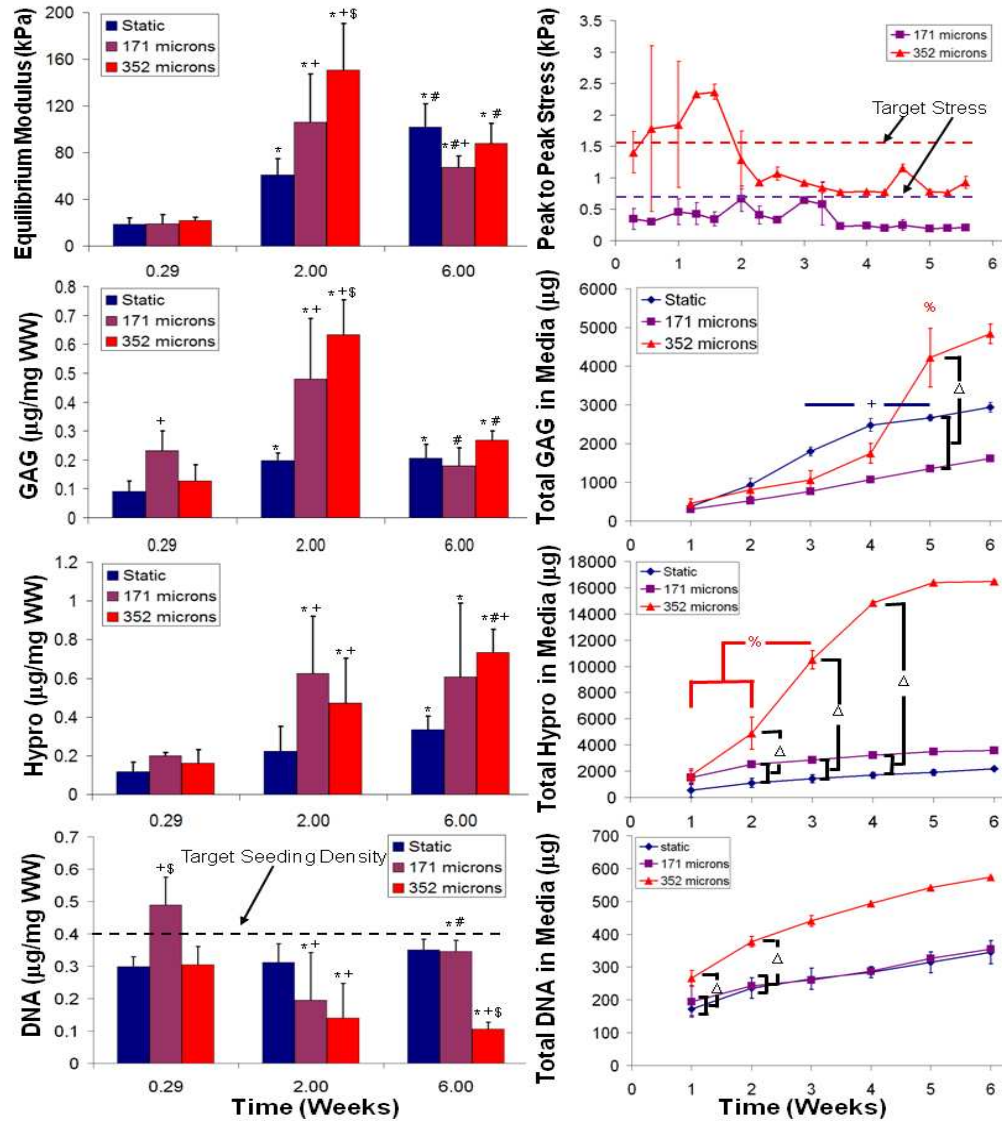


Figure 6.5: Compressive equilibrium modulus, GAG content, collagen content, and DNA content found in engineered constructs (column 1) and cumulative release to the culture medium (column 2) for different culture conditions. Peak to peak stress (column 2) was calculated by dividing the measured load cell force by the contact area of the loading platens. “*” = difference from 0.29 week cultures, “#” = differences from 2 week cultures, “+” = difference compared to respective static time point, “\$” = difference compared to respective 171 μm time point. In column 2 a “ Δ ” denotes a significant difference between media values for that given time point, and the remainder denote differences between respective time points for a given culture condition: “+” = static, “\$” = 171 μm , and “%” = 352 μm . Data presented as mean \pm SD and $P < 0.05$.

Biochemical analysis of these constructs showed a 2.4-3.2 fold increases in GAG content for both loading groups at 2 weeks compared to static controls ($P < 0.001$) (Fig. 6.5). GAG retention (i.e. fraction of synthesized GAG remaining in the sample) at 2 weeks to be 25%, 60%, and 56% for static, 171 μm , and 352 μm groups respectively. However, at 6 weeks there was a significant drop in GAG content for both loading groups ($P < 0.001$) as well as a significant increase in GAG lost to the media ($P < 0.05$). The combined effects of increased GAG loss to the media and decreased content in the construct resulted in lower GAG retentions of 11%, 12%, and 9% for static 171 μm , and 352 μm groups respectively.

Unlike mechanical properties and GAG content, collagen continued to accumulate in constructs throughout 6 weeks of culture for all culture conditions. A 2-2.8 fold increase in collagen content for both loading groups was observed at 2 weeks compared to static controls ($P < 0.05$) (Fig. 6.5). Over the course of 6 weeks 352 μm loaded constructs lost significantly more collagen to the media than either static and 171 μm culture groups ($P < 0.01$) (Fig. 6.5). The high collagen loss to the media had a negative effect on collagen retention for the highest loading condition with retention being 24%, 29%, and 13% at 2 weeks and 21%, 18%, and 7% at 6 weeks for static, 171 μm , and 352 μm groups respectively.

Despite the higher ECM content and mechanical properties at 2 weeks for both loading groups there was a decrease in DNA compared to static controls at 2 weeks ($P < 0.05$) (Fig. 6.5). However, DNA content rebounded at 6 weeks for 171 μm constructs but not for 352 μm constructs. Cumulative DNA content accumulation in the media was greatest for the 352 μm group, while all static and 171 μm groups were similar.

6.5 Discussion

This study investigated the hypothesis that dynamic compression alters the composition and mechanical properties of anatomically shaped tissue engineered menisci. We found that dynamic compressive simulation greatly enhanced matrix accumulation in constructs after just 2 weeks of culture (Fig. 6.4&6.5), and yielded samples with a compressive modulus that was 60 – 80% of native tissue [29] (Fig. 6.5). However, prolonged dynamic compression decreased mechanical properties, decreased GAG content in constructs, and enhanced the loss of ECM to the culture media (Fig. 6.5). These results demonstrate the potential for dynamic compression to enhance the performance of engineered tissues. However, dynamic compression stimulation still needs to be carefully optimized to prevent the negative effects that can ensue with longer cultures times.

Dynamic compression has been previously used to stimulate engineered and native tissues in simple geometries, upregulating ECM production using both meniscal fibrochondrocytes and articular chondrocytes [39, 41, 43, 46, 167-169]. In this study we wished to design a system capable of dynamically compressing an engineered tissue with complex geometry. This complex geometry combined with the non-linear mechanical behavior of hydrogels makes predictions of local stresses, strains, pressures, and fluid flow a challenge. As such, we developed a linear poroelastic FE model to predict the physical stimuli resulting from the imposed displacements. The validity of the model was confirmed by comparing peak-to-peak stresses on day 2 of cultures. Predictions of peak-to-peak load for the FE model (2.25 N) were similar to those measured experimentally (2.07 ± 0.49 N) for the 352 μm condition (Fig. 6.5). For the 171 μm loading condition FE model estimates were higher than measured experimentally (1.1 N vs. 0.51 ± 0.49 N), which may be due to the fact that the measured loads were near the limit of the load cell's resolution.

Dynamic compression stimulation was used in this study because of positive results found in prior studies using this type of stimulation of articular cartilage [39, 40, 46, 170]. The observed 2-3.2 fold increase in matrix accumulation and 1.8-2.5 fold increase in mechanical properties correspond to findings from these previous studies. The loss of DNA from constructs observed in the 352 mm condition could be due to compression-induced fluid flow, forcing cells out of the engineered tissues. The loss of DNA content in alginate constructs could be slowed down by providing cell attachment sites via binding peptides not currently present in these hydrogels.

The decrease in GAG and compressive modulus from 2 to 6 weeks was striking. In addition to the loss of DNA noted above, we speculate that other mechanisms contribute to the decreased mechanical properties in 6 week dynamically compressed samples. Dynamic compression stimulation could be increasing the rate of degradation of the alginate scaffold and also be forcing out newly formed matrix via convective flow induced by compression. This assumption is based on prior work done with mixing media stimulation [171], where higher mixing intensities increased the rate of alginate construct degradation. Another possible cause for decreased tissue performance after 6 weeks of dynamic loading could be an induced catabolic cellular response. Studies of meniscal tissue explants [46] and articular chondrocytes seeded in RGD agarose [170], RGD PEG [167], and peptide hydrogel [40] have found that exposing cells to dynamic strains of 20% or higher and extended continuous loading (i.e. 12-48 hrs) results in cell loss from the construct, increased gene expression of matrix metalloproteinases, and increased ECM loss to the media. Collectively the studies suggest that continuous mechanical stimuli may not be optimal for engineering tissues. As such, optimizing duty cycle of loading duration may be necessary to achieve more functional tissue.

This study began with the hypothesis that dynamic compression stimulation would enhance construct development. We found that dynamic compression has positive effects on mechanical properties and biochemical composition at early time points, but that these effects did not persist with continued loading. As a result, further investigation needs to be done to elucidate the mechanisms for decreased performance by engineered tissue under extended displacement loading.

CHAPTER 7

CONCLUSIONS

This dissertation studied the effect of mechanical stimulation on the mechanical properties and matrix content in TE menisci that were produced by image-guided fabrication methods. Ultimately, the effects of media mixing and dynamic compression were studied. This dissertation completed four tasks. First, a method of fabricating anatomically shaped menisci was developed and then baseline behavior was assessed under static culture conditions (Chapter 3). Second, a method to measure the geometric accuracy of these constructs was developed to confirm claims that patient specific implants could be made via image-guided tissue engineering (Chapter 4). Third, Chapter 5 examined the effects of media mixing on TE menisci over a wide range of mixing intensities (Re 0.5 – Re 21.8). Fourth and finally, Chapter 6 investigated the hypothesis that dynamic compression stimulation will enhance ECM content and mechanical properties in anatomically shaped TE menisci. This chapter discusses the main findings from these studies and presents ideas for future research that emerge from the work presented here.

Chapter 3 documented the development of an image-guided TE approach based on widely used medical imaging modalities and tissue injection molding techniques. Previous tissue engineering studies on meniscal tissue engineering have focused on simple geometries or were limited to generating anatomically shaped molds from simple impression molds. This technique demonstrated a way to acquire patient specific geometry that was non-invasive and could be applied to many other tissues and organs, including cartilage, bone, skeletal muscle, cardiac muscle, and neural tissue. Anatomically shaped constructs were achieved using 2% w/v alginate mixed with 2% w/v CaSO₄ in a 2:1 ratio respectively and allowed to crosslink for 20 minutes in a 60 mM CaCl₂ bath. These constructs were able to remain viable for 8

weeks of static culture achieving an equilibrium compressive modulus that was 50% of the native tissue. Constructs maintained shape fidelity throughout culture, but had what appeared to be a more opaque necrotic center. After biochemical analysis, the opaque center was found to have the highest concentration of matrix throughout the bulk of the tissue. As a result of this work, two goals were pursued in tandem. First, develop a method to measure the accuracy of engineered menisci and second, to study the effects of media mixing on the spatial ECM composition of these large volume hydrogels.

The method presented in Chapter 4 was developed to confirm that injection molding and 3D tissue printing could generate anatomically accurate tissues based on medical imaging modalities such as MRI and μ CT. It is commonly found in the literature that studies which claim to produce anatomically shaped engineered tissues then present little or no data comparing the accuracy of the engineered tissue to the tissue's native geometry. Since this dissertation also claims to have engineered anatomically shaped TE menisci, it seemed appropriate to both compare the geometry to the native tissue, as well as design a method that would allow for automated and quantitative geometric comparisons. Utilizing a commercially available laser triangulation distance sensor and image processing software, it was possible to digitize the geometry of the hydrogel and compare it to a digital rendering of the native tissue using previously established points of interest [150]. This research found that both injection molding and 3D printing could produce anatomically accurate TE menisci with high geometric fidelity using either MRI or μ CT imaging modalities. Both fabrication techniques demonstrated good repeatability, though injection molding was the more reliable method with superior shape accuracy. Molds based on μ CT images performed better than MRI-based molds, but this could be a result of the imaging resolution as well as the different imaging environment (i.e. MRI images in the knee

while μ CT image excised tissue that is unloaded). Improving the shape fidelity of TE constructs in future research depends on further development of control feedback 3D printing to minimize deviation from native tissue as well as improved MRI technology that can generate high-resolution scans which can be undertaken given clinical time restraints.

While media mixing is commonly used in tissue engineering studies with articular chondrocytes to improve nutrient transport, little research has been undertaken which studies meniscal fibrochondrocytes in large volume constructs. Chapter 5 examined the effects that different media mixing intensities have on anatomically shaped TE menisci. Media mixing resulted in more homogeneous ECM distribution and mechanical properties throughout the engineered tissue. It was also observed that lower mixing intensities (Re 0.5 and 2.9) increased both ECM content and mechanical properties in engineered tissues, while higher mixing intensities (Re 5.8, 10.2 and Re 21.8) decreased mechanical properties despite an increase in ECM content. Even though there was an increase in GAG content for turbulent mixing intensities (Re 10.2 and Re 21.8), there were no increases in compressive properties. As such we hypothesized that media mixing altered the rate of alginate degradation. A test done with acellular alginate hydrogels confirmed that alginate degradation rates increased with amplified mixing intensity. This conclusion of the research presented in Chapter 5 was that media mixing can be modulated to optimize construct growth.

Chapter 6 reviewed the research that attempted to design a system to dynamically compress anatomically shaped TE menisci. This study investigated the hypothesis that dynamic compression enhances ECM content and mechanical properties of TE menisci. Previous work has studied the effects of dynamic compression on articular chondrocytes and meniscal fibrochondrocytes in simple geometry small volume plugs resulting in increased ECM production [39, 41, 43].

Anatomically shaped TE menisci had significant increases in matrix accumulation and a compressive modulus that was 60 – 80% of native tissue. However, prolonged compressive loading decreased mechanical properties, decreased GAG content in constructs, and enhanced the loss of ECM to the culture media. The decreased mechanical performance of engineered constructs could be due to an increased rate of alginate degradation, as seen in the media mixing study, or an induced catabolic cellular response. Studies of meniscal tissue explants and articular chondrocytes seeded in various scaffolds have yielded similar results when exposing cells to dynamic strain of 20% or high and extended continuous loading (i.e. 12 – 48 hrs). These results demonstrate the potential of dynamic compression to enhance the performance of engineered tissues, but suggest that continuous mechanical stimuli may not be optimal for the engineering of functional tissues.

The studies presented in Chapters 5 and 6 of this dissertation are the first attempts to examine the effects of dynamic stimulation on large volume anatomically shaped TE menisci. The findings presented highlight 1) the effectiveness of image-guided fabrication techniques in generating patient specific TE implants (Chapters 3 and 4), and 2) the potential of mechanical stimulation to enhance tissue growth in engineered constructs (Chapters 5 and 6). However, comparing biochemical and mechanical data among different culture conditions (Fig. 7.1), we see that the compressive behavior of these constructs does not always correlate with GAG content. Also observed, the tensile properties are unaffected by ECM composition which is likely due to the absence of an aligned collagen fiber network. For higher mixing intensities such as Re 5.8, lower compressive properties can be explained by the increased degradation rate of the alginate scaffold (Fig. 7.1). Likewise, the decrease in GAG content and compressive modulus from 2 to 6 weeks in 352 microns loading samples can also be attributed to alginate scaffold degradation which results in not

only a release of GAG from scaffolds, but a loss of scaffold mechanical integrity. However, in comparing statically cultured samples to Re 2.9 constructs, very similar amounts of GAG are accumulated in these engineered tissues. However, Re 2.9 have a significantly higher compressive modulus at 6 weeks (Fig. 7.1) The only difference between the Re 2.9 culture group and the static group is the collagen content—as denoted by the hydroxyproline content—in which Re 2.9 has significantly more collagen than static samples at both 2 and 6 weeks.

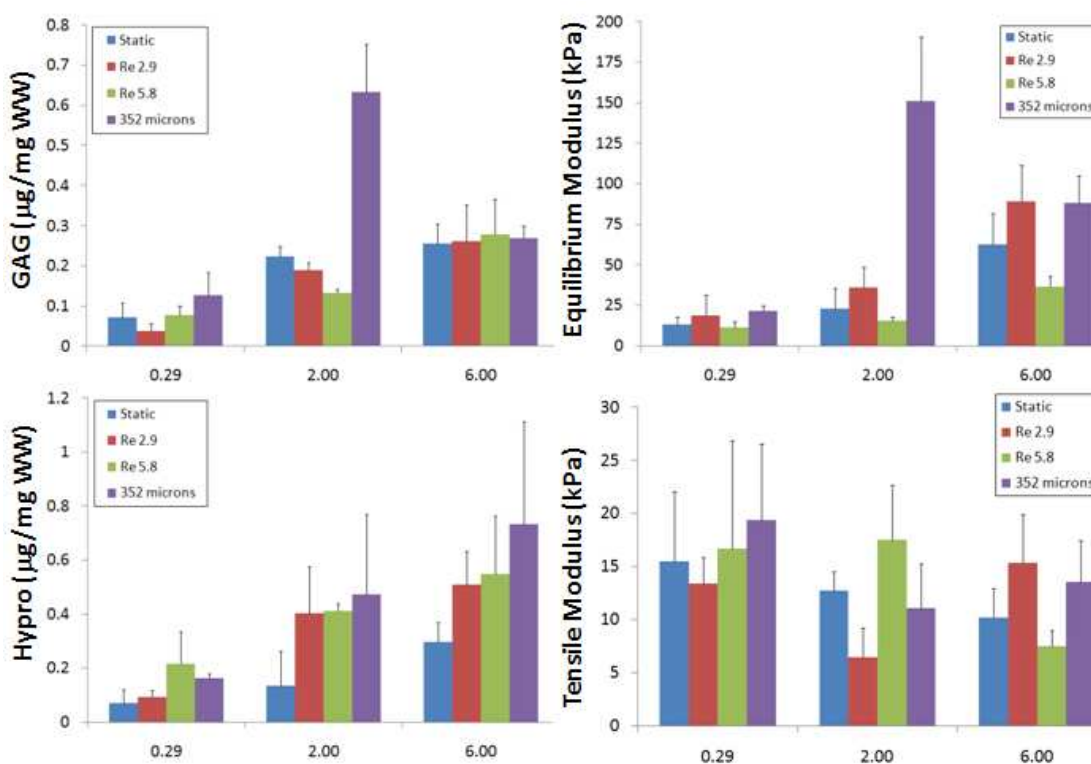


Figure 7.1: GAG content, hydroxyproline (Hypro) content, compressive equilibrium modulus and tensile modulus for engineered tissues exposed to varying culture conditions at 0.29, 2, and 6 weeks.

It has long been known that the mechanical properties of articular and fibrocartilage are a result of the composition and organization of the ECM. The compressive properties are primarily a result of the GAG content and tensile properties, dependent on the collagen content and fiber orientation. In order to better

explain the influence of each ECM component and how it contributes to the compressive equilibrium modulus of the tissue engineered menisci generated in this dissertation, the rule of mixtures was applied. This rule is represented by: $E(t) = E_{Alg}[Alg](t) + E_{GAG}[GAG](t) + E_{Col}[Col](t)$. Where E_{Alg} is the modulus constant for alginate, E_{GAG} is the modulus constant for GAG, E_{Col} is the modulus constant for collagen, $[Alg](t)$ is the amount of alginate in the construct as a function of time, $[GAG](t)$ is the concentration of GAG as a function of time, and $[Col](t)$ is the concentration of collagen in the construct as a function of time. The exponential growth and decay equations for alginate, GAG, and collagen were fitted to the data for each culture condition based on work by Wilson et al. the data which can be found in Appendix E [172].

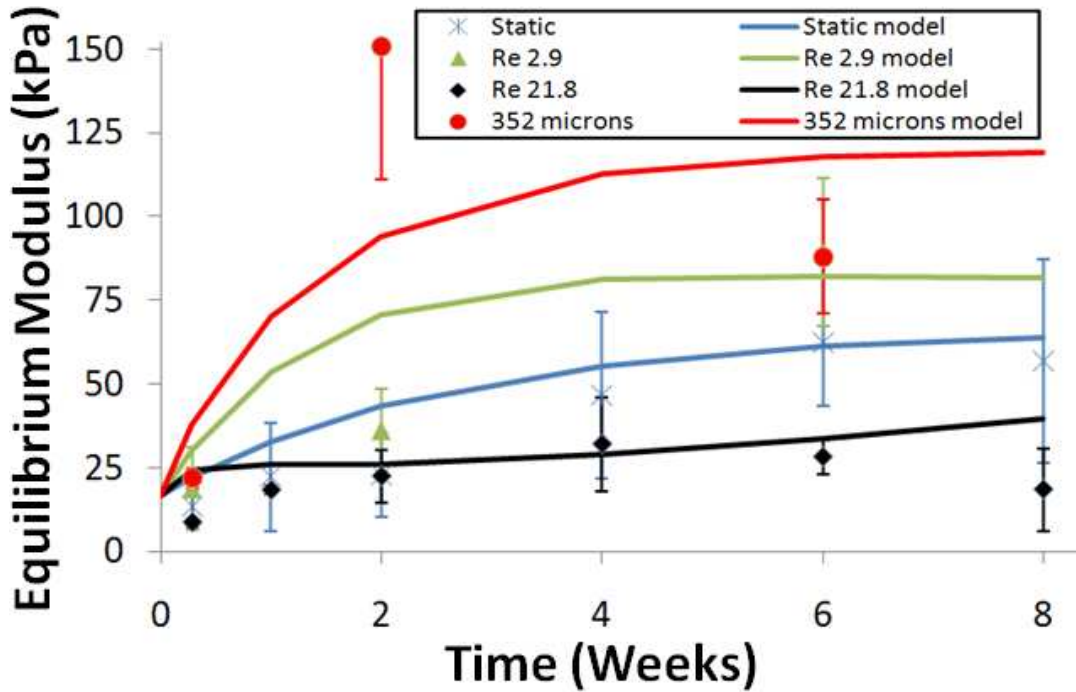


Figure 7.2: $E(t)$ model using rule of mixtures for static, Re 2.9, Re 21.8, and 352 microns (lines) along side measured compressive modulus values.

The model fits were entered into the compressive modulus equation, $E(t)$, for each respective culture condition. The constants E_{Alg} , E_{GAG} , and E_{Col} were found by

fitting the model to the static free-swell culture condition resulting in 1.5 kPa/g, 45 kPa, and 130 kPa for each, respectively. These values were then used for the Re 2.9, Re 21.8 and 352 microns culture conditions E(t) models (Fig. 7.2). Surprisingly, collagen plays a large roll in contributing to the compressive properties of engineered constructs as indicated by the higher compressive modulus in Re 2.9 group compared to static controls which have similar GAG content, though the Re 2.9 group did have more collagen. GAG content has typically been considered to be the highest contributor to compressive modulus based on theories describing articular cartilage. However, in the meniscus, GAG makes up only 2 - 3% of the dry weight matrix [8, 9] which is 5 times below what is found in articular cartilage [173]. The meniscus have a compressive modulus that is $\frac{1}{2}$ that of AC [9, 173], meaning that the collagen matrix must be providing some type of compressive support as it does not follow the same behavior as would be expected in articular cartilage. Further support from our model shows that collagen plays a crucial roll in compressive properties and can enhance the modulus when coupled with a stable scaffold and/or enhanced GAG accumulation.

The model estimations predict the compressive properties at longer time points very well (i.e. 6 and 8 weeks). In addition, we have also learned by modeling the compressive equilibrium modulus as a rule of mixtures system that scaffold integrity plays a larger role in the overall mechanical properties of engineered menisci than previously thought. As the scaffold breaks down, not only are more cells and ECM components lost to the media, but their ability to provide resistance in compression is also negated to a much greater degree.

Media mixing and dynamic compression are two different ways to approach the same problem. Media mixing was used to improve transport and removal of nutrient and waste products, while dynamic compression served as a direct mechanical stimulus to amplify ECM production by the cells. The data suggest that direct

mechanical stimulation is a more effective form of stimulation that can cause more rapid increases in ECM and compressive properties. However, media mixing can serve as a more passive form of dynamic stimulation for engineered constructs that are not being dynamically loaded, particularly at lower mixing intensities.

While both forms of stimulation had a range (i.e. mixing intensity or time) where tissue properties were improved, large problems still exist in using these forms of stimulation. For example, media mixing and dynamic compression with unmodified alginate gels resulted in significant cell loss and ECM loss to the media. Higher mixing intensities and continuous compressive loading resulted in poor compressive properties at later time points. The similarities between these two very different forms of mechanical stimulation suggest the imperative nature of proper modulation and optimization of exposure to stimulatory forces. In the context of the goals of tissue engineering, this dissertation did not produce an engineered menisci capable of *in vivo* implantation, but did exemplify the critical role image-guided TE and mechanical stimulation will play as tissue engineering works towards creating tissues that mimic what is found in the body.

Looking forward, mechanical stimulation is a valuable tool in tissue engineering because of its ability to enhance ECM production in meniscal cells. As such, this work did not analyze gene expression, as typically performed in other tissue engineering studies to verify cell behavior; high amounts of GAG and collagen were being produced by cells and it was obvious that gene expression was not a problem in this current setup. However, this research does suggest two major problems which emerge as a result of mechanical stimulation, both for media mixing and dynamic compression. First, although a system now exists that stimulates cells to produce ECM nearing values found in native tissue, the synthesized matrix is not being retained in the scaffold. Second, mechanical stimulation increases the rate of scaffold

degradation, which in turn increases cell and matrix loss to the media. The identification of these future issues is a key contribution of this dissertation research.

Alginate was originally chosen as a scaffold because it is a biocompatible material ideal for the image guided fabrication techniques developed in this dissertation. Alginate was also selected because it will degrade during *in vitro* culture. Ideally, as the scaffold degrades it is replaced by newly synthesized ECM. Moving forward, the challenge will be to figure out the optimal way to further increase ECM output from cells. Optimizing ECM production might be accomplished either through growth factors or other mechanical stimulation techniques. Along with increasing ECM output, cell and matrix retention in the scaffold needs to be increased and could be made possible through the modification of alginate with binding peptides or by designing a novel composite material. These problems and solutions will be discussed in more detail in the next section.

7.1 Future Directions

This dissertation has developed many new methods for tissue engineering anatomically shaped constructs, focusing on the meniscus due to its geometric complexity. While key questions are answered by the results presented in this dissertation, many questions emerge. The meniscus is a very complex tissue with an intricate collagen network and experiences mechanical stimulation that extends far beyond dynamic compression and fluid flow (i.e. media mixing). This section presents potential areas of future investigation that would strengthen our knowledge of how to generate tissue engineered menisci that mimics native tissue.

Introduction of growth factors

This research did not introduce any growth factors that are known to induce a biochemical response in meniscal fibrochondrocytes similar to that which was observed with mechanical stimulation. Research has only just begun to examine these effects in statically cultured samples supplemented with insulin-like growth factor-I (IGF-I). TGF- β and IGF-I are two growth factors known to upregulate matrix synthesis in articular chondrocytes [174] and meniscal fibrochondrocytes [127, 175]. Future work should look to combine growth factor stimulation with mechanical stimulation to see if there is a synergistic effect when both are present during *in vitro* culture.

Altering biomaterial properties

Comparing this work in our laboratory to other meniscal tissue engineering efforts, when compared to native tissue, alginate hydrogels perform poorly in tension. Tensile properties are of particular interest because one of the primary functions of the meniscus is to redistribute compressive shock forces through tensile hoop stresses. Currently, PCL meshes have been able to generate tensile properties nearing those of native tissue, but provide no compressive resistance [30]. Through the use of 3D tissue printing alginate could be combined with PCL meshes to produce a composite material that is able to withstand hoop stresses when exposed to an *in vivo*-like loading regime. Generating a composite construct with PCL and alginate would also provide ligament/suture attachment sights necessary for future animal studies, which are not currently present in alginate hydrogels.

Another area of future research should attempt to limit the amount of cell loss to the media from TE menisci. Dynamic compressive loading results in significant cell

loss in many different biomaterials such as alginate, agarose, PEG, etc. Altering the loading protocol to loading constructs every other day has shown to decrease construct cell loss, but more research could be conducted to modify the scaffold chemistry so that this result could be prevented. One possibility is to modify the alginate hydrogels with Arginine–glycine–aspartic acid (RGD) to provide attachment sites for cells. By providing attachment sites for meniscal fibrochondrocyte in alginate scaffolds, I hypothesize that two things will happen: 1) more cells will remain in TE menisci for a longer period of time, and 2) an increase in ECM content and mechanical properties as a result of the synergistic effects of having more cells and providing cell attachment sites. Modifying alginate hydrogels with RGD has been shown to increase cell sensitivity to mechanical stimulation [167]. With more cells present, more matrix may be generated and could be modified according to the stimuli in which they are presented. This dissertation provides the foundation for future research for reducing cell loss.

Finally, this research demonstrates that under dynamic compression, much of the collagen is being lost to the media. The total collagen produced during the 6 weeks of dynamic compression culture neared values close to those in native tissue. Despite this achievement, there is a lack of fiber bundles in these tissue engineered constructs. I hypothesize that if more of the collagen generated by the cells remained present in the scaffold for longer that collagen molecules will be more likely to modify into fiber bundles in extracellular spaces. Trapping more collagen in the scaffold may allow time for collagen subunits to self-assemble and form fiber bundles with the aid of other proteins present, including other collagens, glycoproteins and proteoglycans also produced by the cells. Similar to the work done with modifying alginate with RGD to bind cells, alginate chemistry could be altered to contain CD36 or CD44 binding sites that are capable of attaching to collagen. Another approach could be utilizing 3D

printing technology and fibronectin to print concentric layers of fibronectin within the alginate construct. Fibronectin is known to bind to cells, collagen, and many other ECM components. By printing multiple layers within the alginate scaffold multiple barriers will be available for cells and ECM to bind to before being lost to the media. These approaches may lead to engineered tissues that better mimic the properties of native tissue.

Optimizing mechanical stimulation protocol

This study has shown that prolonged compressive stimulation is to TE menisci. However, the first two weeks of compressive loading resulted in improved tissue properties. Future work should explore different loading protocols to elucidate the cause of decreased tissue performance with extended loading times. Cells may be able to remodel the tissue and produce more robust engineered constructs if given more time to rest after an initial 2 week loading period. These studies have already begun in our lab and preliminary results are promising based on gross tissue inspection.

Another avenue to explore is implementing a system that provides multi-modal stimulation (i.e. compression, tension, shear, and fluid flow). Currently, studies have only focused on compression and fluid flow stimulation on meniscal fibrochondrocytes. These studies have been limited to simple geometry gels. To move forward, this field needs to generate bioreactors that are capable of exposing these delicate hydrogels to multiple mechanical stresses to guide tissue maturity for implantation into the body.

This dissertation has clearly presented both the contributions of the research presented in this dissertation as well as actionable ideas for future research. It has been shown that mechanical stimulation is crucial tool in tissue development. Looking

forward mechanical stimulation can be combined with other cell stimulating factors to work towards generating a living synthetic meniscal replacement that could have the potential to impact over a million American lives each year.

CHAPTER 8

AN INTRODUCTION TO TISSUE ENGINEERING USING HYDROGELS

Submitted to *Science Scope* 5/14/2010⁶

8.1 Abstract

Tissue engineering is a field that applies the principles of engineering and biological sciences to create substitutes for damaged tissue. Tissue engineering is a relatively new field in biomedical engineering with a wide variety of applications that range from synthesizing living heart valves and kidneys to other tissues like bones and ears. This article presents an engaging classroom activity that allows students to learn about tissue engineering and replicate research done at Cornell University. The inquiry-based instructional unit was designed in collaboration with a New York middle school 8th grade science teacher and a Cornell University biomedical engineering graduate student. The activities allowed students to get hands on experience with hydrogels, injection molding techniques, and allowed them to explore how to make various alginate hydrogels with different mechanical properties. The ultimate goal of the activity was to make the stiffest gel possible. The overall class performance increased from Pre- and Post-Quiz scores ($P < 0.001$) and all students gave the activity a lot of praise that corroborated our observations in the class room. This activity can be applied to not only middle school classes but also can be used for high school chemistry, physics, or biology classrooms.

8.2 Introduction

Being a part of the National Science Foundation's (NSF) GK-12 program has been an honor and highly educational experience. The NSF Graduate STEM Fellows

⁶ Ballyns JJ, Doran RF, Archer SD, and Bonassar LJ. An introduction to tissue engineering using hydrogels. *Science Scope* 2010; Under Review.

in K-12 Education (GK-12) program paired graduate students in Science, Technology, Engineering and Mathematics (STEM) with a middle or high school science teachers. This chapter will present the activities I have participated in throughout my year in the GK -12 program, the benefits I have gained, and lessons I have taken away from this experience, and end with an article submitted to Science Scope on the lesson plan Rob Doran (Newfield Middle School science teacher) and I implemented in his General Science class.

The Cornell GK-12 Program–Cornell Learning Initiative in Medicine and Bioengineering (CLIMB) starts off with a 6 week summer program where graduate fellows and teachers are paired to develop curriculum based on the fellow’s research and summer research project specially designed for teachers. Also during this time fellows and teachers take part in workshops on inquiry based teaching. During the academic year the fellow spends approximately a day a week in the classroom acting as a science mentor and implementing the curriculum developed.

These activities are meant to enrich both the teacher and graduate student to allow for improved quality in graduate research and classroom teaching. It has been reported that the NSF GK-12 program has had a large impact on past Cornell GK-12 fellows. Their teaching skills were enhanced, there was a positive impact on the fellow’s research, as well as increased interest in educational outreach, better time management skills, and improved self-confidence [176]. Like the fellows before me, I also shared similar improvements and benefits for being a part of the NSF GK-12 program.

As part of the GK-12 program I was given the opportunity to design and implement my own summer research project for my partner teacher. In doing so, I was also able to hone my training abilities and show research techniques to someone not necessarily familiar with tissue engineering. The project consisted of generating an

alginate-collagen hydrogel composite by mixing different concentrations of alginate and collagen solutions together. The measured outcomes included, mechanical testing, geometry measurements, cell morphology inspection via microscopy and second harmonic generation microscopy to view collagen bundles. While the project was not necessarily a success due to the lack of observable changes in cell morphology, geometry or evidence of collagen bundle formation in these composite gels, Mr. Doran was able to learn sterile technique, create viable tissue engineered composite discs and culture them for up to 2 weeks. If given more time I feel confident that together we could have further developed this work to create a composite structure that would have yielded the results we were looking for.

Throughout the academic year I visited Mr. Doran's class to aid with demonstrations and lab experiments. I was also given an opportunity to teach classes to practice lecturing and leading experimental lab sessions. Some of the lab experiments I participated in at Newfield Middle School included a Mentos© and Coke© experiment to teach the scientific method, a density lab using density cubes to practice measuring volume and mass to calculate an objects density, a roller coaster lab to teach students about momentum, and an optics lab to teach students about light properties and fiber optics. Mr. Doran and I also did a forensic investigation lab where the class was set up as a crime scene and students acted as the detectives to solve the murder of Timmy the baby seal. The students would determine who committed the crime based on some clues and a gun shot residue kit. We also provided class demonstrations which included a dry ice day to teach students about sublimation and phase changes of matter as well as a vacuum demonstration so students could visualize Boyle's Law. The dry ice demo included floating soap bubbles on a CO₂ cloud, exploding film canisters, a shivering quarter, a screeching quarter, and a CO₂ magnesium sandwich fire. The vacuum demo allowed students to observe pressure

volume relationships by watching balloons and marshmallows expand under a vacuum as well as altering the boiling point of water. While students were mostly observing for the class demonstrations they all seem captivated by what they saw and very willing to interact and ask questions.

Before the GK-12 teaching experience I had only been exposed to teaching through a one week CURIE Academy outreach program for high school girls and as a teaching assistant for Professor Bonassar's class entitled, "Biomedical Engineering Analysis of Metabolic and Structural Systems". Before this I was not sure if I was interested in teaching. I did enjoy leading lab sessions and aiding students with their projects. I also enjoyed guiding and helping undergraduates with their research and sharing the joys of their success when it turned out well resulting in accepted abstracts or prizes in Cornell research competitions. However, what I did not enjoy was holding office hours to go over homework. I now realize that I did not always adequately prepare and expected students to ask pertinent questions that would facilitate me aiding them with solving problem sets. However, students would come without any informed questions and expect the answer to be given to them. Through NSF GK-12 program I found that students in middle school acted exactly the same way. If they arrived at something they did not know they simply raised their hand and said, "I don't know this," expecting to have the answer given to them. Eventually I changed my strategy by preparing a list of questions students should ask when they approach a problem so that when they came for help, if they simply said, "I don't get this," I would have questions to ask them. This eventually led to the student making a connection to the material they learned before. By the end of the semester and the end of the school year students would stop saying they didn't understand and instead ask for help with an intuitive question. Learning and improving this approach has aided

me in my teaching ability, my mentorship to students in the lab, and also has improved my attitude towards teaching.

I participated in the NSF GK-12 program in my final year of my Ph.D., the program did not change my approach to my research or have a large impact on my time commitments, as most of my research experiments were completed with the exception of some data analysis. None the less, being a NSF GK-12 fellow has been a privilege, something I am definitely proud to put on my Curriculum Vitae, and has vastly changed my outlook on pursuing a career in academia. Designing the interactive curriculum with Rob Doran took a lot of time and effort, but the result was very rewarding to me and I hope for the students as well. The curriculum, which is presented later, combined with other lab experiments and demonstrations I did in class really helped stimulate interests in science. I think the program was very successful and gave these students a great opportunity to learn and participate in an activity based on university level research.

8.3 Article Background

Biotechnology has often been a favorite topic in popular culture, while this has provided some introduction to the futuristic potential of biotechnology and biomedical sciences, it does not often translate to activities that will excite and stimulate students academically. Moreover, middle and high school students are not always aware of current research and how it benefits mankind. Here we present a three part classroom activity that introduces students to examples of research in the field of tissue engineering, and allows them to replicate experiments being done in university laboratories utilizing alginate hydrogels.

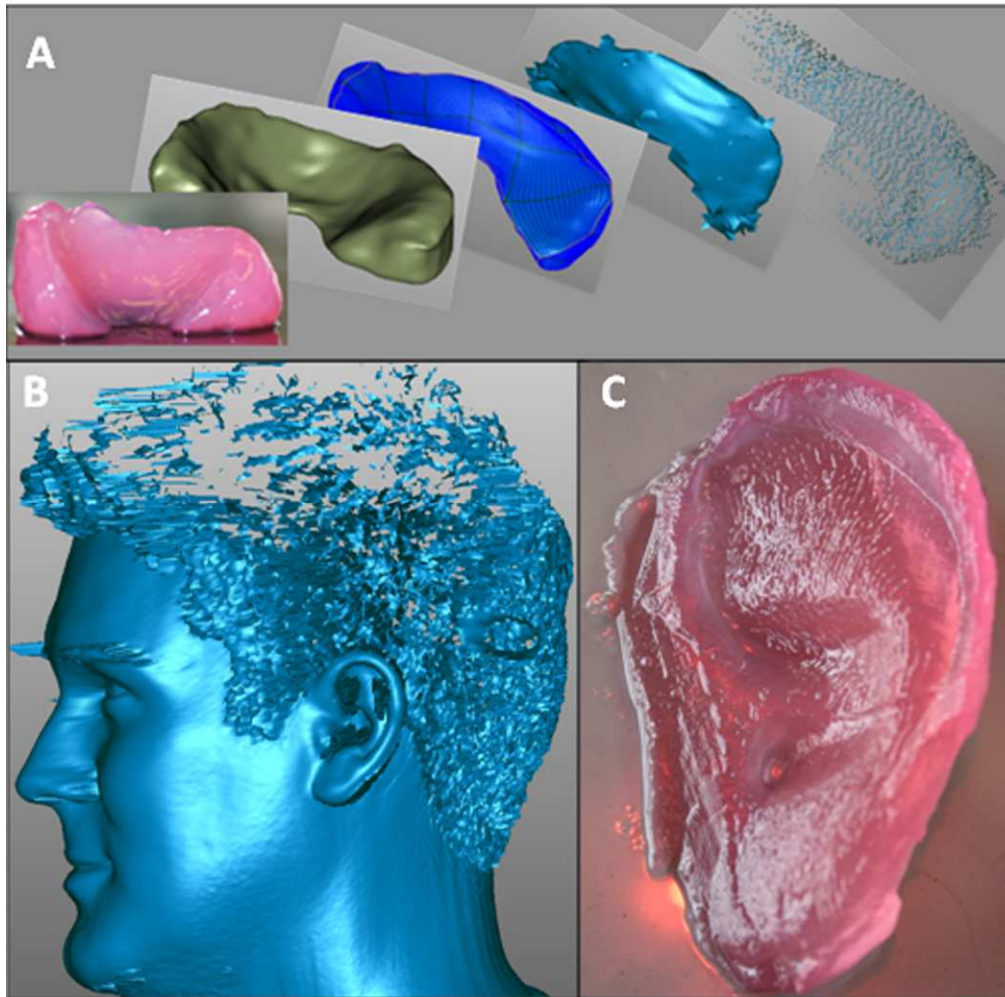


Figure 8.1: (A) Example of a point cloud image from an MRI scan being used to design a knee meniscus for tissue engineering. (B) Laser scan of a human head to generate a tissue engineered ear (C).

What is Tissue Engineering?

Tissue engineering is a field that applies the principles of engineering and biological sciences to create substitutes for damaged or diseased tissue [56]. It is a relatively new field with a wide variety of applications that range from synthesizing living heart valves and kidneys to generating tissues like bone, ears, and the meniscus

of the knee. Relating current tissue engineering research to the health costs associated with diseases can help captivate students' interest. Many students know that entertainment icons make millions of dollars annually, but have no appreciation that healthcare costs to treat ailments such as heart disease, kidney failure, or various musculoskeletal injuries/disease (hip and knee replacements) can range from 1 to 900 billion dollars annually [177]. At Cornell University, some current tissues being modeled include the meniscus of the knee and the human ear (Fig. 8.1) [29].

Materials used in Tissue Engineering

Engineered tissues are generated by utilizing biomaterials that mimic native properties and can support the biological function of living cells. A biomaterial is a non-toxic, synthetic material used to replace part of a living system or function in a living tissue usually combined with cells [32, 56]. Hydrogels are a popular type of biomaterial used in tissue engineering. They are made of highly absorbent polymer networks that contain more than 90% water and have a degree of flexibility very similar to natural tissue. Alginate is a hydrogel ideal for tissue engineering applications because it is biocompatible with cells and can be injection molded to make many shapes and tissues. It is extracted from brown algae or seaweed as a viscous liquid and gels when combined with calcium. Some typical uses for alginate include as a food additive/thickener or making impression molds of teeth/body parts [178].

Characterizing the strength of engineered tissue

It is important to characterize the strength of the engineered biomaterials since they have to perform many mechanical functions in the body. Most building materials such as steel, aluminum and concrete are treated as linearly elastic materials (Fig. 8.2 Q6 left plot) i.e. they deform linearly when exposed to stress, and return to their initial position when the stress is removed. However, alginate and many other soft tissues in the human body are viscoelastic materials (Fig. 8.2 Q6 right plot). A viscoelastic material has both viscous and elastic properties, but is dependent on time, temperature, stress and strain rates. Stress and strain can be used as an evaluation tool to compare materials. Stress is defined as a force that produces strain on a body and can be represented mathematically as: $Stress = \frac{Force}{Area}$. Strain is a measure of how much a material deforms (i.e. compresses or elongates) for a given stress. By plotting stress vs. strain one can calculate the stiffness of a material as the slope of the linear curve [179]. This is important since, a stiffer tissue engineered construct would be more appropriate for a knee cartilage that has a high mechanical load versus ear cartilage which does not.

8.4 Tissue Engineering Activity

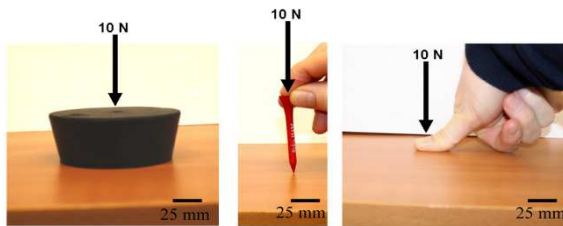
The instructional unit was designed in collaboration with a New York State middle school 8th grade science teacher and a Cornell University biomedical engineering graduate student. The activity took an inquiry based approach, where students were engaged in open ended, student centered discovery. In this three part activity foundation lectures and demonstrations were presented on the first day. This gave examples of how tissue engineering can be used in medicine and to repair the human body and taught the concepts of biomaterials, hydrogels, stress, force, and linear elastic vs. viscoelastic materials. In the second part, students made alginate molds of sheep menisci alginate sheets, and cylinders. Then on the 3rd day, they were

provided with different concentrations of alginate and different types of cross-linkers to experiment and explore what combinations would result in the stiffest gel. The activities allowed students to get hands on experience with hydrogels and injection molding techniques. Students were given a Pre- and Post-Quiz to evaluate what they learnt from the class lecture and activities (Fig. 8.2). They were also given an open ended question to write what they thought of the lesson. This activity can be applied to not only middle school general science classes but also to high school chemistry, physics, or biology classrooms.

1.) Define Tissue Engineering: _____

2.) What is a Biomaterial? _____

3.) Which of these is imposing a higher stress on the table? (circle one)



(A) (B) (C) (D) All are the same

4.) $Stress = \frac{Force}{X}$ Which of the following is the correct answer for X?

(A) Acceleration (B) Mass (C) Area (D) Velocity

5.) Force = Mass x (Z) which of the following is the correct answer for Z?

(A) Acceleration (B) Mass (C) Area (D) Velocity

6.) Which of the following represents a Stress-strain plot of a viscoelastic material? (circle one graph)

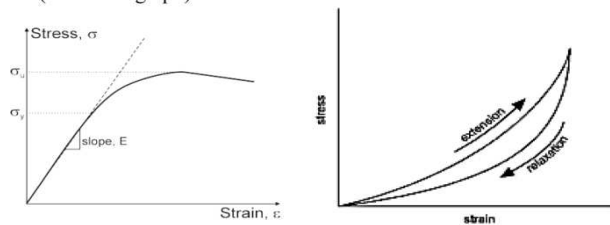


Figure 8.2: Quiz given to student before and after 3 day lesson.

DAY 2

Making Alginate Gels!!!!

Supplies for each desk:

- 1 beaker with 50 mL 2% (w/v) Alginate (Protanal LF 10/60 sample; FMC BioPolymer, Drammen, Norway)
- 1 beaker with 50 mL 2% (w/v) CaSO₄ (Cat# C1015-500g; Sigma-ALDRICH Co., St. Louis, MO)
- 1 beaker with 50 mL 2% (w/v) CaCl₂ (Cat# 237132-500g; Sigma-ALDRICH Co., St. Louis, MO)
- 1 beaker with 50 mL tap water
- 4 10 mL syringes (10 mL syringe Luer-Lok tip; BD, Franklin, NJ)
- 2 3-way stopcocks (Standard bore 3-way stopcock with rotating luer lock; Baxton Healthcare Corporation, Deerfield, IL)
- 2 syringe tips (these are not needles! Part# 5118-1-B; EFD-Inc.)
- 1 silastic rubber meniscus mold (Can be made into any shape using Silastic E RTV Silicone Rubber base and curing agent; Dow Corning Corporation, Midland, MI)
- or
- 1 (ABS) plastic meniscus mold (custom made)
- 1 15 mL conical tube
- 1 set of glass plates with 1mm spacers
- 2 biopsy punches (6 mm biopsy punch REF 33-36; Miltex, Inc., York, PA)
- 2 mini spatulas

Goal: Today you will be repeating what Mr. Doran and I did/do at Cornell University. Your goal is to play with alginate, make an alginate meniscus and HAVE FUN!!!!

Steps:

- 1.) Make sure you have all the items listed above at your work station. If you are confused as to what an item is please ask for help.
- 2.) Choose a meniscus mold (silastic rubber or ABS plastic)
- 3.) With one syringe pull up 3 mL of alginate. Make sure to get rid of as many air bubbles as possible!
- 4.) Attach the syringe to the 3-way stopcock. Make sure to squeeze out any air and then close off the alginate port. If you are not sure how to do this please ask for help.
- 5.) Draw 1.5 mL of 2% CaSO₄ into the other syringe and get rid of air bubbles. Make sure the CaSO₄ is well mixed before you draw out the amount you need.
- 6.) Quickly, attach the syringe to the other port on the 3-way stopcock and squeeze out the air.
- 7.) Attach the syringe tip to the last open port on the 3-way stop cock and put the tip into the hole of the mold. Ask for help if you are having trouble finding the correct hole.
- 8.) Turn the knob towards the syringe tip and rapidly mix the alginate and CaSO₄ 4 times, then turn the knob to the empty syringe and inject the mixture into the mold.
- 9.) Quickly remove the tip from the mold and place the mold in the CaCl₂ beaker. Allow it to sit in the beaker for 20-30 minutes then remove from mold.

Make an alginate sheet:

- 1.) Place aluminum spacers on top of 1 glass plate so that they are parallel with the ends.
- 2.) Repeat steps 1-5 from above.
- 3.) Mix alginate and CaSO₄ 3 times and quickly squirt alginate onto the plate and rapidly set the other glass plate on top.
- 4.) After 5minutes try and slide the top plate off without tearing the alginate sheet.
- 5.) Make as many disc as you can with the biopsy punch.
- 6.) Place some in the CaCl₂ beaker for a minute or 2 and then fish it out and observe how it has changed compared to the other discs.
- 7.) Repeat as needed.

Clean up work station at the end of class

Figure 8.3: Hand out for students with a list of materials and instruction for the first alginate activity.

8.5 Alginate Activity #1

Materials and Teacher Preparation

A list of materials for each group is given in Fig. 10.3. During this activity each group was supplied with a 15 mL conical tube and a set of 130 mm x 130 mm glass plates with 1 mm thick aluminum spacers. The conical tube was used to make a solid cylinder of alginate and a sheet of alginate was made using the glass plates and spacers (Fig. 8.4A).

Before class, the teacher should prepare the 2% weight/volume (w/v) alginate with de-ionized or distilled water using a magnetic stir bar. For a class of 60 students 1 L of alginate is recommended and it should be stored in the fridge overnight. The alginate solution will typically keep for up to 2 days. The 2% w/v CaSO_4 (medium speed crosslinker) and 2% w/v CaCl_2 (rapid crosslinker) should be made the morning of the activity and can be mixed using tap water. It is recommended to make 500 mL of CaSO_4 and 1 L of CaCl_2 , as the CaCl_2 will typically need changing after 2 or 3 uses.

Performing the Activity

The class was allowed to form their own groups of 2 or 3 and then shown a demo of how to properly draw up alginate solutions in a syringe, remove air bubbles, and mix solutions before rapidly injecting them into the molds. It is critical to start with the injection mold as this will take 20 minutes to gel even while soaking in the rapid CaCl_2 crosslinker. Following injection into the molds, students were then instructed to make an alginate sheet followed by an alginate cylinder. The alginate cylinders should be made using 6 mL of alginate and 3 ml of CaSO_4 that has been mixed 4 times and rapidly injected into the conical tube. After injecting the alginate

into the tube, a few mL of CaCl_2 should be added to the top then let it sit for 7-10 minutes.

After allowing the alginate sheet to gel for 5 minutes, students can biopsy alginate discs and observe how the discs become stiffer when exposed to a secondary crosslinker, CaCl_2 . They can also observe the viscoelastic behavior with the large alginate cylinder and injection molded meniscus as they squeeze and release it gently allowing water to leave and slowly re-enter the structure as it returns to its original shape.

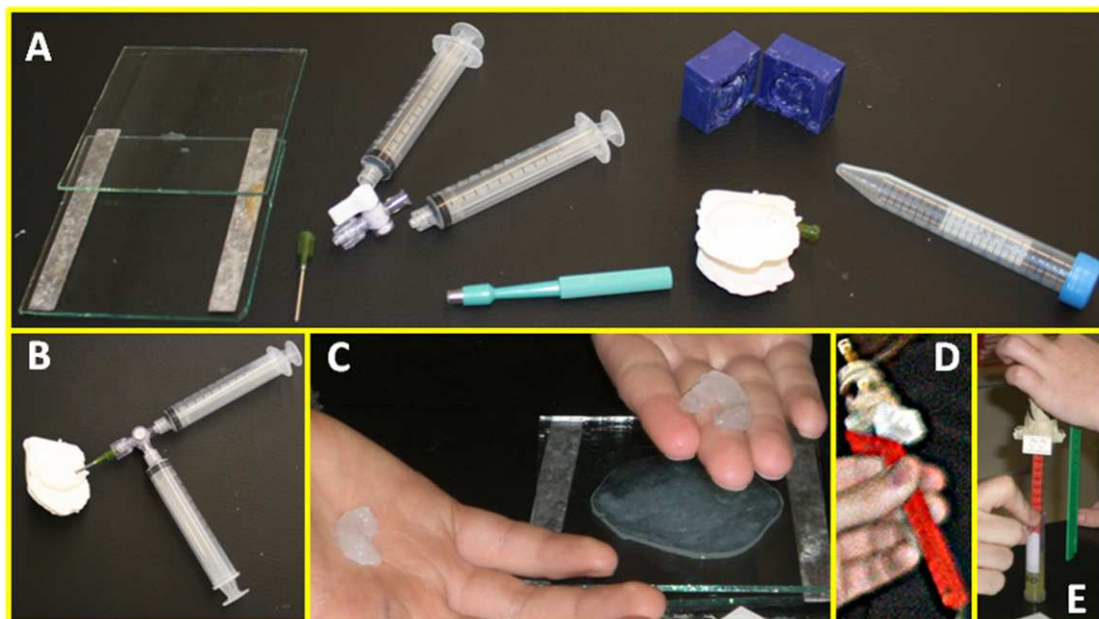


Figure 8.4: (A) Layout of materials used for alginate activities which include (starting from the left) glass plates with 1mm thick aluminum spacers, syringe tip, 3-way stopcock, 2 syringes, green biopsy punch, white silastic mold, blue ABS plastic mold, and 15 mL conical tube. (B) Assembled injection molding system. (C) Successfully molded menisci held by student and alginate sheet. Loading device (D) and a successfully loaded alginate gel in conical tube (E).

8.6 Alginate Activity #2

Materials and Teacher Preparation

For activity #2 preparations are the same, note the additional alginate solutions that need to be prepped the night before, new crosslinker solutions to be made the morning of the activity, and the updated list of materials in Fig. 8.5. Groups will be given three 15 mL conical tubes, an additional 15 mL conical tube with the bottom end sawed off, as well as a set of small weights (ranging from 5 – 100 g) that can fit through the open end of the conical tube or a different loading system such as the one we designed for the class (Fig. 8.5). Food coloring should be used for the different alginate concentrations to help distinguish between different alginate concentrations. The objective of the second activity is for students to find a formulation (with any mixture of alginate concentration and crosslinker) that produces the strongest gel and to develop a method of characterizing how much stronger it is from other gels (using weights or loading system).

Performing the Activity

A demonstration of the compression test was done using an alginate cylinder made in Activity 1 with a conical tube. Compression tests were performed with the loader designed by the authors (Fig. 8.4D). The loader consisted of a long lego block (sized to fit in the tube) with a weight fixed on the end totaling 86 g (Fig. 8.4D-E). Students cut the ends of the gel so that they were parallel. The gel was then placed in the cut tube, held so that the top of the tube was firmly against the table, and the height of the gel was measured. The loader was then gently placed on the gel through the sawed off end and students measured how much the gel compressed (change in height) or recorded the test as a failure if the gel could not support the load (Fig. 8.4E).

Students could then use these measurements to calculate stress and strain using the formulas provided (Fig. 8.5).

For students having difficulty getting started, it was helpful to have them select their favorite color of alginate. Once the first choice was made the students were motivated to try new combinations, regardless of whether the gel failed or not. It is important to be conscious of time since almost every group did not want to stop testing new combinations. The goal was to have each group make 3 gels with at least one successful load test.

8.7 Results

Class Performance

Students reacted very positively to all parts of the lesson plan, even the introductory lecture where specific comments were made about how much they liked seeing pictures of current research and learning about the money involved in healthcare costs (Fig. 8.7). Most students were able to make intact menisci gels from the first activity as well as observe the change in stiffness when exposing alginate to CaCl_2 (Fig. 8.4C). All but one group generated an alginate cylinder that could pass the loading test. None of the students performed the strain calculations, but approximately half of the groups did do comparisons between the different alginate cylinder displacements. Other hydrogel observations included comments on the clarity, consistency, and stiffness to the touch.

Day 3

Alginate Characterization!!!!

Supplies for each desk:

3 intact 15 mL conical tubes
1 open ended 15 mL conical tube
1 set of weights (5 - 100 g)
1 beaker with 25 mL 1% (w/v) Alginate (Red)
1 beaker with 25 mL 2% (w/v) Alginate (Blue)
1 beaker with 25 mL 3% (w/v) Alginate (Yellow)
1 beaker with 25 mL 0.75% (w/v) CaSO₄
1 beaker with 25 mL 2% (w/v) CaSO₄
1 beaker with 50 mL 1% (w/v) CaCl₂
1 beaker with 50 mL 2% (w/v) CaCl₂
1 beaker with 50 mL tap water
4 10 mL syringes
2 3-way stopcocks
2 mini spatulas
1 ruler or micrometer

Goal: Today you will be trying to make an optimal strong alginate gel. With the items given you must try to make 3 different kinds of gels and devise a way to characterize them to determine which is the strongest/best and why. HAVE FUN!!!!

Some useful information that might help you:

Area of conical tube = 0.000163 m²

Acceleration = 10 m/s/s

$$Force = mass \times acceleration$$

$$Stress = \frac{Force}{Area}$$

$$Strain = \frac{OriginalHeight - NewHeight}{OriginalHeight}$$

Figure 8.5: Student Material List and Directions for Activity #2.

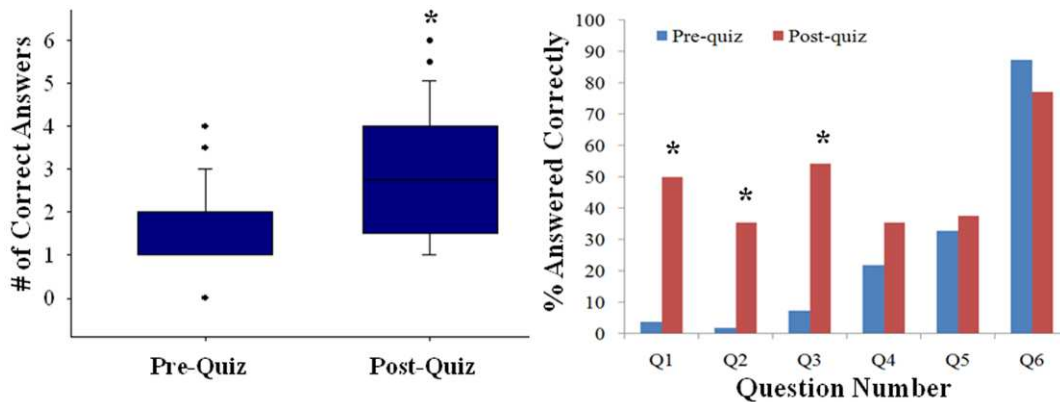


Figure 8.6: Student Pre- and Post-Quiz performance showing a significant increase in the number of correct answers (Left plot) after the lesson which was due to improved answers to the first 3 questions (Right plot). A “●” denotes an outlier and a “*” denotes statistical significance $P < 0.001$.

Before administering the first part of the lesson plan, students were given a Pre-Quiz (Fig. 8.2) and then given the same quiz for post-lesson analysis the week following the lesson plan. The results show that class performance on the quiz was significantly improved ($P < 0.001$) after the 3 day lesson (Fig. 8.6). Students were able to articulate what tissue engineering was (Fig. 8.6Q1) and define what a biomaterial was (Fig. 8.6Q2) ($P < 0.001$ for both). Students were also able to visualize the concept of stress (Fig. 8.6Q3) after the lesson ($P < 0.001$), but were not able to relate to stress or force mathematically in questions 4 and 5. Stress and strain are advanced topics not normally introduced in middle school level and could be too complex for students not in advanced math. The last question (stress-strain plot of a viscoelastic material) had no significant change in performance ($P = 0.272$) as almost 90% students guessed the correct answer before the class and continued to select the correct answer after the lesson. Overall test scores were compared using the Mann-Whitney Rank Sum Test

and individual question performance was compared using a z-test in SigmaStat v3.5 (Systat Software, Inc.; San Jose, CA).

Student Praise for Alginate Activities

Students were also asked to write on the back of the Post-Quiz comments about what they thought about the curriculum they had experienced the week before. All but one student wrote positive comments most of which expressed their enjoyment in being allowed to select their own groups, very much liked the hands aspect of the activity, enjoyed making something new, and liked playing with the “gooey” gels and making a mess. Some comments we would like to highlight include:

- It was fun because we actually got to make a meniscus.
- It was fun to interact with different items around our environment that we usually don't have direct contact with. It was a fun experiment that was rare and rewarding.
- We actually got to make the things ourselves, instead of just watching. Also it was fun to see how to make stuff that is so important to the human body.
- I liked that we are doing stuff that people in Cornell choose to take a profession in that can make major advancements in daily life.

Figure 8.7: Student praise for alginate activities.

8.8 Concluding Remarks

This lesson will introduce an appreciation for the field of tissue engineering as well as provide hands on knowledge of principles behind tissue engineering which include: biomaterials, stresses, strains, and viscoelastic materials in our body. Students will learn that science is an explorative process and gain respect for university research (Fig. 8.7).

APPENDIX A

SUPPLEMENTARY DATA AND MATLAB CODE FOR SHAPE FIDELITY DATA ANALYSIS

Despite the difference in resolution between MRI, μ CT, and a laser scan it became obvious that the different imaging modalities had various draw backs when compared directly (Fig. A.1). MRI was a lower resolution scan of a loaded tissue still inside the joint, while the μ CT scan of the exact same meniscus was a higher resolution image of excised tissue that was allowed to soak in a contrast agent. Lastly, the laser scan was of medium resolution compared to MRI and μ CT, but a topological scan that resulted in obvious projection of overhanging surfaces (Fig. A.1). It was determined that laser scans of engineered tissue would be compared to laser scans of native tissue to maintain consistency and in essence normalize for projected surfaces.

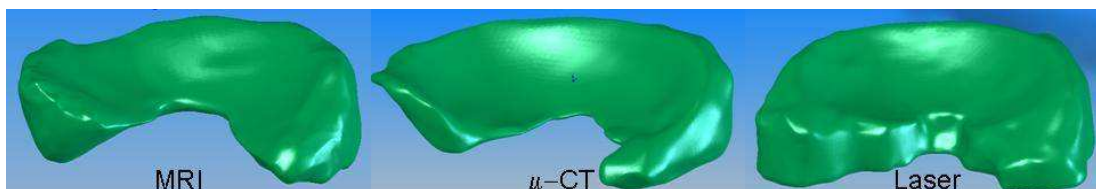


Figure A.1: Comparative MRI, μ CT, and laser scan of the same ovine meniscus.

To generate the frequency histograms of the deviation heat map data seen in figures 4.3 and D.2 the Matlab code below normalized the deviation points to a characteristic height length for that particular ovine meniscus and binned them in 5% error bar increments. This code was written by Dan Cohen and Jeff Ballyns utilizing two components, the “main.m” file and the “histomaker.m” function.

Main.m Matlabe Code:

```
%%%%%%%% CHANGE BELOW %%%%
Vzref = -4437;
Vinc = 296;
%%%%%%%% CHANGE ABOVE %%%%

cd data
%%%%%%%% CHANGE BELOW %%%%
cd S7
%%%%%%%% CHANGE ABOVE %%%%
cd CTM

x = dir;
no_files = size(x);
for i= 3: no_files(1,1)
    ystr = x(i).name
    dataStruct = importdata(ystr);
    currentData = zeros(length(dataStruct.data),12);
    currentData = dataStruct.data;
    cd ..
    [H1,H2,H3,PlusMinus10] = histoMaker(currentData,Vzref,Vinc,ystr);
    cd CTM
    CTMoutput{i-2,1}=H1;
    CTMoutput{i-2,2}=H2;
    CTMoutput{i-2,3}=H3;
    CTMoutput{i-2,4}=PlusMinus10;
end

cd ..
cd CTP

x = dir;
no_files = size(x);
for i= 3: no_files(1,1)
    ystr = x(i).name
    dataStruct = importdata(ystr);
    currentData = zeros(length(dataStruct.data),12);
    currentData = dataStruct.data;
    cd ..
    [H1,H2,H3,PlusMinus10] = histoMaker(currentData,Vzref,Vinc,ystr);
    cd CTP
    CTPoutput{i-2,1}=H1;
    CTPoutput{i-2,2}=H2;
```

```

    CTPoutput{i-2,3}=H3;
    CTPoutput{i-2,4}=PlusMinus10;
end

cd ..
cd MRM

x = dir;
no_files = size(x);
for i= 3: no_files(1,1)
    ystr = x(i).name
    dataStruct = importdata(ystr);
    currentData = zeros(length(dataStruct.data),12);
    currentData = dataStruct.data;
    cd ..
    [H1,H2,H3,PlusMinus10] = histoMaker(currentData,Vzref,Vinc,ystr);
    cd MRM
    MRMoutput{i-2,1}=H1;
    MRMoutput{i-2,2}=H2;
    MRMoutput{i-2,3}=H3;
    MRMoutput{i-2,4}=PlusMinus10;
end

cd ..
cd MRP

x = dir;
no_files = size(x);
for i= 3: no_files(1,1)
    ystr = x(i).name
    dataStruct = importdata(ystr);
    currentData = zeros(length(dataStruct.data),12);
    currentData = dataStruct.data;
    cd ..
    [H1,H2,H3,PlusMinus10] = histoMaker(currentData,Vzref,Vinc,ystr);
    cd MRP
    MRPoutput{i-2,1}=H1;
    MRPoutput{i-2,2}=H2;
    MRPoutput{i-2,3}=H3;
    MRPoutput{i-2,4}=PlusMinus10;
end

cd ..
cd SIL

```

```

x = dir;
no_files = size(x);
for i= 3: no_files(1,1)
    ystr = x(i).name
    dataStruct = importdata(ystr);
    currentData = zeros(length(dataStruct.data),12);
    currentData = dataStruct.data;
    cd ..
    [H1,H2,H3,PlusMinus10] = histoMaker(currentData,Vzref,Vinc,ystr);
    cd SIL
    SILoutput{i-2,1}=H1;
    SILoutput{i-2,2}=H2;
    SILoutput{i-2,3}=H3;
    SILoutput{i-2,4}=PlusMinus10;
end

cd ..

save CTM_output CTMoutput -MAT
save CTP_output CTPoutput -MAT
save MRM_output MRMoutput -MAT
save MRP_output MRPoutput -MAT
save SIL_output SILoutput -MAT
hnEdges = 14;
CTMsum =
CTMoutput{1,1}+CTMoutput{2,1}+CTMoutput{3,1}+CTMoutput{4,1}+CTMoutput
{5,1}+CTMoutput{6,1};
CTMcomp = CTMsum/6;
figure(11)
edges = (-(hnEdges*Vinc):Vinc:(hnEdges*Vinc));
bar(edges,CTMcomp);
CTPsum =
CTPoutput{1,1}+CTPoutput{2,1}+CTPoutput{3,1}+CTPoutput{4,1}+CTPoutput{5,1}
+CTPoutput{6,1};
CTPcomp = CTPsum/6;
figure(12)
edges = (-(hnEdges*Vinc):Vinc:(hnEdges*Vinc));
bar(edges,CTPcomp);
MRMsum =
MRMoutput{1,1}+MRMoutput{2,1}+MRMoutput{3,1}+MRMoutput{4,1}+MRMou
tput{5,1}+MRMoutput{6,1};
MRMcomp = MRMsum/6;
figure(13)
edges = (-(hnEdges*Vinc):Vinc:(hnEdges*Vinc));
bar(edges,MRMcomp);

```

```

MRPsum =
MRPoutput{1,1}+MRPoutput{2,1}+MRPoutput{3,1}+MRPoutput{4,1}+MRPoutput
{5,1}+MRPoutput{6,1};
MRPcomp = MRPsum/6;
figure(14)
edges = (-(hnEdges*Vinc):Vinc:(hnEdges*Vinc));
bar(edges,MRPcomp);
SILsum =
SILoutput{1,1}+SILoutput{2,1}+SILoutput{3,1}+SILoutput{4,1}+SILoutput{5,1}+S
ILoutput{6,1};
SILcomp = SILsum/6;
figure(15)
edges = (-(hnEdges*Vinc):Vinc:(hnEdges*Vinc));
bar(edges,SILcomp);

saveas(11,'TotalCTM.tiff');
saveas(12,'TotalCTP.tiff');
saveas(13,'TotalMRM.tiff');
saveas(14,'TotalMRP.tiff');
saveas(15,'TotalSIL.tiff');

```

Histomaker.m function Matlab code:

```

function [histo1,histo2,histo3,pm10] = histoMaker(origData,zref,inc,name)

%%%%%%%%%% CHANGE VALUE %%%%%%%%%%%
hnEdges = 14;
%%%%%%%%%%

newData1 = zeros(length(origData),12);
% ZREF MUST BE NEGATIVE!
% zref = -0.357;
row1 = 1;
for i = 1:length(origData)
    if (origData(i,3)<=zref)
        % ignore the row's data
    else
        newData1(row1,1:10) = origData(i,:);
        newData1(row1,3) = newData1(row1,3) + abs(zref);
        newData1(row1,6) = newData1(row1,6) + abs(zref);
        newData1(row1,11) = newData1(row1,10)/newData1(row1,3)*100;
    end
end

```

```

        newData1(row1,12) = newData1(row1,9)/newData1(row1,3)*100;
        row1 = row1 + 1;
    end
end
endRow = row1 - 1;
newData2 = newData1(1:endRow,:);

% inc = 0.296;
edges = (-(hnEdges*inc):inc:(hnEdges*inc));
histo = histc(newData2(:,10),edges);
% histo_length = length(histo)
% edges_length = length(edges)
newHisto = histo/sum(histo)*100;
histo1 = newHisto;
figure(1)
bar(edges,newHisto)

%%%%%%%%%% CHANGE VALUE %%%%%%%%%%%
pm10 = newHisto(hnEdges-
1)+newHisto(hnEdges)+newHisto(hnEdges+1)+newHisto(hnEdges+2);
%%%%%%%%%%

edges = (-(200):5:(200));
histo = histc(newData2(:,11),edges);
% histo_length = length(histo)
% edges_length = length(edges)
newHisto = histo/sum(histo)*100;
histo2 = newHisto;
figure(2)
bar(edges,newHisto)

edges = (-(200):5:(200));
histo = histc(newData2(:,12),edges);
% histo_length = length(histo)
% edges_length = length(edges)
newHisto = histo/sum(histo)*100;
histo3 = newHisto;
figure(4)
bar(edges,newHisto)

str1 = strcat(name,'_1.tiff')
str2 = strcat(name,'_2.tiff')
str4 = strcat(name,'_4.tiff')
saveas(1,str1);
saveas(2,str2);

```

```

saveas(4,str4);

% hist(newData2(:,10),edges);
% figure(2)
% newData3 = [newData2(:,4) newData2(:,5) newData2(:,11)];
% plot3(newData2(:,4), newData2(:,5), newData2(:,11))

% newData3 = zeros(size(newData2));
% min1 = min(newData2(:,1));
% if min1<0
%     %
% else
%     min1 = 0;
% end
% min2 = min(newData2(:,2));
% if min2<0
%     %
% else
%     min2 = 0;
% end
% for i = 1:length(newData2)
%     newData3(i,:) = newData2(i,:);
%     newData3(i,1) = newData2(i,1) + abs(min1)+0.0000001;
%     newData3(i,4) = newData2(i,4) + abs(min1)+0.0000001;
%     newData3(i,2) = newData2(i,2) + abs(min2)+0.0000001;
%     newData3(i,5) = newData2(i,5) + abs(min2)+0.0000001;
% end
% figure(3)
%
mesh(newData3(1:1000,1),newData3(1:1000,2),newData3(1:1000,3),newData3(1:1000,11))

```

APPENDIX B

SUPPLEMENTARY DATA FOR MEDIA MIXING STUDY (CHAPTER 6)

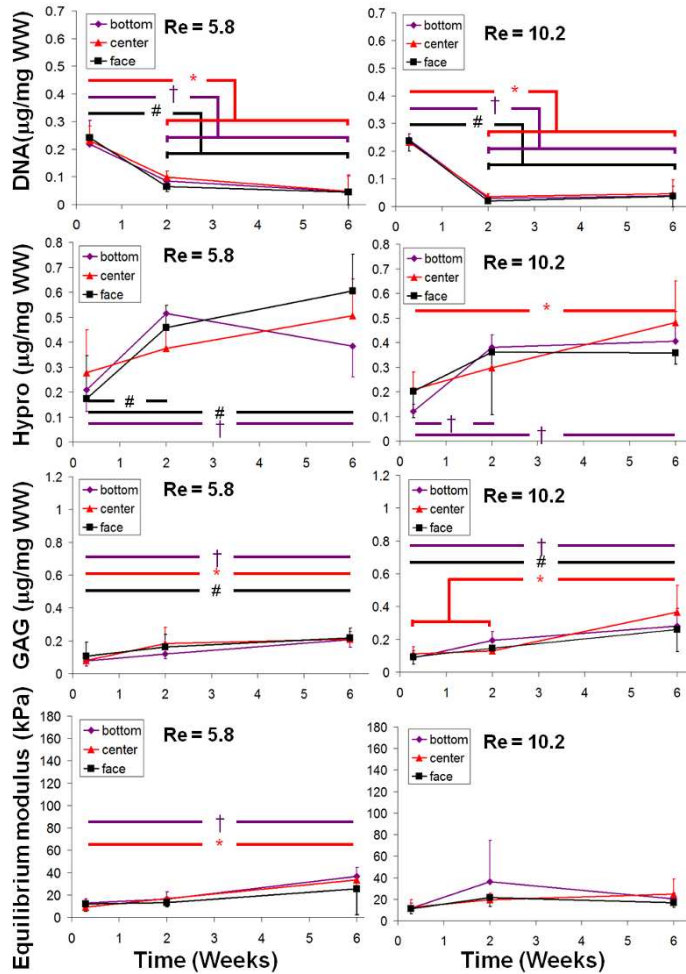


Figure B.1: Plots of DNA content (row 1), collagen content (row 2), and GAG content (row 3), looking at the individual spatial properties for Re 5.8 and Re 10.2. A “ \dagger ” denotes significant difference in the bottom location, a “ $*$ ” denotes a difference in the center location, a “ $\#$ ” denotes a difference in the face locations. Data represented as mean \pm SD and $P < 0.05$.

Due to space limitation not all the mixing media data was submitted for publication. Below are the mechanical and biochemical trends with time and location for Re 5.8 and Re 10.2. While there are temporal differences with regards to increases in ECM ($P < 0.05$) there are no differences with location in engineered menisci. Both mixing intensities show a similar decrease in DNA content across all locations with culture time ($P < 0.05$).

APPENDIX C

BIOREACTOR DESIGN MODIFICATIONS AND LABVIEW CODE

The original bioreactor design had a heating problem and would reach temperatures well above 45°C, which would kill cells. The bioreactor was also not capable of moving at frequencies other than 1Hz and could not generate an accurate sinusoidal curve. As a result the bioreactor underwent design alterations and programming changes to provide more accurate movements at an acceptable operating temperature of 37°C. The work was done along side Elysia Sheu.

The design alteration included addition of 4 heat sinks, 4 cooling fans, a ceramic insulator, and lowering the incubator temperature to 33°C (Fig. C.1). A load cell was also added onto the bioreactor so that compressive loads could be recorded during stimulations cycles.

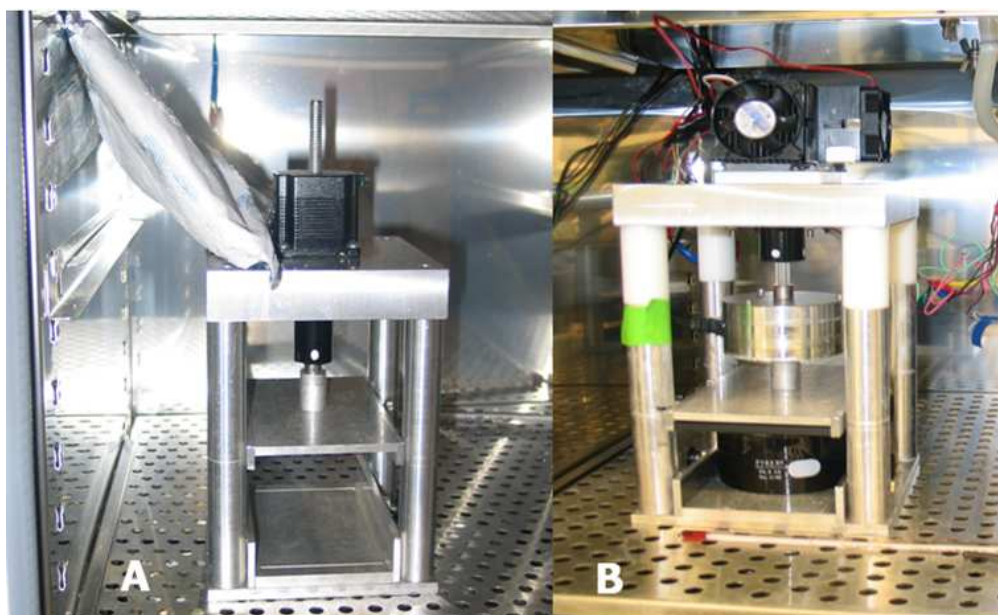


Figure C.1: Original bioreactor design with an ice pack (A) and retrofitted bioreactor (B) with heat sinks, cooling fans, and load cell.

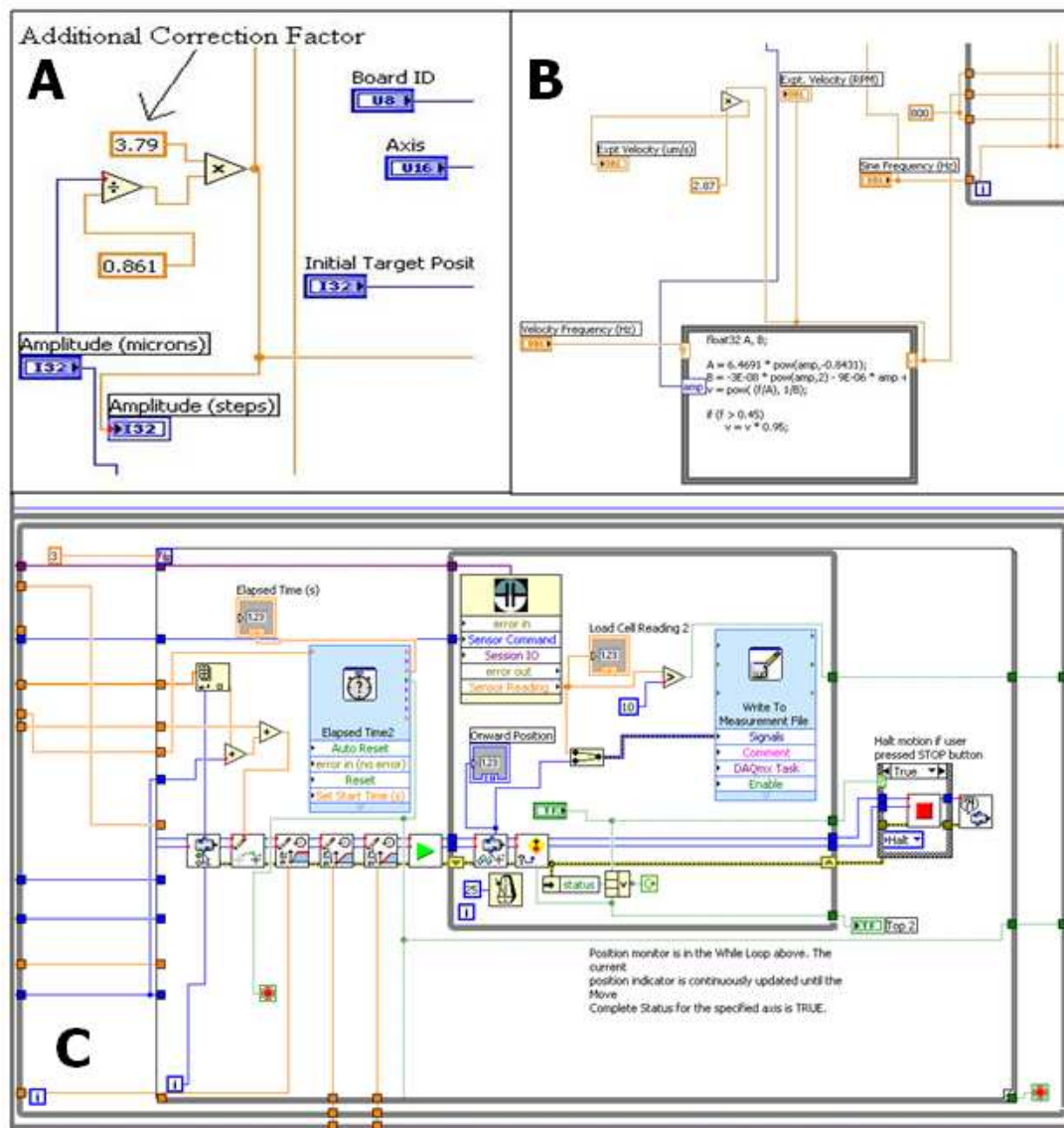


Figure C.2: Labview diagram for the bioreactor. (A) Amplitude correction factor for more accurate displacements. (B) New velocity frequency parameter to drive accurate sinusoidal movements. To move at a frequency of 1Hz, the velocity frequency = 4.5Hz. The maximum frequency can move = 1.25 Hz, with a velocity frequency of 4.75Hz. (C) Single step process of moving stepper motor and data acquisition.

APPENDIX D

SUPPLEMENTARY DATA AND MATLAB CODE USED FOR DYNAMIC LOADING DATA ANALYSIS

Due to space limitations some of the FE analysis, shape fidelity, biochemical, and mechanical data were not included in the manuscript submitted for publication. The results of the linear poroelastic FE model show similar normalized fluid velocity fields at maximum tissue compression, as expected. The direction of fluid flow as indicated by the arrow heads appears to be slightly random in the center of the construct and more radial towards the free edges of the tissue (Fig. D.1). Pressure gradient maps of the top and bottom surfaces of loaded menisci had very low value predictions ($\text{Pa/m} \times 10^{-110}$), indicating that fluid velocities are also quite low except for a few focal points on the pressure gradient maps (Fig. D.1). The differences between the location of peak pressure gradient and proportional fluid velocity values in 171 μm and 352 μm FE models, questions the validity of the fluid flow behavior in both models. It appears as though there may be a singularity happening in different locations for each model resulting in the different locations of peak velocity and pressure gradient values.

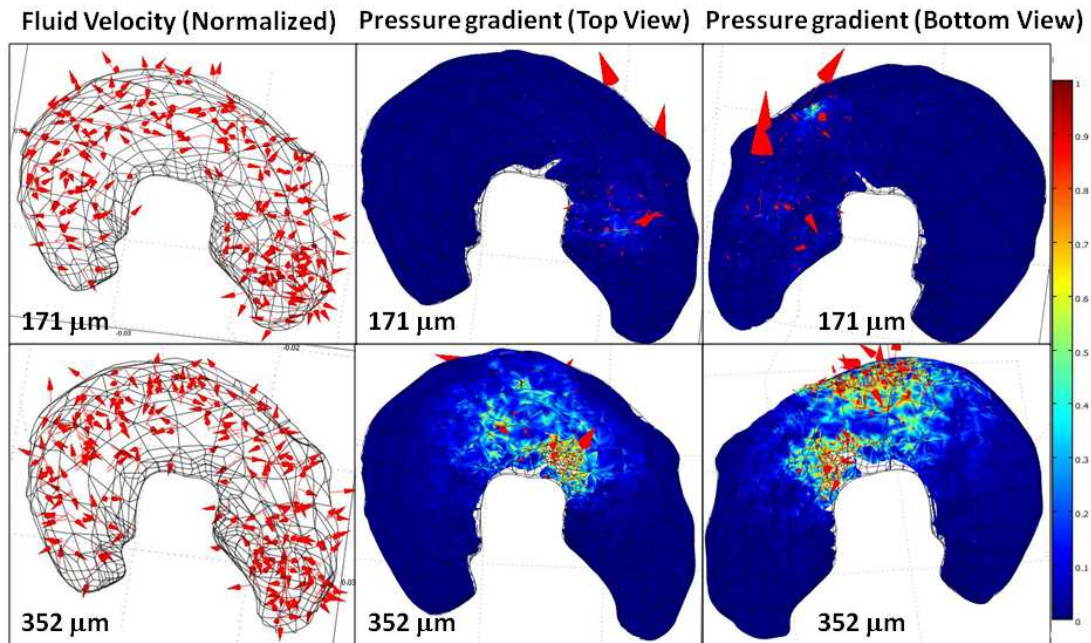


Figure D.1: Predicted fluid velocity directions (column 1) for dynamically loaded TE menisci at maximum compression. Top (column 2) and bottom (column 3) views of induced pressure gradient field ($\text{Pa/m} \times 10^{-110}$) at maximum compression along with a proportional fluid velocity field. Larger arrows denote higher fluid velocity.

Engineered constructs were analyzed for shape retention over culture time. It was observed that dynamic loading did not destructively alter overall shape fidelity as indicated by the lack of change in the deviation histogram profile with culture time (Fig. D.2). 171 μm construct did have slight decreases in volume and deviated more from target dimensions, but this change was likely due to handling error in between loading cycles.

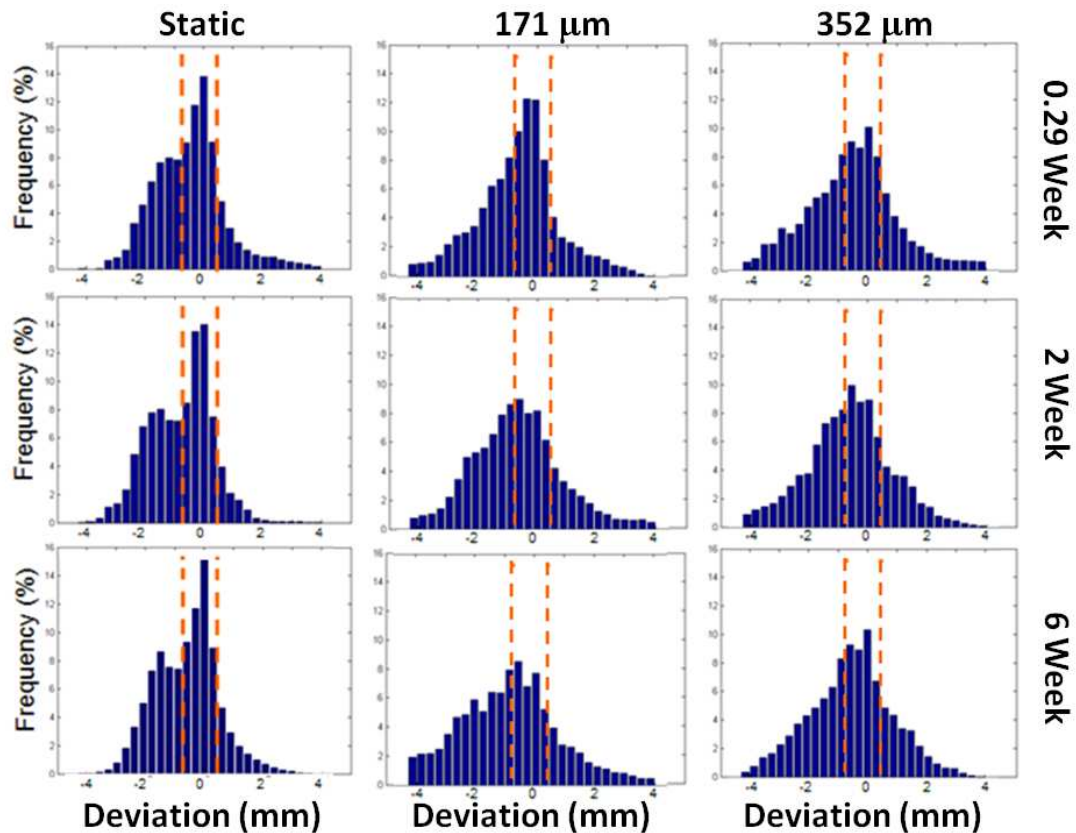


Figure D.2: Deviation histograms of static and dynamically loaded constructs and 0.29, 2 and 6 weeks.

Due to the observed decrease in compressive modulus from 2 to 6 weeks in 352 μm constructs, supplementary samples were cultured to determine if similar findings would be observed for the tensile properties. Despite the continued loading there was no difference between statically cultured and 352 μm samples (Fig. D.3). There was no increase in tensile properties even with an increase in collagen content in 352 μm samples (Fig. D.3). The lack of change in tensile properties is likely due to the absence of connected collagen network. This data suggests that dynamic compressive loading does not degrade alginate hydrogels as destructively in tension as higher media mixing intensities have shown to do in chapter 5.

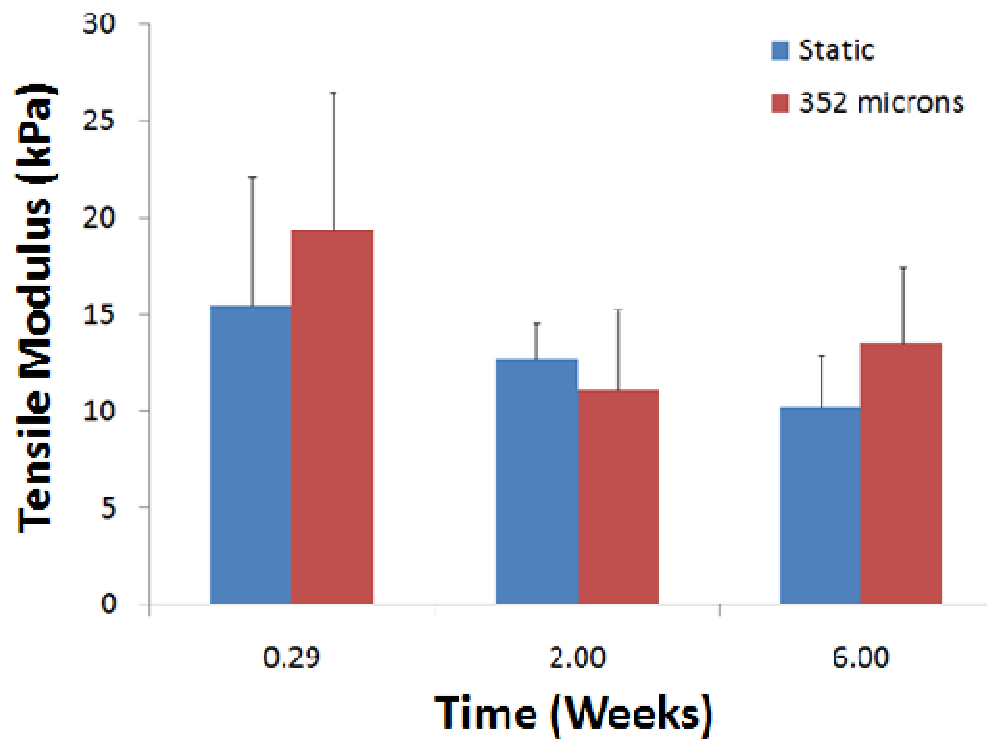


Figure D.3: Tensile modulus for static and 352 μm dynamically loaded constructs.

Lastly, DNA and ECM accumulation was analyzed based on location throughout these dynamically loaded constructs. It was found that no significant differences exist with location and that dynamic compressive loading resulted in uniform growth and loss of both DNA and ECM in these tissues (Fig. D.4).

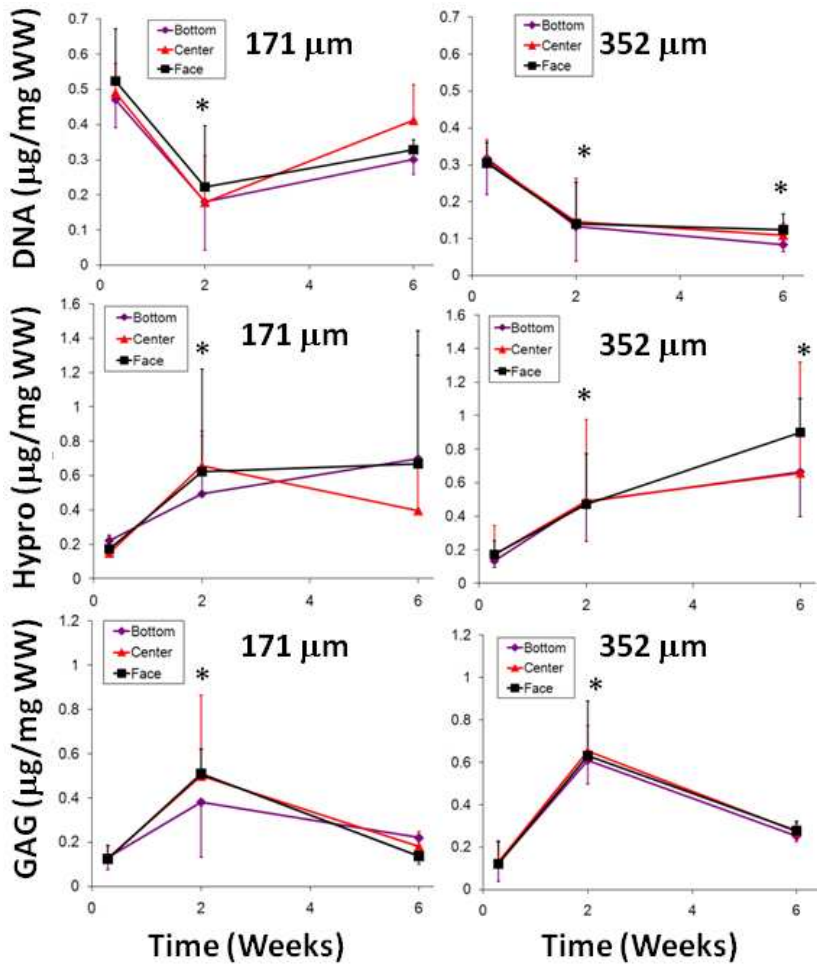


Figure D.4: DNA content and ECM accumulation at different locations throughout dynamically loaded TE menisci. “*” denotes significant difference compared to 0.29 weeks with $P < 0.05$.

Acquired load cell data from the bioreactor was filtered and analyzed using the Matlab script presented below. The code provided an average peak-to-peak load calculation at 5, 15, 30 and 45 minutes of each loading cycle to verify equilibrium. The code was written by John Nguyen, Jenny Puetzer, and Jeff Ballyns.

Pkpk.m file that calls on the peakfinder.m function in matlab:

```
% loading imported data from .lvm file
%load loaddata.mat

% assigning variables to columns
time = data(:,1);
lode = data(:,2);
motion = data(:,3);

figure(1)
plot(time,lode)
hold on

% red plot
[a,b] = butter(1,.1); %designs a order 1 lowpass butterworth filter
with normalized cutoff frequency of .1
smoothed = filtfilt(a,b,lode);
plot(time,smoothed,'r')

% green plot
[c,d] = butter(1,.4);
filtered = filtfilt(c,d,lode);
plot(time,filtered,'g')

% motion plot
plot(time,(motion-6446.5)./10000,'k')

%slope = diff(smoothed)./diff(time);

%set threshold value
n = .25;

%determins data at 5 mins
time_5= time>=300 & time<=360;
location_5 = find(time_5);
filtered_5 = filtered(location_5);
ftime_5 = time(location_5)

[peakLoc_5, peakMax_5] = peakfinder(filtered_5, n, 1);
plot(ftime_5(peakLoc_5), peakMax_5, 'k+')
[peakLoc2_5, peakMin_5] = peakfinder(filtered_5, n, -1);
plot(ftime_5(peakLoc2_5), peakMin_5, 'kd')

if (length(peakMax_5) ~= length(peakMin_5));
    if (length (peakMax_5)>length(peakMin_5));
        peakMax_5 = peakMax_5(1:length(peakMin_5));
    else
        peakMin_5 = peakMin_5(1:length(peakMax_5));
    end
end
end
```

```

%Length_max = length(peakMax_5)
%Lenght_min = length(peakMin_5)

Peak_Peak_5 = abs(peakMax_5 - peakMin_5)
Average_5 = mean(Peak_Peak_5)
Mode_5 = mode(Peak_Peak_5)

t_5 = ftime_5(peakLoc_5);
t_5 = t_5(1: length(Peak_Peak_5));

mean_max_5=mean(peakMax_5);
mean_min_5=mean(peakMin_5);
mode_max_5=mode(peakMax_5);
mode_min_5=mode(peakMin_5);
peak_peak_average_5=abs(mean_max_5-mean_min_5)
peak_peak_mode_5 =abs(mode_max_5-mode_min_5)

%determins data at 15 mins
time_15= time>=900 & time<=960;
location_15 = find(time_15);
filtered_15 = filtered(location_15);
ftime_15 = time(location_15);

[peakLoc_15, peakMax_15] = peakfinder(filtered_15, n, 1);
plot(ftime_15(peakLoc_15), peakMax_15, 'k+')
[peakLoc2_15, peakMin_15] = peakfinder(filtered_15, n, -1);
plot(ftime_15(peakLoc2_15), peakMin_15, 'kd')

if (length(peakMax_15) ~= length(peakMin_15));
    if (length (peakMax_15)>length(peakMin_15));
        peakMax_15 = peakMax_15(1:length(peakMin_15));
    else
        peakMin_15 = peakMin_15(1:length(peakMax_15));
    end
end

%Length_max = length(peakMax_15)
%Lenght_min = length(peakMin_15)

Peak_Peak_15 = abs(peakMax_15 - peakMin_15)
Average_15 = mean(Peak_Peak_15)
Mode_15 = mode(Peak_Peak_15)

t_15 = ftime_15(peakLoc_15);
t_15 = t_15(1: length(Peak_Peak_15));

mean_max_15=mean(peakMax_15);
mean_min_15=mean(peakMin_15);
mode_max_15=mode(peakMax_15);
mode_min_15=mode(peakMin_15);
peak_peak_average_15=abs(mean_max_15-mean_min_15)

```

```

peak_peak_mode_15 =abs(mode_max_15-mode_min_15)

%Determines data at 30 mins
time_30= time>=1800 & time<=1860;
location_30 = find(time_30);
filtered_30 = filtered(location_30);
ftime_30 = time(location_30);

[peakLoc_30, peakMax_30] = peakfinder(filtered_30, n, 1);
plot(ftime_30(peakLoc_30), peakMax_30, 'k+')
[peakLoc2_30, peakMin_30] = peakfinder(filtered_30, n, -1);
plot(ftime_30(peakLoc2_30), peakMin_30, 'kd')

if (length(peakMax_30) ~= length(peakMin_30));
    if (length (peakMax_30)>length(peakMin_30));
        peakMax_30 = peakMax_30(1:length(peakMin_30));
    else
        peakMin_30 = peakMin_30(1:length(peakMax_30));
    end
end

%Length_max = length(peakMax_30)
%Length_min = length(peakMin_30)

Peak_Peak_30 = abs(peakMax_30 - peakMin_30)
Average_30 = mean(Peak_Peak_30)
Mode_30 = mode(Peak_Peak_30)

t_30 = ftime_30(peakLoc_30);
t_30 = t_30(1: length(Peak_Peak_30));

mean_max_30=mean(peakMax_30);
mean_min_30=mean(peakMin_30);
mode_max_30=mode(peakMax_30);
mode_min_30=mode(peakMin_30);
peak_peak_average_30=abs(mean_max_30-mean_min_30)
peak_peak_mode_30 =abs(mode_max_30-mode_min_30)

%Determines data at 45 mins
time_45= time>=2700 & time<=2760;
location_45 = find(time_45);
filtered_45 = filtered(location_45);
ftime_45 = time(location_45);

[peakLoc_45, peakMax_45] = peakfinder(filtered_45, n, 1);
plot(ftime_45(peakLoc_45), peakMax_45, 'k+')
[peakLoc2_45, peakMin_45] = peakfinder(filtered_45, n, -1);
plot(ftime_45(peakLoc2_45), peakMin_45, 'kd')

if (length(peakMax_45) ~= length(peakMin_45));
    if (length (peakMax_45)>length(peakMin_45));
        peakMax_45 = peakMax_45(1:length(peakMin_45));
    else

```

```

        peakMin_45 = peakMin_45(1:length(peakMax_45));
    end
end

%Length_max = length(peakMax_45)
%Lenght_min = length(peakMin_45)

Peak_Peak_45 = abs(peakMax_45 - peakMin_45)
Average_45 = mean(Peak_Peak_45)
Mode_45 = mode(Peak_Peak_45)

t_45 = ftime_45(peakLoc_45);
t_45 = t_45(1: length(Peak_Peak_45));

mean_max_45=mean(peakMax_45);
mean_min_45=mean(peakMin_45);
mode_max_45=mode(peakMax_45);
mode_min_45=mode(peakMin_45);
peak_peak_average_45=abs(mean_max_45-mean_min_45)
peak_peak_mode_45 =abs(mode_max_45-mode_min_45)

%Analysis of all data at once
%[peakLoc, peakMax] = peakfinder(filtered, 1/4, 1);
%plot(time(peakLoc), peakMax, 'k+')
%[peakLoc2, peakMin] = peakfinder(filtered, 1/4, -1);
%plot(time(peakLoc2), peakMin, 'kd')
%mean_max=mean(peakMax)
%mean_min=mean(peakMin)
%mode_max=mode(peakMax)
%mode_min=mode(peakMin)
%length_max = length(peakMax);
%length_min = length(peakMin);
%sum_max = sum(peakMax);
%sum_min = sum(peakMin);
%average_max = sum_max / length_max;
%average_min = sum_min / length_min;
%peak_peak=abs(average_max-average_min)
%peak_peak_mode =abs(mode_max-mode_min)

hold off

figure(2)
subplot(2, 2, 1);
plot( t_5, Peak_Peak_5)
xlabel('Time(s)')
ylabel('Peak to Peak difference')
legend('5 mins')

subplot(2, 2, 2);
plot(t_15 , Peak_Peak_15)
xlabel('Time(s)')
ylabel('Peak to Peak difference')
legend('15 mins')

```

```

subplot(2,2, 3)
plot(t_30 , Peak_Peak_30)
xlabel('Time(s)')
ylabel('Peak to Peak difference')
legend('30 mins')

subplot(2, 2, 4)
plot(t_45 , Peak_Peak_45)
xlabel('Time(s)')
ylabel('Peak to Peak difference')
legend('45 mins')

% throwing out data

%set point for throwing out below
x = .2

%throw out data for 5 mins
ePk_Pk_5= Peak_Peak_5>=x;
elocation_5 = find(ePk_Pk_5);
ePeak_Peak_5 = Peak_Peak_5(elocation_5);
eftime_5 = t_5(elocation_5);

%throw out data for 15 mins
ePk_Pk_15= Peak_Peak_15>=x;
elocation_15 = find(ePk_Pk_15);
ePeak_Peak_15 = Peak_Peak_15(elocation_15);
eftime_15 = t_15(elocation_15);

%throw out data for 30 mins
ePk_Pk_30= Peak_Peak_30>=x;
elocation_30 = find(ePk_Pk_30);
ePeak_Peak_30 = Peak_Peak_30(elocation_30);
eftime_30 = t_30(elocation_30);

%throw out data for 45 mins
ePk_Pk_45= Peak_Peak_45>=x;
elocation_45 = find(ePk_Pk_45);
ePeak_Peak_45 = Peak_Peak_45(elocation_45);
eftime_45 = t_45(elocation_45);

%Graph new data
figure(3)
subplot(2, 2, 1);
plot( eftime_5, ePeak_Peak_5)
xlabel('Time(s)')
ylabel('Peak to Peak difference')
legend('5 mins')

subplot(2, 2, 2);
plot(eftime_15 , ePeak_Peak_15)

```

```
xlabel('Time(s)')
ylabel('Peak to Peak difference')
legend('15 mins')
```

```
subplot(2,2, 3)
plot(eftime_30 , ePeak_Peak_30)
xlabel('Time(s)')
ylabel('Peak to Peak difference')
legend('30 mins')
```

```
subplot(2, 2, 4)
plot(eftime_45 , ePeak_Peak_45)
xlabel('Time(s)')
ylabel('Peak to Peak difference')
legend('45 mins')
```

APPENDIX E

SUPPLEMENTARY DATA FOR MODELING THE DYNAMIC COMPOSITION OF ENGINEERED MENISCI AND EQUILIBRIUM COMPRESSIVE MODULUS USING THE RULE OF MIXTURES

It is well established that the mechanical properties of articular and fibrocartilage are a result of the composition and organization of the ECM. Primarily, the compressive properties of articular cartilage are a result of the GAG content and tensile properties and are heavily dependent on the collagen content and fiber orientation. This dissertation has demonstrated that mechanical stimulation via media mixing and dynamic compression can 1) enhance ECM accumulation in tissue engineered menisci and 2) improve the compressive equilibrium modulus. In addition, this research has shown that higher mixing intensities can have a detrimental effect on compressive properties by increasing the rate of scaffold degradation (Fig. E.1A). Under dynamic compression loading, it was observed that prolonged loading resulted in decreased GAG content in engineered menisci. This resulted in a lower compressive modulus. However, the findings of this dissertation also suggest that the compressive equilibrium modulus can increase with mechanical stimulation when GAG content does not differ from statically cultured controls, but collagen content does. The change in compressive modulus suggests that the collagen matrix accumulated in these engineered menisci does contribute to the compressive properties.

To model the influence of each component that contributes to the overall compressive equilibrium modulus of these tissue engineered constructs, the rule of mixtures was applied. This rule is represented

by: $E(t) = E_{Alg}[Alg](t) + E_{GAG}[GAG](t) + E_{Col}[Col](t)$, where E_{Alg} is the modulus constant for alginate, E_{GAG} is the modulus constant for GAG, E_{Col} is the modulus constant for collagen, $[Alg](t)$ is the amount of alginate in the construct as a function of time, $[GAG](t)$ is the concentration of GAG as a function of time, and $[Col](t)$ is the concentration of collagen in the construct as a function of time. The alginate, GAG, and collagen concentrations can be described by the following nonlinear decay and growth equations:

$$[Alg](t) = [Alg]_o e^{\frac{-t}{\tau_{Alg}}}$$

$$[GAG](t) = [GAG]_{SS} (1 - e^{\frac{-t}{\tau_{GAG}}})$$

$$[Col](t) = [Col]_{SS} (1 - e^{\frac{-t}{\tau_{Col}}})$$

Where $[Alg]_o$ is the initial alginate mass in

grams, $[GAG]_{SS}$ and $[Col]_{SS}$ are the steady state GAG and collagen concentrations in $\mu\text{g}/\text{mg}$ WW, and τ_{Alg} , τ_{GAG} , and τ_{Col} are the time constants in weeks (wks) for alginate, GAG, and collagen respectively. The exponential growth and decay equations are based on work by Wilson et al. that modeled the dynamic composition of engineered cartilage to find steady state values in tissue engineered constructs [172]. The time constants and steady state values (Table E.1) were calculated by fitting the nonlinear model equations for each culture condition which included static, Re 2.9, Re 21.8 and the 352 microns loading condition. Since alginate degradation rate data only existed for static, Re 5.8 and Re 21.8 culture conditions, the alginate scaffold degradation curve was interpolated between the static and Re 5.8 (Fig. E.1A). It was also assumed that the alginate degradation rate for the 352 microns loading condition was similar to that of Re 2.9.

Table E.1: Constants for initial alginate mass, time constants and steady state GAG and collagen concentrations for different culturing conditions based on model fits to measured biochemical data.

Culture Condition	$[Alg]_0$	$[GAG]_{ss}$	$[Col]_{ss}$	τ_{Alg}	τ_{GAG}	τ_{Col}
Static	11.16 g	0.28 $\mu\text{g}/\text{mg WW}$	0.32 $\mu\text{g}/\text{mg WW}$	5.50 wks	1.73 wks	3.03 wks
Re 2.9	11.16 g	0.25 $\mu\text{g}/\text{mg WW}$	0.52 $\mu\text{g}/\text{mg WW}$	4.98 wks	1.77 wks	1.36 wks
Re 5.8	11.16 g	NA	NA	4.03 wks	NA	NA
Re 21.8	11.16 g	77.1 $\mu\text{g}/\text{mg WW}$	0.09 $\mu\text{g}/\text{mg WW}$	2.69 wks	1000 wks	0.21 wks
352 microns	11.16 g	0.44 $\mu\text{g}/\text{mg WW}$	0.76 $\mu\text{g}/\text{mg WW}$	4.98 wks	0.53 wks	1.89 wks

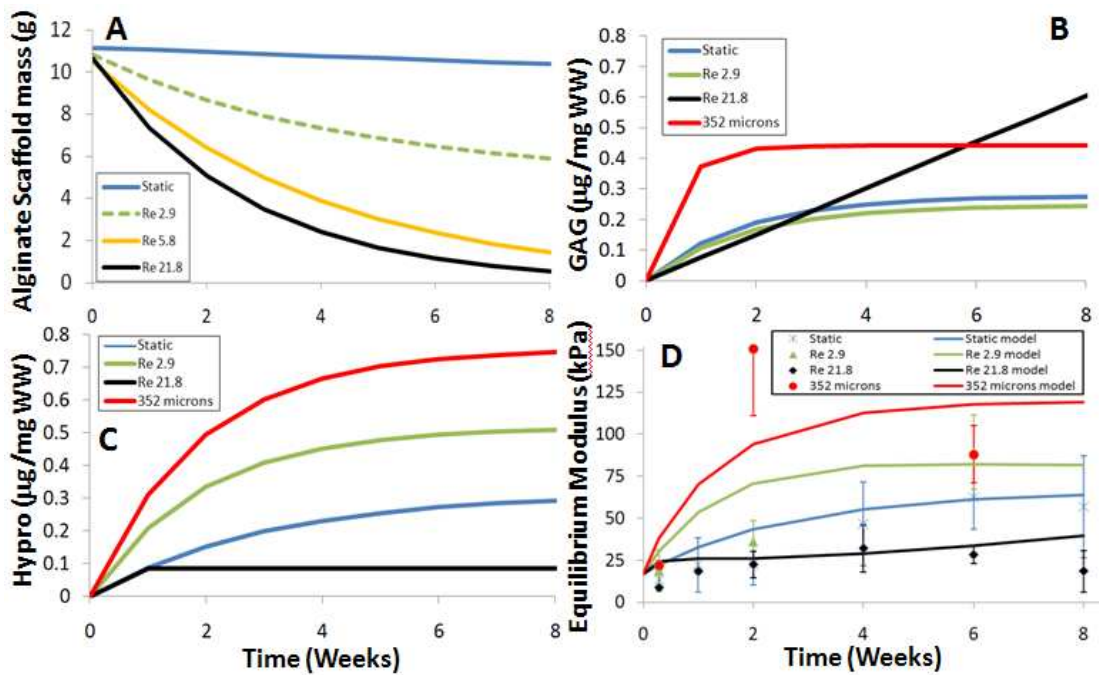


Figure E.1: (A) Alginde scaffold mass degradation model fit. (B) GAG and (C) hydroxyprolein (hypro) accumulation model fits for engineered constructs. (D) Equilibrium compressive model and measured data points for different culture conditions.

The model fits for alginate mass loss over time (Fig. E.1A) exemplifies how the application of media mixing can greatly increase the degradation rate of the alginate scaffold. The large decrease in alginate mass can explain the low compressive properties in samples exposed to Re 5.8 or higher. The model fits for collagen content

in engineered menisci showed that collagen accumulation was greatly amplified at lower mixing intensities such as Re 2.9 and the 352 microns compression condition (Fig. E.1C), but was not the case for GAG accumulation in Re 2.9 samples (Fig. E.1B).

The model fits were entered into the compressive modulus equation, $E(t)$, for each respective culture condition. The constants E_{Alg} , E_{GAG} , and E_{Col} were found by fitting the model to the static free-swell culture condition. This resulted in the constants of 1.5 kPa/g, 45 kPa, and 130 kPa for E_{Alg} , E_{GAG} , and E_{Col} respectively. These values were then used to model $E(t)$ for the Re 2.9, Re 21.8 and 352 microns culture conditions (Fig. E.1D). Surprisingly, these models show that collagen greatly contributes to the compressive properties in tissue engineered constructs, as indicated by the higher compressive modulus in Re 2.9 group compared to static controls which have similar GAG content. The most interesting model was the Re 21.8 culture condition, which showed an initial increase, followed by a slight decrease, and finally increased again as GAG accumulation became the dominating factor (Fig. E.1D).

The model estimations accurately predict the compressive properties at longer time points (i.e. 6 and 8 weeks). By modeling the compressive equilibrium modulus as a rule of mixtures system, we have learned that scaffold integrity plays a larger role in overall mechanical properties of engineered menisci than previously thought. As the scaffold breaks down, not only are more cells and ECM components lost to the media, but the ability to provide resistance in compression is also negated to a much greater degree than can be predicted with the rule of mixtures model presented here.

Modeling the modulus as a rule of mixtures in this dissertation has also brought to light the significant role collagen can play in compression. Evidence had previously suggested, based on theories describing articular cartilage, that GAG content was the highest contributor to compressive modulus. However, in the

meniscus, GAG makes up only 2 - 3% of the dry weight matrix [8, 9] which is 5 times below what is found in articular cartilage [173]. The meniscus has a compressive modulus that is $\frac{1}{2}$ that of articular cartilage [9, 173] meaning the collagen matrix must provide compressive support and does not follow the same behavior as would otherwise be observed in articular cartilage. The E(t) model demonstrates that collagen plays a crucial role in compressive properties and can enhance modulus when coupled with a stable scaffold and/or enhanced GAG accumulation.

APPENDIX F

PILOT DYNAMIC COMPRESSION LOADING EXPERIMENTS OF TISSUE ENGINEERED ARTICULAR CARTILAGE PLUGS

Upon completing the design, fabrication, and installation of the bioreactor into the incubator, pilot studies were conducted to replicate previous findings in the literature. The literature found that dynamic compression increases GAG accumulation in engineered cartilage [39]. Engineered plugs were generated by isolating articular chondrocytes from the femoral condyles and the patella-femoral groove of freshly slaughtered 1-3 day old calves. Cells were seeded into 2% w/v low viscosity alginate at a concentration of 50×10^6 cells/mL. The alginate cell suspension was then crosslinked with 2% w/v CaSO_4 then pressed between two plates of glass with 1mm spacers between them and allowed to gel for 5 minutes. 6mm diameter by 1mm thick plugs were biopsied from the alginate sheet. For each pilot study there was a control and loaded group that consisted of 24 plugs each, with 8 plugs allotted for each culture time point.

The first pilot study dynamically compressed plugs using a sinusoidal waveform at 1 Hz with an offset of 5% strain and amplitude of 5% resulting in a maximum compression of 10% strain. Samples were loaded for 1 hour everyday for up to 2 weeks. The second pilot study loaded plugs the same way except the waveform had an offset of 2.5% compressive strain and amplitude of 2.5% with a maximum compression of 5% strain. The third and final pilot study was carried out exactly the same as the second pilot study except that an ice pack was rested against the stepper motor to prevent the bioreactor test frame from reaching temperatures above 37°C. For all pilot studies static controls were statically loaded to 0% compressive strain in the bioreactor for 1 hour every day.

Upon removal from culture engineered plugs were analyzed biochemically for DNA content and GAG content via the Hoechst dye assay and the DMMB dye assay respectively. For the third pilot study collagen content was also analyzed via DMAB dye assay.

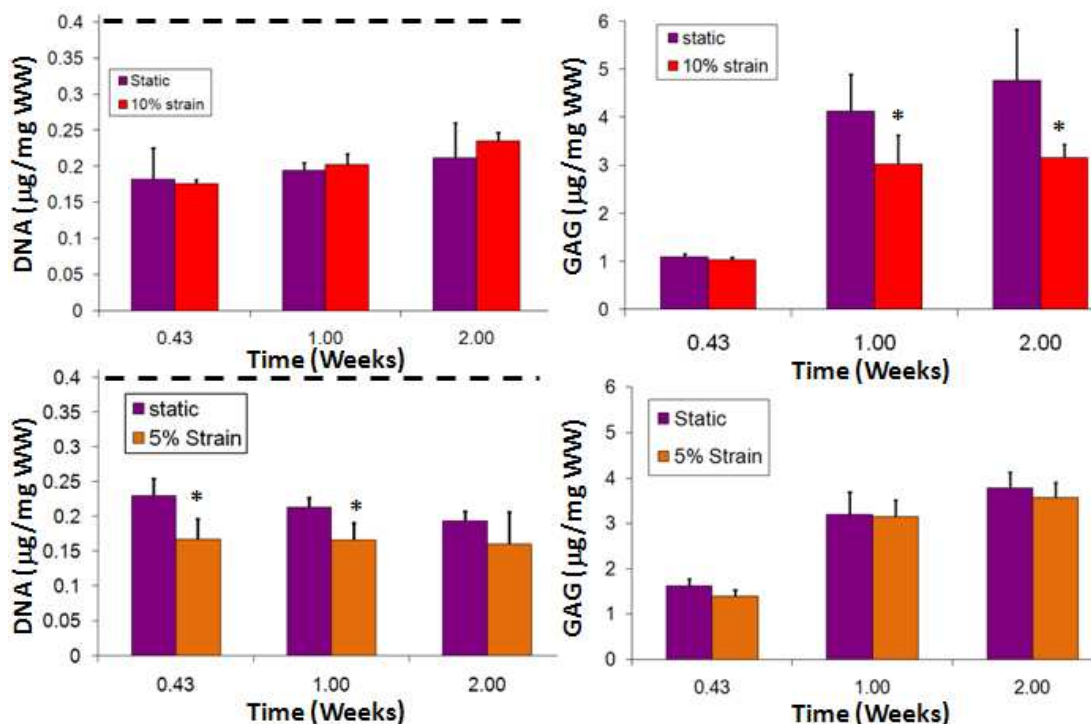


Figure F.1: DNA and GAG content for the first (Top, 10% strain) and second (Bottom, 5% strain) pilot studies. Dotted line denotes target DNA content for constructs. “*” denote significance compared to static controls $P < 0.05$.

The first pilot study resulted in lower DNA content in both static and loaded constructs compared to the initial target cell seeding density (Fig. F.1). 10% compressive strain also resulted in significantly lower GAG content in engineered plugs compared to static controls at 1 and 2 weeks ($P < 0.05$). Due to the lower GAG content we thought dynamically compressed plugs were being overloaded and decided to decrease the maximum strain engineered plugs were exposed to.

The second pilot study again resulted in lower DNA content in both static and loaded constructs compared to the initial target cell seeding density. However, in the

second study loaded constructs had significantly lower DNA content than static controls at 0.43 and 1 week ($P < 0.05$). No differences in GAG content were observed (Fig. F.1). The results of the second study lead us to believe that maybe the bioreactor was operating at too high a temperature and killing cells as a result. Measurements of the test frame operating temperature yielded a temperature of 43°C , confirming suspicions.

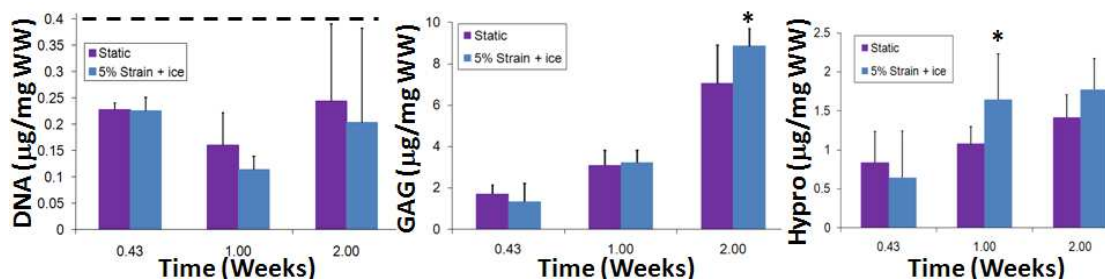


Figure F.2: DNA, GAG, and hydroxyproline content for the third pilot study. Dotted line denotes target DNA content for constructs. “*” denote significance compared to static controls $P < 0.05$.

The third pilot study implemented an ice pack to cool the test frame so that it would operate at the desired temperature of 37°C . The results of the 3rd study also had DNA content values that were below the target cell seeding density, but there were no statistical difference between static and loaded constructs. At 2 weeks more GAG accumulated in loaded constructs compared to static controls ($P < 0.05$) (Fig. F.2). There was also more collagen in loaded constructs at 1 week compared to static controls ($P < 0.05$) (Fig. F.2).

The findings of the three pilot studies show that the in house designed bioreactor can replicate findings from the literature [39]. Allowing the bioreactor to operate at a lower temperature proved to be the major problem inhibiting cells from synthesizing more ECM in response to mechanical stimulation. Based on these findings a project was initiated to better control bioreactor temperature as explained in Appendix C.

REFERENCES

1. Koski JA, Ibarra C, Rodeo SA, Warren RF. Meniscal injury and repair: clinical status. *The Orthopedic clinics of North America* 2000;31:419-436.
2. Kocabey Y, Nyland J, Isbell WM, Caborn DN. Patient outcomes following T-Fix meniscal repair and a modifiable, progressive rehabilitation program, a retrospective study. *Archives of orthopaedic and trauma surgery* 2004;124:592-596.
3. Khetia EA, McKeon BP. Meniscal allografts: biomechanics and techniques. *Sports medicine and arthroscopy review* 2007;15:114-120.
4. Barrett GR, Richardson K, Koenig V. T-Fix endoscopic meniscal repair: technique and approach to different types of tears. *Arthroscopy* 1995;11:245-251.
5. Meakin JR, Shrive NG, Frank CB, Hart DA. Finite element analysis of the meniscus: the influence of geometry and material properties on its behaviour. *The Knee* 2003;10:33-41.
6. Alford JW, Cole BJ. Cartilage restoration, part 1: basic science, historical perspective, patient evaluation, and treatment options. *The American journal of sports medicine* 2005;33:295-306.
7. Sweigart MA, Athanasiou KA. Tensile and compressive properties of the medial rabbit meniscus. *Proceedings of the Institution of Mechanical Engineers* 2005;219:337-347.
8. Fithian DC, Kelly MA, Mow VC. Material properties and structure-function relationships in the menisci. *Clinical orthopaedics and related research* 1990;19-31.
9. Sweigart MA, Zhu CF, Burt DM, DeHoll PD, Agrawal CM, Clanton TO, et al. Intraspecies and interspecies comparison of the compressive properties of the medial meniscus. *Annals of biomedical engineering* 2004;32:1569-1579.

10. Proctor CS, Schmidt MB, Whipple RR, Kelly MA, Mow VC. Material properties of the normal medial bovine meniscus. *J Orthop Res* 1989;7:771-782.
11. Wisnewski PJ, Powers DL, Kennedy JM. Glutaraldehyde-cross-linked meniscal allografts: mechanical properties. *J Invest Surg* 1988;1:259-266.
12. Anderson DR, Gershuni DH, Nakhostine M, Danzig LA. The effects of non-weight-bearing and limited motion on the tensile properties of the meniscus. *Arthroscopy* 1993;9:440-445.
13. McNickle AG, Wang VM, Shewman EF, Cole BJ, Williams JM. Performance of a sterile meniscal allograft in an ovine model. *Clinical orthopaedics and related research* 2009;467:1868-1876.
14. ME´RIDA-VELASCO JA, SA´NCHEZ-MONTESINOS I, ESPI´N-FERRA JN, RODRI´GUEZ-VA´ZQUEZ JF, ME´RIDA-VELASCO JR, JIME´NEZ-COLLADO J. Development of the Human Knee Joint. *The Anatomical record* 1997;2:269-278.
15. Oransky M, Canero G, Maiotti M. Embryonic development of the posterolateral structures of the knee. *The Anatomical record* 1989;225:347-354.
16. Fukazawa I, Hatta T, Uchio Y, Otani H. Development of the meniscus of the knee joint in human fetuses. *Congenital anomalies* 2009;49:27-32.
17. Cui JH, Min BH. Collagenous fibril texture of the discoid lateral meniscus. *Arthroscopy* 2007;23:635-641.
18. Pena E, Calvo B, Martinez MA, Palanca D, Doblare M. Finite element analysis of the effect of meniscal tears and meniscectomies on human knee biomechanics. *Clinical biomechanics (Bristol, Avon)* 2005;20:498-507.
19. Vadher SP, Nayeb-Hashemi H, Canavan PK, Warner GM. Finite element modeling following partial meniscectomy: effect of various size of resection. *Conf Proc IEEE Eng Med Biol Soc* 2006;1:2098-2101.

20. Kessler MA, Glaser C, Tittel S, Reiser M, Imhoff AB. Volume changes in the menisci and articular cartilage of runners: an in vivo investigation based on 3-D magnetic resonance imaging. *The American journal of sports medicine* 2006;34:832-836.
21. Mastrokalos DS, Papagelopoulos PJ, Mavrogenis AF, Hantes ME, Paessler HH. Changes of the posterior meniscal horn height during loading: an in vivo magnetic resonance imaging study. *Orthopedics* 2008;31:68.
22. Farnig E, Sherman O. Meniscal repair devices: a clinical and biomechanical literature review. *Arthroscopy* 2004;20:273-286.
23. Peters G, Wirth CJ. The current state of meniscal allograft transplantation and replacement. *The Knee* 2003;10:19-31.
24. Dienst M, Greis PE, Ellis BJ, Bachus KN, Burks RT. Effect of lateral meniscal allograft sizing on contact mechanics of the lateral tibial plateau: an experimental study in human cadaveric knee joints. *The American journal of sports medicine* 2007;35:34-42.
25. Heijkants RG, van Calck RV, De Groot JH, Pennings AJ, Schouten AJ, van Tienen TG, et al. Design, synthesis and properties of a degradable polyurethane scaffold for meniscus regeneration. *Journal of materials science* 2004;15:423-427.
26. Kobayashi M. A study of polyvinyl alcohol-hydrogel (PVA-H) artificial meniscus in vivo. *Bio-medical materials and engineering* 2004;14:505-515.
27. Kang SW, Son SM, Lee JS, Lee ES, Lee KY, Park SG, et al. Regeneration of whole meniscus using meniscal cells and polymer scaffolds in a rabbit total meniscectomy model. *J Biomed Mater Res A* 2006;78:659-671.
28. Aufderheide AC, Athanasiou KA. Assessment of a bovine co-culture, scaffold-free method for growing meniscus-shaped constructs. *Tissue engineering* 2007;13:2195-2205.
29. Ballyns JJ, Gleghorn JP, Niebrzydowski V, Rawlinson JJ, Potter HG, Maher SA, et al. Image-guided tissue engineering of anatomically shaped implants via

- MRI and micro-CT using injection molding. *Tissue Eng Part A* 2008;14:1195-1202.
30. Baker BM, Mauck RL. The effect of nanofiber alignment on the maturation of engineered meniscus constructs. *Biomaterials* 2007;28:1967-1977.
 31. Aufderheide AC, Athanasiou KA. Comparison of scaffolds and culture conditions for tissue engineering of the knee meniscus. *Tissue engineering* 2005;11:1095-1104.
 32. Ballyns JJ, Bonassar LJ. Image-Guided Tissue Engineering. *Journal of cellular and molecular medicine* 2009;13:1428-1436.
 33. Gooch KJ, Kwon JH, Blunk T, Langer R, Freed LE, Vunjak-Novakovic G. Effects of mixing intensity on tissue-engineered cartilage. *Biotechnology and bioengineering* 2001;72:402-407.
 34. Marsano A, Wendt D, Raiteri R, Gottardi R, Stolz M, Wirz D, et al. Use of hydrodynamic forces to engineer cartilaginous tissues resembling the non-uniform structure and function of meniscus. *Biomaterials* 2006;27:5927-5934.
 35. Bueno EM, Bilgen B, Barabino GA. Wavy-walled bioreactor supports increased cell proliferation and matrix deposition in engineered cartilage constructs. *Tissue engineering* 2005;11:1699-1709.
 36. Bueno EM, Bilgen B, Barabino GA. Hydrodynamic parameters modulate biochemical, histological, and mechanical properties of engineered cartilage. *Tissue Eng Part A* 2009;15:773-785.
 37. Neves AA, Medcalf N, Brindle KM. Influence of stirring-induced mixing on cell proliferation and extracellular matrix deposition in meniscal cartilage constructs based on polyethylene terephthalate scaffolds. *Biomaterials* 2005;26:4828-4836.
 38. Marsano A, Vunjak-Novakovic G, Martin I. Towards tissue engineering of meniscus substitutes: selection of cell source and culture environment. *Conf Proc IEEE Eng Med Biol Soc* 2006;1:3656-3658.

39. Kisiday JD, Jin M, DiMicco MA, Kurz B, Grodzinsky AJ. Effects of dynamic compressive loading on chondrocyte biosynthesis in self-assembling peptide scaffolds. *Journal of biomechanics* 2004;37:595-604.
40. Kisiday JD, Lee JH, Siparsky PN, Frisbie DD, Flannery CR, Sandy JD, et al. Catabolic responses of chondrocyte-seeded peptide hydrogel to dynamic compression. *Annals of biomedical engineering* 2009;37:1368-1375.
41. Aufderheide AC, Athanasiou KA. A direct compression stimulator for articular cartilage and meniscal explants. *Annals of biomedical engineering* 2006;34:1463-1474.
42. Waldman SD, Couto DC, Grynblas MD, Pilliar RM, Kandel RA. Multi-axial mechanical stimulation of tissue engineered cartilage: review. *European cells & materials* 2007;13:66-73; discussion 73-64.
43. Mauck RL, Byers BA, Yuan X, Tuan RS. Regulation of cartilaginous ECM gene transcription by chondrocytes and MSCs in 3D culture in response to dynamic loading. *Biomechanics and modeling in mechanobiology* 2007;6:113-125.
44. Babalola OM, Bonassar LJ. Parametric finite element analysis of physical stimuli resulting from mechanical stimulation of tissue engineered cartilage. *Journal of biomechanical engineering* 2009;131:061014.
45. Bian L, Fong JV, Lima EG, Stoker AM, Ateshian GA, Cook JL, et al. Dynamic mechanical loading enhances functional properties of tissue-engineered cartilage using mature canine chondrocytes. *Tissue Eng Part A* 16:1781-1790.
46. Zielinska B, Killian M, Kadmiel M, Nelsen M, Haut Donahue TL. Meniscal tissue explants response depends on level of dynamic compressive strain. *Osteoarthritis and cartilage / OARS, Osteoarthritis Research Society* 2009;17:754-760.
47. Hennerbichler A, Fermor B, Hennerbichler D, Weinberg JB, Guilak F. Regional differences in prostaglandin E2 and nitric oxide production in the knee meniscus in response to dynamic compression. *Biochemical and biophysical research communications* 2007;358:1047-1053.

48. Shin SJ, Fermor B, Weinberg JB, Pisetsky DS, Guilak F. Regulation of matrix turnover in meniscal explants: role of mechanical stress, interleukin-1, and nitric oxide. *J Appl Physiol* 2003;95:308-313.
49. Upton ML, Chen J, Guilak F, Setton LA. Differential effects of static and dynamic compression on meniscal cell gene expression. *J Orthop Res* 2003;21:963-969.
50. Fink C, Fermor B, Weinberg JB, Pisetsky DS, Misukonis MA, Guilak F. The effect of dynamic mechanical compression on nitric oxide production in the meniscus. *Osteoarthritis and cartilage / OARS, Osteoarthritis Research Society* 2001;9:481-487.
51. Marsano A, Wendt D, Quinn TM, Sims TJ, Farhadi J, Jakob M, et al. Bi-zonal cartilaginous tissues engineered in a rotary cell culture system. *Biorheology* 2006;43:553-560.
52. Baker BM, Nathan AS, Huffman GR, Mauck RL. Tissue engineering with meniscus cells derived from surgical debris. *Osteoarthritis and cartilage / OARS, Osteoarthritis Research Society* 2009;17:336-345.
53. Gunja NJ, Athanasiou KA. Additive and synergistic effects of bFGF and hypoxia on leporine meniscus cell-seeded PLLA scaffolds. *J Tissue Eng Regen Med* 4:115-122.
54. Gunja NJ, Uthamanthil RK, Athanasiou KA. Effects of TGF-beta1 and hydrostatic pressure on meniscus cell-seeded scaffolds. *Biomaterials* 2009;30:565-573.
55. Gunja NJ, Athanasiou KA. Effects of co-cultures of meniscus cells and articular chondrocytes on PLLA scaffolds. *Biotechnology and bioengineering* 2009;103:808-816.
56. Vacanti CA. The history of tissue engineering. *Journal of cellular and molecular medicine* 2006;10:569-576.
57. Saleh K, Olson M, Resig S, Bershadsky B, Kuskowski M, Gioe T, et al. Predictors of wound infection in hip and knee joint replacement: results from a 20 year surveillance program. *J Orthop Res* 2002;20:506-515.

58. Miller CM, Gondolesi GE, Florman S, Matsumoto C, Munoz L, Yoshizumi T, et al. One hundred nine living donor liver transplants in adults and children: a single-center experience. *Annals of surgery* 2001;234:301-311; discussion 311-302.
59. Lietz K, John R, Mancini DM, Edwards NM. Outcomes in cardiac transplant recipients using allografts from older donors versus mortality on the transplant waiting list; Implications for donor selection criteria. *Journal of the American College of Cardiology* 2004;43:1553-1561.
60. Menick FJ. Facial reconstruction with local and distant tissue: the interface of aesthetic and reconstructive surgery. *Plastic and reconstructive surgery* 1998;102:1424-1433.
61. Cao Y, Vacanti JP, Paige KT, Upton J, Vacanti CA. Transplantation of chondrocytes utilizing a polymer-cell construct to produce tissue-engineered cartilage in the shape of a human ear. *Plastic and reconstructive surgery* 1997;100:297-302; discussion 303-294.
62. Weng Y, Cao Y, Silva CA, Vacanti MP, Vacanti CA. Tissue-engineered composites of bone and cartilage for mandible condylar reconstruction. *J Oral Maxillofac Surg* 2001;59:185-190.
63. Vacanti CA, Bonassar LJ, Vacanti MP, Shufflebarger J. Replacement of an avulsed phalanx with tissue-engineered bone. *The New England journal of medicine* 2001;344:1511-1514.
64. Theysohn JM, Maderwald S, Kraff O, Moenninghoff C, Ladd ME, Ladd SC. Subjective acceptance of 7 Tesla MRI for human imaging. *Magma (New York, NY)* 2008;21:63-72.
65. Elliott MR, Thrush AJ. Measurement of resolution in intravascular ultrasound images. *Physiological measurement* 1996;17:259-265.
66. White D, Chelule KL, Seedhom BB. Accuracy of MRI vs CT imaging with particular reference to patient specific templates for total knee replacement surgery. *Int J Med Robot* 2008.

67. Verhey JF, Nathan NS, Rienhoff O, Kikinis R, Rakebrandt F, D'Ambra MN. Finite-element-method (FEM) model generation of time-resolved 3D echocardiographic geometry data for mitral-valve volumetry. *Biomedical engineering online* 2006;5:17.
68. Little SH, Igo SR, McCulloch M, Hartley CJ, Nose Y, Zoghbi WA. Three-dimensional ultrasound imaging model of mitral valve regurgitation: design and evaluation. *Ultrasound in medicine & biology* 2008;34:647-654.
69. Chang SC, Rowley JA, Tobias G, Genes NG, Roy AK, Mooney DJ, et al. Injection molding of chondrocyte/alginate constructs in the shape of facial implants. *J Biomed Mater Res* 2001;55:503-511.
70. Isogai N, Landis W, Kim TH, Gerstenfeld LC, Upton J, Vacanti JP. Formation of phalanges and small joints by tissue-engineering. *The Journal of bone and joint surgery* 1999;81:306-316.
71. Kim WS, Vacanti JP, Cima L, Mooney D, Upton J, Puelacher WC, et al. Cartilage engineered in predetermined shapes employing cell transplantation on synthetic biodegradable polymers. *Plastic and reconstructive surgery* 1994;94:233-237; discussion 238-240.
72. Chang SC, Tobias G, Roy AK, Vacanti CA, Bonassar LJ. Tissue engineering of autologous cartilage for craniofacial reconstruction by injection molding. *Plastic and reconstructive surgery* 2003;112:793-799; discussion 800-791.
73. Del Gaudio C, Bianco A, Grigioni M. Electrospun bioresorbable trileaflet heart valve prosthesis for tissue engineering: in vitro functional assessment of a pulmonary cardiac valve design. *Annali dell'Istituto superiore di sanita* 2008;44:178-186.
74. Hott ME, Megerian CA, Beane R, Bonassar LJ. Fabrication of tissue engineered tympanic membrane patches using computer-aided design and injection molding. *The Laryngoscope* 2004;114:1290-1295.
75. Neidert MR, Tranquillo RT. Tissue-engineered valves with commissural alignment. *Tissue engineering* 2006;12:891-903.

76. Lee KW, Wang S, Lu L, Jabbari E, Currier BL, Yaszemski MJ. Fabrication and characterization of poly(propylene fumarate) scaffolds with controlled pore structures using 3-dimensional printing and injection molding. *Tissue engineering* 2006;12:2801-2811.
77. Hung CT, Lima EG, Mauck RL, Takai E, LeRoux MA, Lu HH, et al. Anatomically shaped osteochondral constructs for articular cartilage repair. *Journal of biomechanics* 2003;36:1853-1864.
78. Mizuno H, Roy AK, Vacanti CA, Kojima K, Ueda M, Bonassar LJ. Tissue-engineered composites of anulus fibrosus and nucleus pulposus for intervertebral disc replacement. *Spine* 2004;29:1290-1297; discussion 1297-1298.
79. Mizuno H, Roy AK, Zaporozhan V, Vacanti CA, Ueda M, Bonassar LJ. Biomechanical and biochemical characterization of composite tissue-engineered intervertebral discs. *Biomaterials* 2006;27:362-370.
80. Choi NW, Cabodi M, Held B, Gleghorn JP, Bonassar LJ, Stroock AD. Microfluidic scaffolds for tissue engineering. *Nature materials* 2007;6:908-915.
81. Mercier NR, Costantino HR, Tracy MA, Bonassar LJ. Poly(lactide-co-glycolide) microspheres as a moldable scaffold for cartilage tissue engineering. *Biomaterials* 2005;26:1945-1952.
82. Hutmacher DW, Cool S. Concepts of scaffold-based tissue engineering--the rationale to use solid free-form fabrication techniques. *Journal of cellular and molecular medicine* 2007;11:654-669.
83. Habibovic P, Gbureck U, Doillon CJ, Bassett DC, van Blitterswijk CA, Barralet JE. Osteoconduction and osteoinduction of low-temperature 3D printed bioceramic implants. *Biomaterials* 2008;29:944-953.
84. Khalyfa A, Vogt S, Weisser J, Grimm G, Rechtenbach A, Meyer W, et al. Development of a new calcium phosphate powder-binder system for the 3D printing of patient specific implants. *Journal of materials science* 2007;18:909-916.

85. Schek RM, Taboas JM, Hollister SJ, Krebsbach PH. Tissue engineering osteochondral implants for temporomandibular joint repair. *Orthodontics & craniofacial research* 2005;8:313-319.
86. Sherwood JK, Riley SL, Palazzolo R, Brown SC, Monkhouse DC, Coates M, et al. A three-dimensional osteochondral composite scaffold for articular cartilage repair. *Biomaterials* 2002;23:4739-4751.
87. Klebe RJ. Cytoscribing: a method for micropositioning cells and the construction of two- and three-dimensional synthetic tissues. *Experimental cell research* 1988;179:362-373.
88. Cohen DL, Malone E, Lipson H, Bonassar LJ. Direct freeform fabrication of seeded hydrogels in arbitrary geometries. *Tissue engineering* 2006;12:1325-1335.
89. Liu Tsang V, Chen AA, Cho LM, Jadin KD, Sah RL, DeLong S, et al. Fabrication of 3D hepatic tissues by additive photopatterning of cellular hydrogels. *Faseb J* 2007;21:790-801.
90. Chang R, Nam J, Sun W. Effects of dispensing pressure and nozzle diameter on cell survival from solid freeform fabrication-based direct cell writing. *Tissue Eng Part A* 2008;14:41-48.
91. Chang R, Nam J, Sun W. Direct Cell Writing of 3D Microorgan for In Vitro Pharmacokinetic Model. *Tissue Eng Part C Methods* 2008;14:157-166.
92. Kaihara S, Borenstein J, Koka R, Lalan S, Ochoa ER, Ravens M, et al. Silicon micromachining to tissue engineer branched vascular channels for liver fabrication. *Tissue engineering* 2000;6:105-117.
93. Cheng CM, LeDuc PR. Micropatterning polyvinyl alcohol as a biomimetic material through soft lithography with cell culture. *Molecular bioSystems* 2006;2:299-303.
94. Sarkar S, Lee GY, Wong JY, Desai TA. Development and characterization of a porous micro-patterned scaffold for vascular tissue engineering applications. *Biomaterials* 2006;27:4775-4782.

95. Subramani K, Birch MA. Fabrication of poly(ethylene glycol) hydrogel micropatterns with osteoinductive growth factors and evaluation of the effects on osteoblast activity and function. *Biomedical materials (Bristol, England)* 2006;1:144-154.
96. Karp JM, Yeh J, Eng G, Fukuda J, Blumling J, Suh KY, et al. Controlling size, shape and homogeneity of embryoid bodies using poly(ethylene glycol) microwells. *Lab on a chip* 2007;7:786-794.
97. Sodunke TR, Turner KK, Caldwell SA, McBride KW, Reginato MJ, Noh HM. Micropatterns of Matrigel for three-dimensional epithelial cultures. *Biomaterials* 2007;28:4006-4016.
98. McGuigan AP, Bruzewicz DA, Glavan A, Butte M, Whitesides GM. Cell encapsulation in sub-mm sized gel modules using replica molding. *PLoS ONE* 2008;3:e2258.
99. Khademhosseini A, Eng G, Yeh J, Kucharczyk PA, Langer R, Vunjak-Novakovic G, et al. Microfluidic patterning for fabrication of contractile cardiac organoids. *Biomedical microdevices* 2007;9:149-157.
100. Cabodi M, Choi NW, Gleghorn JP, Lee CS, Bonassar LJ, Stroock AD. A microfluidic biomaterial. *Journal of the American Chemical Society* 2005;127:13788-13789.
101. Lee CS, Gleghorn JP, Won Choi N, Cabodi M, Stroock AD, Bonassar LJ. Integration of layered chondrocyte-seeded alginate hydrogel scaffolds. *Biomaterials* 2007;28:2987-2993.
102. Wiria FE, Chua CK, Leong KF, Quah ZY, Chandrasekaran M, Lee MW. Improved biocomposite development of poly(vinyl alcohol) and hydroxyapatite for tissue engineering scaffold fabrication using selective laser sintering. *Journal of materials science* 2008;19:989-996.
103. Tanimoto Y, Nishiyama N. Preparation and physical properties of tricalcium phosphate laminates for bone-tissue engineering. *J Biomed Mater Res A* 2008;85:427-433.

104. Borden M, Attawia M, Laurencin CT. The sintered microsphere matrix for bone tissue engineering: in vitro osteoconductivity studies. *J Biomed Mater Res* 2002;61:421-429.
105. Mercier NR, Costantino HR, Tracy MA, Bonassar LJ. A novel injectable approach for cartilage formation in vivo using PLG microspheres. *Annals of biomedical engineering* 2004;32:418-429.
106. Huang A, Hull ML, Howell SM, Haut Donahue T. Identification of cross-sectional parameters of lateral meniscal allografts that predict tibial contact pressure in human cadaveric knees. *Journal of biomechanical engineering* 2002;124:481-489.
107. Donahue TL, Hull ML, Howell SM. New algorithm for selecting meniscal allografts that best match the size and shape of the damaged meniscus. *J Orthop Res* 2006;24:1535-1543.
108. Rankin JS, Dalley AF, Crooke PS, Anderson RH. A 'hemispherical' model of aortic valvar geometry. *The Journal of heart valve disease* 2008;17:179-186.
109. Haj-Ali R, Dasi LP, Kim HS, Choi J, Leo HW, Yoganathan AP. Structural simulations of prosthetic tri-leaflet aortic heart valves. *Journal of biomechanics* 2008;41:1510-1519.
110. Gray ML, Burstein D, Kim YJ, Maroudas A. 2007 Elizabeth Winston Lanier Award Winner. Magnetic resonance imaging of cartilage glycosaminoglycan: basic principles, imaging technique, and clinical applications. *J Orthop Res* 2008;26:281-291.
111. Palmer AW, Guldberg RE, Levenston ME. Analysis of cartilage matrix fixed charge density and three-dimensional morphology via contrast-enhanced microcomputed tomography. *Proceedings of the National Academy of Sciences of the United States of America* 2006;103:19255-19260.
112. Fritton JC, Myers ER, Wright TM, van der Meulen MC. Bone mass is preserved and cancellous architecture altered due to cyclic loading of the mouse tibia after orchidectomy. *J Bone Miner Res* 2008;23:663-671.

113. Yasui T, Tohno Y, Araki T. Determination of collagen fiber orientation in human tissue by use of polarization measurement of molecular second-harmonic-generation light. *Applied optics* 2004;43:2861-2867.
114. Raub CB, Suresh V, Krasieva T, Lyubovitsky J, Mih JD, Putnam AJ, et al. Noninvasive assessment of collagen gel microstructure and mechanics using multiphoton microscopy. *Biophysical journal* 2007;92:2212-2222.
115. Androjna C, Spragg RK, Derwin KA. Mechanical conditioning of cell-seeded small intestine submucosa: a potential tissue-engineering strategy for tendon repair. *Tissue engineering* 2007;13:233-243.
116. Flanagan TC, Cornelissen C, Koch S, Tschoeke B, Sachweh JS, Schmitz-Rode T, et al. The in vitro development of autologous fibrin-based tissue-engineered heart valves through optimised dynamic conditioning. *Biomaterials* 2007;28:3388-3397.
117. Wood MA, Yang Y, Thomas PB, Haj AJ. Using dihydropyridine-release strategies to enhance load effects in engineered human bone constructs. *Tissue engineering* 2006;12:2489-2497.
118. Schumann D, Kujat R, Nerlich M, Angele P. Mechanobiological conditioning of stem cells for cartilage tissue engineering. *Bio-medical materials and engineering* 2006;16:S37-52.
119. Wan DC, Nacamuli RP, Longaker MT. Craniofacial bone tissue engineering. *Dent Clin North Am* 2006;50:175-190, vii.
120. Esselman PC, Thombs BD, Magyar-Russell G, Fauerbach JA. Burn rehabilitation: state of the science. *Am J Phys Med Rehabil* 2006;85:383-413.
121. Jones DL, Westby MD, Greidanus N, Johanson NA, Krebs DE, Robbins L, et al. Update on hip and knee arthroplasty: current state of evidence. *Arthritis Rheum* 2005;53:772-780.
122. Rotter N, Bonassar LJ, Tobias G, Lebl M, Roy AK, Vacanti CA. Age dependence of biochemical and biomechanical properties of tissue-engineered human septal cartilage. *Biomaterials* 2002;23:3087-3094.

123. Hoque ME, Hutmacher DW, Feng W, Li S, Huang MH, Vert M, et al. Fabrication using a rapid prototyping system and in vitro characterization of PEG-PCL-PLA scaffolds for tissue engineering. *J Biomater Sci Polym Ed* 2005;16:1595-1610.
124. Izuta Y, Ochi M, Adachi N, Deie M, Yamasaki T, Shinomiya R. Meniscal repair using bone marrow-derived mesenchymal stem cells: experimental study using green fluorescent protein transgenic rats. *The Knee* 2005;12:217-223.
125. Reguzzoni M, Manelli A, Ronga M, Raspanti M, Grassi FA. Histology and ultrastructure of a tissue-engineered collagen meniscus before and after implantation. *Journal of biomedical materials research* 2005;74:808-816.
126. Martinek V, Ueblacker P, Braun K, Nitschke S, Mannhardt R, Specht K, et al. Second generation of meniscus transplantation: in-vivo study with tissue engineered meniscus replacement. *Archives of orthopaedic and trauma surgery* 2006;126:228-234.
127. Pangborn CA, Athanasiou KA. Effects of growth factors on meniscal fibrochondrocytes. *Tissue engineering* 2005;11:1141-1148.
128. Tienen TG, Heijkants RG, de Groot JH, Pennings AJ, Schouten AJ, Veth RP, et al. Replacement of the knee meniscus by a porous polymer implant: a study in dogs. *The American journal of sports medicine* 2006;34:64-71.
129. Gleghorn JP, Jones AR, Flannery CR, Bonassar LJ. Boundary mode frictional properties of engineered cartilaginous tissues. *European cells & materials* 2007;14:20-28; discussion 28-29.
130. Oegema TR, Jr., Carpenter BJ, Thompson RC, Jr. Fluorometric determination of DNA in cartilage of various species. *J Orthop Res* 1984;1:345-351.
131. Kim YJ, Sah RL, Doong JY, Grodzinsky AJ. Fluorometric assay of DNA in cartilage explants using Hoechst 33258. *Analytical biochemistry* 1988;174:168-176.
132. Enobakhare BO, Bader DL, Lee DA. Quantification of sulfated glycosaminoglycans in chondrocyte/alginate cultures, by use of 1,9-dimethylmethylene blue. *Analytical biochemistry* 1996;243:189-191.

133. Neuman RE, Logan MA. The determination of hydroxyproline. *The Journal of biological chemistry* 1950;184:299-306.
134. Nakamura K, Kawaguchi H, Aoyama I, Hanada K, Hiyama Y, Awa T, et al. Stimulation of bone formation by intraosseous application of recombinant basic fibroblast growth factor in normal and ovariectomized rabbits. *J Orthop Res* 1997;15:307-313.
135. Almarza AJ, Athanasiou KA. Design characteristics for the tissue engineering of cartilaginous tissues. *Annals of biomedical engineering* 2004;32:2-17.
136. Oegema TR, Jr., Deloria LB, Sandy JD, Hart DA. Effect of oral glucosamine on cartilage and meniscus in normal and chymopapain-injected knees of young rabbits. *Arthritis Rheum* 2002;46:2495-2503.
137. Perie DS, Maclean JJ, Owen JP, Iatridis JC. Correlating material properties with tissue composition in enzymatically digested bovine annulus fibrosus and nucleus pulposus tissue. *Annals of biomedical engineering* 2006;34:769-777.
138. Kelly DJ, Crawford A, Dickinson SC, Sims TJ, Mundy J, Hollander AP, et al. Biochemical markers of the mechanical quality of engineered hyaline cartilage. *Journal of materials science* 2007;18:273-281.
139. Malda J, Martens DE, Tramper J, van Blitterswijk CA, Riesle J. Cartilage tissue engineering: controversy in the effect of oxygen. *Crit Rev Biotechnol* 2003;23:175-194.
140. Adesida AB, Grady LM, Khan WS, Hardingham TE. The matrix-forming phenotype of cultured human meniscus cells is enhanced after culture with fibroblast growth factor 2 and is further stimulated by hypoxia. *Arthritis research & therapy* 2006;8:R61.
141. Basser PJ, Pajevic S. A normal distribution for tensor-valued random variables: applications to diffusion tensor MRI. *IEEE Trans Med Imaging* 2003;22:785-794.
142. Ballyns JJ, Cohen D, Malone E, Maher SA, Potter HG, Wright TM, et al. An Optical Method for Evaluation of Geometric Fidelity for Anatomically Shaped Tissue Engineered Constructs. *Tissue Eng Part C Methods* 2009.

143. Sohn DH, Toth AP. Meniscus transplantation: current concepts. *The journal of knee surgery* 2008;21:163-172.
144. Kuhn MA, Ross G. Allografts in the treatment of anterior cruciate ligament injuries. *Sports medicine and arthroscopy review* 2007;15:133-138.
145. Schmidt D, Hoerstrup SP. Tissue engineered heart valves based on human cells. *Swiss Med Wkly* 2006;136:618-623.
146. Mironov V, Boland T, Trusk T, Forgacs G, Markwald RR. Organ printing: computer-aided jet-based 3D tissue engineering. *Trends in biotechnology* 2003;21:157-161.
147. Wang SH, Quan CG, Tay CJ, Shang HM. Surface roughness measurement in the submicrometer range using laser scattering. *Optical Engineering* 2000;39:1597-1601.
148. Halliwell NA. The laser torsional vibrometer: A step forward in rotating machinery diagnostics. *Journal of Sound and Vibration* 1996;190:399-418.
149. McDermott ID, Sharifi F, Bull AM, Gupte CM, Thomas RW, Amis AA. An anatomical study of meniscal allograft sizing. *Knee Surg Sports Traumatol Arthrosc* 2004;12:130-135.
150. Haut TL, Hull ML, Howell SM. Use of roentgenography and magnetic resonance imaging to predict meniscal geometry determined with a three-dimensional coordinate digitizing system. *J Orthop Res* 2000;18:228-237.
151. Stone KR, Freyer A, Turek T, Walgenbach AW, Wadhwa S, Crues J. Meniscal sizing based on gender, height, and weight. *Arthroscopy* 2007;23:503-508.
152. Rankin M, Noyes FR, Barber-Westin SD, Hushek SG, Seow A. Human meniscus allografts' in vivo size and motion characteristics: magnetic resonance imaging assessment under weightbearing conditions. *The American journal of sports medicine* 2006;34:98-107.
153. Rodeo SA. Meniscal allografts--where do we stand? *The American journal of sports medicine* 2001;29:246-261.

154. Busse RF, Hariharan H, Vu A, Brittain JH. Fast spin echo sequences with very long echo trains: design of variable refocusing flip angle schedules and generation of clinical T2 contrast. *Magn Reson Med* 2006;55:1030-1037.
155. Pabbruwe MB, Kafienah W, Tarlton JF, Mistry S, Fox DJ, Hollander AP. Repair of meniscal cartilage white zone tears using a stem cell/collagen-scaffold implant. *Biomaterials* 2010;31:2583-2591.
156. Horie M, Sekiya I, Muneta T, Ichinose S, Matsumoto K, Saito H, et al. Intra-articular Injected synovial stem cells differentiate into meniscal cells directly and promote meniscal regeneration without mobilization to distant organs in rat massive meniscal defect. *Stem cells (Dayton, Ohio)* 2009;27:878-887.
157. Fox DB, Luther JK, Whitener D. An in vitro model to assess mechanisms and efficacy of a cellular conduit for treatment of avascular meniscal injuries. *In vitro cellular & developmental biology* 2008;44:185-188.
158. Becker R, Wirz D, Wolf C, Gopfert B, Nebelung W, Friederich N. Measurement of meniscofemoral contact pressure after repair of bucket-handle tears with biodegradable implants. *Archives of orthopaedic and trauma surgery* 2005;125:254-260.
159. Collier S, Ghosh P. Effects of transforming growth factor beta on proteoglycan synthesis by cell and explant cultures derived from the knee joint meniscus. *Osteoarthritis and cartilage / OARS, Osteoarthritis Research Society* 1995;3:127-138.
160. Chen JP, Cheng TH. Thermo-responsive chitosan-graft-poly(N-isopropylacrylamide) injectable hydrogel for cultivation of chondrocytes and meniscus cells. *Macromolecular bioscience* 2006;6:1026-1039.
161. Gunja NJ, Athanasiou KA. Effects of hydrostatic pressure on leporine meniscus cell-seeded PLLA scaffolds. *J Biomed Mater Res A* 2009.
162. O'Hern TJ, Torczynski JR. Reynolds number dependence of the drag coefficient for laminar flow through fine-scale photoetched screens. *Experiments in Fluids* 1993;15:75-81.

163. Cherry RS, Papoutsakis ET. Hydrodynamic effects on cells in agitated tissue culture reactors. *Bioprocess Engineering* 1986;1:29-41.
164. Kim YJ, Bonassar LJ, Grodzinsky AJ. The role of cartilage streaming potential, fluid flow and pressure in the stimulation of chondrocyte biosynthesis during dynamic compression. *Journal of biomechanics* 1995;28:1055-1066.
165. Drury JL, Dennis RG, Mooney DJ. The tensile properties of alginate hydrogels. *Biomaterials* 2004;25:3187-3199.
166. Gunja NJ, Huey DJ, James RA, Athanasiou KA. Effects of agarose mould compliance and surface roughness on self-assembled meniscus-shaped constructs. *J Tissue Eng Regen Med* 2009;3:521-530.
167. Kock LM, Schulz RM, van Donkelaar CC, Thummler CB, Bader A, Ito K. RGD-dependent integrins are mechanotransducers in dynamically compressed tissue-engineered cartilage constructs. *Journal of biomechanics* 2009;42:2177-2182.
168. Gunja NJ, Athanasiou KA. Effects of hydrostatic pressure on leporine meniscus cell-seeded PLLA scaffolds. *J Biomed Mater Res A* 2010;92:896-905.
169. Hunter CJ, Mouw JK, Levenston ME. Dynamic compression of chondrocyte-seeded fibrin gels: effects on matrix accumulation and mechanical stiffness. *Osteoarthritis and cartilage / OARS, Osteoarthritis Research Society* 2004;12:117-130.
170. Villanueva I, Hauschulz DS, Mejc D, Bryant SJ. Static and dynamic compressive strains influence nitric oxide production and chondrocyte bioactivity when encapsulated in PEG hydrogels of different crosslinking densities. *Osteoarthritis and cartilage / OARS, Osteoarthritis Research Society* 2008;16:909-918.
171. Ballyns JJ, Maher SA, Wright TM, Bonassar LJ. Effect of Mixing Intensity on ECM Assembly and Mechanical Properties of Anatomically Shaped Tissue Engineered Meniscus. *Transactions of the Orthopaedic Research Society* 2008;33:1461.

172. Wilson CG, Bonassar LJ, Kohles SS. Modeling the dynamic composition of engineered cartilage. *Arch Biochem Biophys* 2002;408:246-254.
173. Bonassar LJ, Stinn JL, Paguio CG, Frank EH, Moore VL, Lark MW, et al. Activation and inhibition of endogenous matrix metalloproteinases in articular cartilage: effects on composition and biophysical properties. *Arch Biochem Biophys* 1996;333:359-367.
174. Seifarth C, Csaki C, Shakibaei M. Anabolic actions of IGF-I and TGF-beta1 on Interleukin-1beta-treated human articular chondrocytes: evaluation in two and three dimensional cultures. *Histol Histopathol* 2009;24:1245-1262.
175. Tumia NS, Johnstone AJ. Regional regenerative potential of meniscal cartilage exposed to recombinant insulin-like growth factor-I in vitro. *J Bone Joint Surg Br* 2004;86:1077-1081.
176. Trautman NM, Kransy ME. Integrating Teaching and Research: A New Model for Graduate Education? *BioScience* 2006;56:159-165.
177. American_Association_of_Orthopaedic_Surgeons. The Burden of Musculoskeletal Disease in the United States. Rosemont, IL: American Academy of Orthopaedic Surgeons, 2008.
178. Sabra W, Zeng AP, Deckwer WD. Bacterial alginate: physiology, product quality and process aspects. *Applied microbiology and biotechnology* 2001;56:315-325.
179. Hoppensteadt FC, Peskin CS. Modeling and Simulation in Medicine and the Life Sciences 2nd Edition. 2nd ed. New York, NY: Springer-Verlag, 2002.